学位論文

Study of superconducting gap structure in prototypical heavy-fermion $CeCu_2Si_2$

平成 29 年 1 月博士 (理学) 申請
京都大学大学院理学研究科 物理学・宇宙物理学専攻

山下卓也

Abstract

Superconductivity is one of the best-known macroscopic quantum phenomena in condensed matter physics. The history of superconductivity was started by Heike Kamerlingh Onnes, who found a sudden drop in the resistance of elemental mercury at 4.2 K in 1911. After discovering superconductivity, the first microscopic theory was formulated by John Bardeen, Leon Neil Cooper, and John Robert Schrieffer in 1957, commonly called the BCS theory. The BCS theory has provided a very successful explanation for "conventional" superconductivity, in which electrons form the so-called Cooper pairs through k-independent attractive interactions mediated by phonons. Therefore, the superconducting gap is isotropic owing to s-wave pairing in conventional superconductors.

However, the discovery of a heavy-fermion superconductor in 1979 and high-T_c copper oxide superconductors (so-called cuprates) in 1987 dramatically changed the field. The unusual superconducting properties and the high T_c superconductivity, especially in cuprates, cannot be explained by the framework of the BCS theory. Moreover, the conventional phonon-mediated on-site pairing is unlikely because the electron correlation in those system is so strong. In fact, the strongly correlated superconductivity often emerges as the antiferromagnetic (AFM) long-range order is suppressed. Therefore, such superconductivity is widely believed to be magnetically driven rather than resulting from the conventional electron-phonon, namely, spin-fluctuation mechanism. Strong k-dependent repulsive interaction plays a key role for Cooper paring in the spin-fluctuation mechanism. Such an unconventional pairing mechanism leads to anisotropic superconductivity. For example, the superconducting gap symmetry in cuprates is widely believed to be $d_{x^2-y^2}$, where the gap changes sign along the AFM propagation vector $\boldsymbol{Q} = (\pi, \pi)$ to satisfy the gap equation $\Delta(\boldsymbol{k}+\boldsymbol{Q})\Delta(\boldsymbol{k}) < 0$. Thus cuprates have superconducting gap nodes along the $\boldsymbol{Q}$ vector. In real space, the repulsive interactions

appear at the on-site (x, y)=(0, 0) and $(x, y) = (\pm a, \pm a)$. However, attractive interactions appear at $(x, y) = (\pm a, 0)$, $(0, \pm a)$ (a is the unit cell length of the cuprates). Therefore, off-site pairing is realized to prevent strong repulsion force between electrons. The heavy-fermion $CeCoIn_5$ is also believed to be $d_{x^2-y^2}$-wave superconductor. In 2006, the new Fe-based superconductor LaFePO ($T_c = 4$ K) was discovered by Hosono's group. In 2008, they observed the high T_c of 26 K by replacing P with As, which has attracted much attention both experimentally and theoretically. In Fe-based superconductors, the superconductivity emerges in the vicinity of the antiferromagnetic spin-density-wave (SDW) order. Such close proximity between magnetism and superconductivity is similar to that of cuprates. However, in sharp contrast with cuprates, the Fe-based superconductor is characterized by a multiband electronic structure. Since the typical Fe-based superconductors have a disconnected quasi-2D cylindrical hole pocket at the Brillioun zone center and electron pocket at the Brillioun zone boundary, strong nesting between them would be essential for pairing. If the spin fluctuation mechanism is important, $S_{\pm}$-wave symmetry, in which the gap changes sign between the hole and electron pockets, is realized. On the other hand, orbital fluctuation-mediated pairing suggests S_{++}-wave symmetry.

As seen above, the superconducting gap symmetry is intimately related to the pairing interaction. Therefore, a considerable amount of research investigating the superconducting gap symmetry is being carried out in order to clarify the pairing mechanism.

• Study of superconducting gap structure in prototypical heavy-fermion $CeCu_2Si_2$

Strongly correlated electrons have been one of the most fascinating systems in modern physics. They exhibit a rich variety of exotic phenomena such as unconventional superconductivity, non-Fermi liquid, exotic orders and so on. The strongest electron correlation is realized in heavy-fermion (HF) compound, in which the quasiparticle effective mass is typically two or three orders of magnitude larger than the bare electron mass. In particular, such heavy quasiparticles often exhibit unconventional supercon-

ductivity in the vicinity of the magnetic instability, so-called quantum critical point (QCP).

$CeCu_2Si_2$ is a prototypical HF superconductor with T_c of 0.6 K discovered in 1979. The large specific heat jump at T_c indicates that the heavy electrons form Cooper pairs. The decrease of the Knight shift below T_c indicates the spin-singlet superconductivity. Moreover, $T^{3/2}$ behavior in the resistivity and $T^{1/2}$ behavior in γ indicate that the superconductivity occurs in the vicinity of an antiferromagnetic (AF) QCP. Unconventional nature of the superconductivity has been reported in some experiments, including the T-linear behavior of C/T, and no coherence peak just below T_c and the T^3 behavior in NMR relaxation rate $1/T_1$. Based on these results, the superconducting symmetry in $CeCu_2Si_2$ has been suggested to be d-wave with line nodes mediated by AF spin-fluctuations. On the other hand, recent specific heat measurements suggested fully-gapped superconductivity. However, since the specific heat mainly detects the quasiparticle contribution in the heavy electron band, the possibilities of the existence of nodes in the light hole band cannot be excluded.

Here, to clarify the superconducting gap structure of $CeCu_2Si_2$, we performed the thermal conductivity (κ) measurements which sensitively probe the quasiparticle contribution in the light band. At the lowest temperatures in zero-field, κ/T extrapolated to $T = 0$ goes to zero within our experimental resolution or is at least an order of magnitude smaller than that expected for line nodes. Moreover, field dependence of κ/T shows that the magnetic field hardly affects the thermal conduction in the low field regime, which is in stark contrast to the nodal superconductor. Based on these results, we conclude the absence of gap nodes at any point on the Fermi surface. Furthermore, in order to clarify whether there is sign change in the superconducting gap, we performed the electron-irradiation experiments. We found a very small pair-breaking effect, which suggests there are no sign changes in the superconducting gap function.

These results imply that, contrary to long-standing belief, heavy electrons with extremely strong Coulomb repulsions can condense into a fully-gapped s-wave superconducting state, which has an on-site attractive pairing interaction.

Contents

1 Introduction

1.1 Superconductivity

Superconductivity is one of the best-known macroscopic quantum phenomena in condensed matter physics. The history of superconductivity was initiated by Heike Kamerlingh Onnes, who found a sudden drop in the resistance of elemental mercury at 4.2 K in 1911 [1]. After 46 years from the discovery of superconductivity, the first microscopic theory was formulated by John Bardeen, Leon Neil Cooper and John Robert Schrieffer in 1957, commonly called the BCS theory [2]. The BCS theory has provided a very successful explanation for the properties and mechanism of superconductivity, in which conduction electrons form so-called Cooper pairs through k-independent attractive interaction mediated by phonon and then the pairs condense into a ground state. Such phonon-mediated superconductivity is characterized by an isotropic s-wave superconducting gap structure and is now called "conventional."

Generally, in all superconductors the $U(1)$ gauge symmetry is broken below the superconducting transition temperature T_c. Conventional superconductors are those in which only the $U(1)$ gauge symmetry is broken. Recently, as will be discussed in a later section, the study of "unconventional" superconductivity has become a central problem in condensed matter physics. Unconventional superconductors break an additional symmetry in addition to $U(1)$. The general classification scheme for the superconducting order parameter is based on its behavior under symmetry transformations. The full symmetry group $\mathcal{G}$ of the crystal is given by

$$\mathcal{G} = U(1) \otimes G \otimes SU(2) \otimes \mathcal{T} \tag{1.1}$$

where G is the crystal point group, $SU(2)$ is the spin rotation group, and $\mathcal{T}$ is the time reversal symmetry group. In unconventional superconductors, therefore, the order pa-

rameter (i) breaks the point group symmetry of the crystal, (ii) has odd parity, and/or (iii) breaks the time reversal symmetry. So far, numerous groups have reported anomalous and exotic physical properties associated with unconventional superconductivity.

1.2 Overview of unconventional superconductors

The unexpected discovery of superconductivity in the heavy-fermion compound $CeCu_2Si_2$ by Frank Steglich in 1979 [3] turned the BCS paradigm on its head. In a heavy-fermion system, the f-shell electrons are strongly correlated due to their localized character. Below a certain characteristic temperature, hybridization between the localized f-electrons and the conduction electrons occurs, which leads to the formation of quasiparticles with large effective masses. The superconducting Cooper pairs in $CeCu_2Si_2$ are widely believed to be formed from these heavy quasiparticles. These quasiparticles with f characters would have difficulty in forming ordinary s-wave Cooper pairs due to the strong Coulomb repulsion. Furthermore, unusual superconducting properties have been observed in $CeCu_2Si_2$, which cannot be explained by the framework of BCS theory. This evidence made it clear that $CeCu_2Si_2$ was not an ordinary BCS superconductor, and opened a new era of "unconventional" superconductivity.

One of the most important breakthroughs of condensed matter physics is the high-temperature copper oxide superconductor (so-called high-T_c cuprates), discovered by Johannes Georg Bednorz and Karl Alexander Müller in 1987 [4]. They observed superconducting transition below 35 K in $Ba_xLa_{5-x}Cu_5O_{5(3-y)}$, which was the highest T_c at that time. In cuprates, the parent compounds are known to be antiferromagnetic Mott insulators. The superconductivity often emerges when the antiferromagnetic phase is completely suppressed by electron or hole doping. Currently, the superconductor with the highest T_c is $HgBa_2Ca_2Cu_3O_{8+\delta}$ at around 153 K under high pressure [5]. The unexpectedly high T_c that cannot be explained by BCS theory also made it clear that the cuprates are unconventional superconductors and urged theorists to construct a theoretical description beyond BCS.

In 2006, the new Fe-based superconductor LaFePO (T_c = 4 K) was discovered by

Hosono's group [6]. In 2008, they observed the high T_c of 26 K by replacing P with As [7], which has attracted much attention both experimentally and theoretically. Moreover, in sharp contrast with cuprates, the Fe-based superconductor is characterized by a multiband electronic structure. This multiband nature has also attracted much interest because the intricate interplay between spin and orbitals degrees of freedom leads to novel electronic phases. In the Fe-based superconductor, the superconductivity often emerges when the antiferromagnetic spin-density-wave (SDW) order is suppressed. Such close proximity between magnetism and superconductivity is similar to that of heavy-fermion system.

What is important for these strongly correlated superconductors is that the superconductivity emerges in the vicinity of the antiferromagnetic (AFM) quantum critical point (QCP). This fact suggests that the electron-electron interactions are more significant than the electron-phonon interactions. From this point of view, spin-fluctuation-mediated pairing mechanism is the most promising candidate for the microscopic origin of superconductivity in these systems. As will be explained in a later section, this spin-fluctuation mechanism leads to anisotropic superconducting gap structure. For example, it is widely believed that the cuprates have a $d_{x^2-y^2}$-wave symmetry, which leads to line nodes (that is zero gaps) along the c-axis in the superconducting gap. Heavy-fermion superconductors, in which the strongest electron correlation is realized, also have line nodes in the superconducting gap. On the other hand, since typical Fe-based superconductors have disconnected quasi-2D cylindrical hole pockets at the Brillioun zone center and electron pockets at the Brillioun zone boundary due to their multiband nature, the strong nesting between them would play a role for Cooper pairing. If the spin fluctuation mechanism is important, $S_{\pm}$-wave symmetry, in which the gap changes sign between the hole and electron pockets, is realized. On the other hand, orbital fluctuation mediated pairing suggests S_{++}-wave symmetry.

As seen above, the superconducting gap symmetry is intimately related to the pairing interaction. Therefore, a lot of research investigating the superconducting gap symmetry is being carried out in order to identify the pairing mechanism.

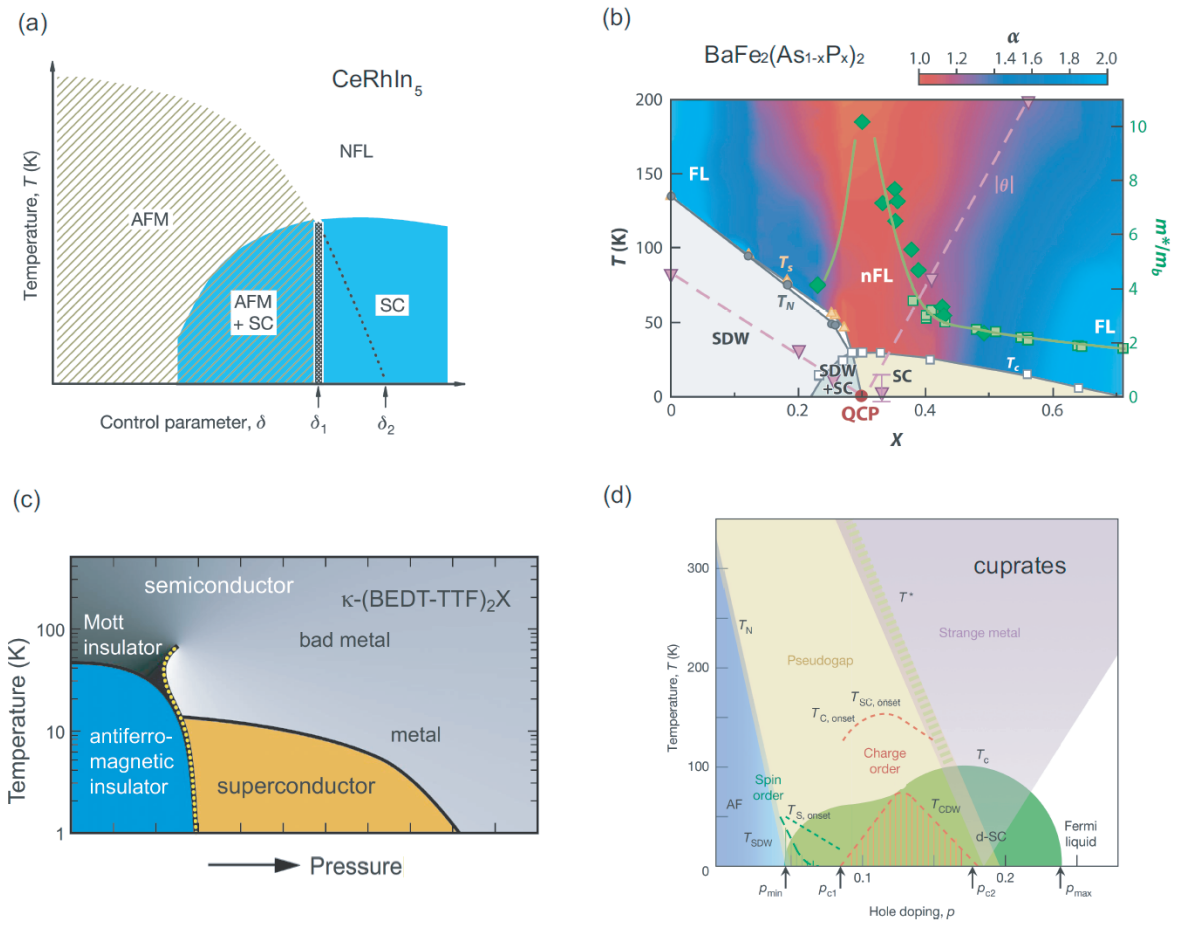

Figure 1.1: Phase diagram of several strongly correlated materials. (a) heavy-fermion superconductor $CeRhIn_5$ [8], (b) Fe-pnictide $BaFe_2(As_{1-x}P_x)_2$ [9], (c) organic κ-(BEDT-TTF)$_2$X [10] and (d) high-T_c cuprates [11].

1.3 Quantum critical point and unconventional superconductivity

As mentioned in the previous section, unconventional superconductivity seems to be related to an ordered phase in strongly correlated materials. Figure 1.2 depicts the general phase diagram found in strongly correlated materials, including heavy-fermion compounds, Fe-pnictides, and so on [9]. The second-order phase transition at T_o (*e.g.*, $T_o = T_N$ in case of AFM order) can be suppressed by increasing a non-thermal parameter g, and then disappears at $g = g_c$. The end point of a line of finite-T phase transition, which separates the two distinct quantum phases at zero temperature, is the QCP. In

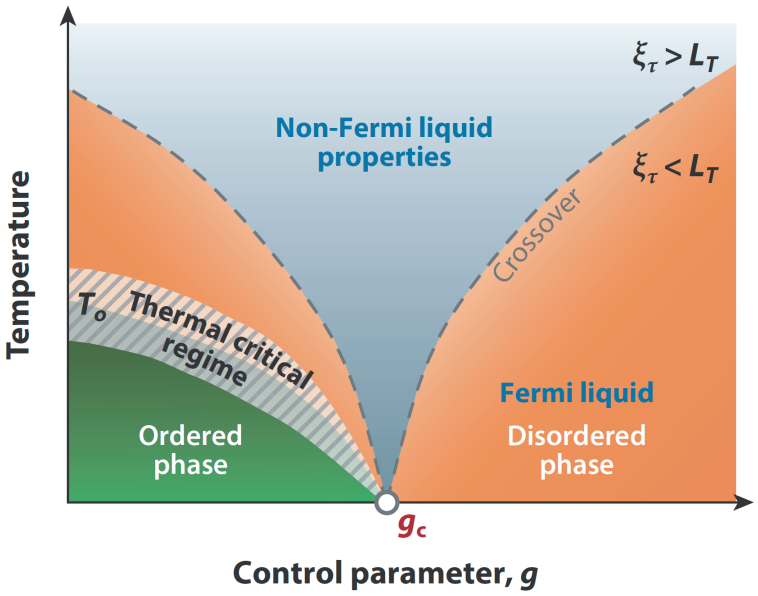

Figure 1.2: General phase diagram in the vicinity of QCP [9]. The non-Fermi-liquid region spreads like a fan from the QCP to high temperature. Importantly, unconventional superconductivity often emerges in the vicinity of the QCP.

the regime where the thermal timescale $L_\tau \equiv \hbar/k_B T$ is much shorter than the quantum timescale ξ_τ, the physical quantities cannot be simply described by the ground state wave function at g.

In this quantum critical regime, the temperature dependences of physical quantities often deviate from the conventional Landau's Fermi-liquid behavior. For example, at low-T, the $T^{3/2}$-dependence of the resistivity, $\rho(T) = \rho_0 + \alpha T^{3/2}$, and the $T^{1/2}$ dependence of the electronic specific heat coefficient, $\gamma(T) = \gamma_0 - \beta T^{1/2}$, are observed in the vicinity of the AFM QCP in a 3D system, which are well explained by the self-consistent renormalization (SCR) theory of spin fluctuations [12]. This "non-Fermi" liquid region spreads like a fan-shape from the QCP to high temperatures. More interestingly, the unconventional superconductivity often emerges in the vicinity of the QCP; in other words, quantum critical instability. Furthermore, the superconducting transition temperature reaches its maximum at the QCP. From this point of view, the pairing glue in unconventional superconductors is believed to not be phonon vibrations but other mechanisms related to the quantum instability such as antiferromagnetic spin fluctuations.

1.4 d-wave superconductivity mediated by spin fluctuation mechanism

Because the superconducting gap structure is intimately related to the pairing interaction, the elucidation of the superconducting gap symmetry is extremely important for understanding the mechanism of the superconductivity. In this section, we will see the emergence of the unconventional superconductivity with angular momentum l greater than zero, in brief.

The BCS mean field Hamiltonian is written by,

$$\mathscr{H} = \sum_{\boldsymbol{k}} \begin{pmatrix} \psi^{\dagger}_{\boldsymbol{k},\uparrow} & \psi_{\boldsymbol{k},\downarrow} \end{pmatrix} \begin{pmatrix} \xi(\boldsymbol{k}) & \Delta(\boldsymbol{k}) \\ \Delta(\boldsymbol{k})^{*} & -\xi(\boldsymbol{k}) \end{pmatrix} \begin{pmatrix} \psi_{\boldsymbol{k},\uparrow} \\ \psi^{\dagger}_{-\boldsymbol{k},\downarrow} \end{pmatrix} \tag{1.2}$$

Here, $\boldsymbol{k}$ is the quasiparticle momentum, ψ ($\psi^{\dagger}$) is the electron annihilation (creation) operator, $\xi(\boldsymbol{k})$ is the band energy relative to the chemical potential, and $\Delta(\boldsymbol{k})$ is the superconducting order parameter written as,

$$\Delta(\boldsymbol{k}) = -\sum_{\boldsymbol{k}'} V(\boldsymbol{k},\boldsymbol{k}')\langle \psi_{\boldsymbol{k}',\uparrow}\psi_{-\boldsymbol{k}',\downarrow}\rangle. \tag{1.3}$$

Here, $V(\boldsymbol{k},\boldsymbol{k}')$ is the interaction between electrons. It should be noted that the BCS mean field $\langle \psi_{\boldsymbol{k}',\uparrow}\psi_{-\boldsymbol{k}',\downarrow}\rangle$ spontaneously breaks the $U(1)$-gauge symmetry. We are able to diagonalize the BCS Hamiltonian using the Bogoliubov transformation. Therefore, the eigenvalue of Eq. (1.2) is given by:

$$E(\boldsymbol{k}) = \sqrt{\xi(\boldsymbol{k})^2 + |\Delta(\boldsymbol{k})|^2} \tag{1.4}$$

$E(\boldsymbol{k})$ means the energy of single particle excitation in the superconducting state. If $\Delta(\boldsymbol{k})$ is finite, the superconducting gap opens around the Fermi level. By calculating

$\langle \psi_{\boldsymbol{k}',\uparrow} \psi_{-\boldsymbol{k}',\downarrow} \rangle$, we get the gap equation:

$$\Delta(\boldsymbol{k}) = -\sum_{\boldsymbol{k}'} V(\boldsymbol{k}, \boldsymbol{k}') \frac{\Delta(\boldsymbol{k}')}{2E(\boldsymbol{k}')} \tanh\left(\frac{E(\boldsymbol{k}')}{2k_B T}\right) \tag{1.5}$$

The existence of the nontrivial solution ($\Delta(\boldsymbol{k}) \neq 0$) is a necessary and sufficient condition for the occurrence of superconductivity. In BCS theory, the pairing interaction mediated by phonons is assumed to be attractive and $\boldsymbol{k}$-independent:

$$V(\boldsymbol{k}, \boldsymbol{k}') = \begin{cases} -V & (|\xi(\boldsymbol{k})|, |\xi(\boldsymbol{k}')| < \hbar\omega_D) \\ 0 & (\text{otherwise}) \end{cases} \tag{1.6}$$

Here, $V > 0$ and ω_D is the Debye cutoff frequency. This type of interaction means on-site attractive interaction $-V(\boldsymbol{r}) \sim -\delta(\boldsymbol{r})$ in real space and leads to the $\boldsymbol{k}$-independent gap:

$$\Delta(\boldsymbol{k}) = \begin{cases} \Delta & (|\xi(\boldsymbol{k})| < \hbar\omega_D) \\ 0 & (\text{otherwise}) \end{cases} \tag{1.7}$$

Therefore, phonon-mediated superconductivity is characterized by the isotropic s-wave ($\ell = 0$) superconducting gap.

In the case of strongly correlated material, however, the superconductivity is not believed to be phonon-mediated, but can be due to an electronic correlation. Moreover, in contrast to the conventional BCS superconductor, pairing interactions become $\boldsymbol{k}$-dependent in strongly correlated material. For instance, in high-T_c cuprates, the AFM fluctuations play an important role in Cooper pairing because the superconducting phase is adjacent to the AFM phase. If we consider the spin fluctuation mechanism, the spin susceptibility is peaked at the magnetic ordering wave vector $\boldsymbol{Q} = (\pi, \pi)$. In fact, according to the random phase approximation (RPA), $V(\boldsymbol{q})$ of the singlet pairing is given by

$$V^s(\boldsymbol{q}) = U + \frac{3}{2} U^2 \chi_s(\boldsymbol{q}) - \frac{1}{2} U^2 \chi_c(\boldsymbol{q}). \tag{1.8}$$

Here, U is the on-site coulomb interaction, and $\chi_s(\boldsymbol{q})$ and $\chi_c(\boldsymbol{q})$ are the spin suscepti-

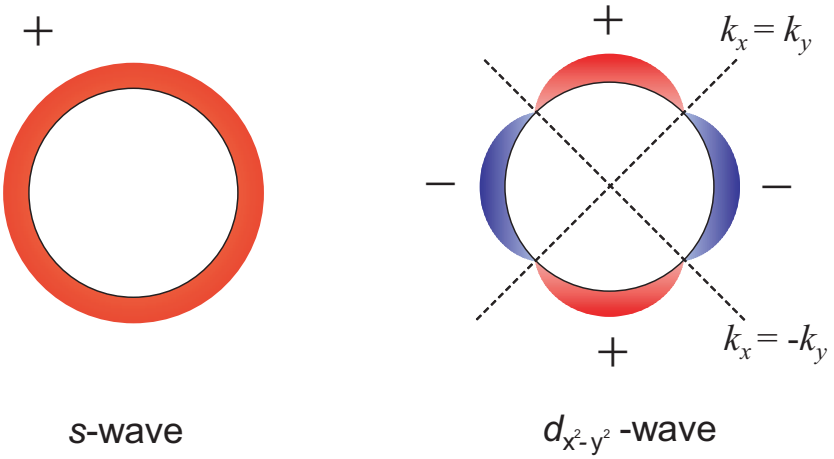

Figure 1.3: Superconducting order parameter for s-wave and $d_{x^2-y^2}$-wave

bility and charge susceptibility, respectively:

$$\chi_s(\boldsymbol{q}) = \frac{\chi_0(\boldsymbol{q})}{1 - U\chi_0(\boldsymbol{q})} \tag{1.9}$$

$$\chi_c(\boldsymbol{q}) = \frac{\chi_0(\boldsymbol{q})}{1 + U\chi_0(\boldsymbol{q})}. \tag{1.10}$$

Here, $\chi_0(\boldsymbol{q})$ is the susceptibility in the absence of interactions. In particular, the spin susceptibility is considerably larger than the charge susceptibility near the magnetic ordering ($U\chi_0(\boldsymbol{q}) \sim 1$). Therefore, the pairing interaction can be approximated by,

$$V^s(\boldsymbol{q}) \sim \frac{3}{2}U^2\chi_s(\boldsymbol{q}) = \frac{3}{2}U^2\frac{\chi_0(\boldsymbol{q})}{1 - U\chi_0(\boldsymbol{q})} \tag{1.11}$$

This implies that $V^s(\boldsymbol{q})$ also has a peak at the magnetic ordering wave vector $\boldsymbol{Q} = (\pi, \pi)$, but is always repulsive. For simplicity, we can approximate the spin susceptibility as $\chi_s(\boldsymbol{q}) \sim \delta(\boldsymbol{q} - \boldsymbol{Q})$. Then, the gap equation (1.5) is given by

$$\Delta(\boldsymbol{k}) \sim -U^2\frac{\tanh\left(E(\boldsymbol{k} - \boldsymbol{Q})/2k_BT\right)}{2E(\boldsymbol{k} - \boldsymbol{Q})}\Delta(\boldsymbol{k} - \boldsymbol{Q}). \tag{1.12}$$

Since $U^2\frac{\tanh(E(\boldsymbol{k}-\boldsymbol{Q})/2k_BT)}{2E(\boldsymbol{k}-\boldsymbol{Q})}$ is always positive, the order parameter must follow this equa-

tion to have non-trivial solution:

$$\Delta(\boldsymbol{k})\Delta(\boldsymbol{k}-\boldsymbol{Q})<0 \tag{1.13}$$

This implies that the superconducting gap changes its sign between the parts of the Fermi surfaces which are connected through the wave vector $\boldsymbol{Q}=(\pi,\pi)$. If the order parameter has B_{1g} symmetry [13], which is written as

$$\Delta(\boldsymbol{k})\propto \mathrm{cos}k_x-\mathrm{cos}k_y, \tag{1.14}$$

Eq. (1.13) is satisfied. In fact, several experiments that are sensitive to the phase of the superconducting order parameter reveal that the superconducting gap in the cuprates has B_{1g} symmetry [14–16]. This symmetry is commonly called $d_{x^2-y^2}$ wave symmetry ($\ell=2$). It should be noted that gap nodes (that is, zero gaps) appear along $k_x=\pm k_y$. In particular, the presence of gap nodes affects the transport and thermodynamic properties, which will be discussed in the next section.

1.5 Superconducting pairing symmetry

In this section, we will see the superconducting symmetry in more general sense. As mentioned in the previous section, the superconducting order parameter is expressed by the gap function $\Delta^{\ell}_{\boldsymbol{s_1},\boldsymbol{s_2}}(\boldsymbol{k})$, which is proportional to the amplitude of the Cooper pair wave function $\Psi^{\ell}_{\boldsymbol{s_1},\boldsymbol{s_2}}(\boldsymbol{k})=\langle\psi_{\boldsymbol{k},\boldsymbol{s_1}}\psi_{-\boldsymbol{k},\boldsymbol{s_2}}\rangle$. Here, ℓ is the orbital angular momentum and $\boldsymbol{s_i}$ is the electron spin. In the simplest case where the spin-orbit coupling is sufficiently weak, the total orbital angular momentum $\boldsymbol{L}$ and total spin $\boldsymbol{S}=\boldsymbol{s_1}+\boldsymbol{s_2}$ are good quantum numbers, and $\Delta^{\ell}_{\boldsymbol{s_1},\boldsymbol{s_2}}(\boldsymbol{k})$ can be separated into orbital and spin parts:

$$\Delta^{\ell}_{\boldsymbol{s_1},\boldsymbol{s_2}}(\boldsymbol{k})=g_{\ell}(\boldsymbol{k})\chi_s(\boldsymbol{s_1},\boldsymbol{s_2}). \tag{1.15}$$

The orbital part $g_{\ell}(\boldsymbol{k})$ can be expanded in terms of spherical harmonics $Y_{\ell m}(\hat{\boldsymbol{k}})$, which are the eigenfunctions of the orbital angular momentum operator with the momentum

ℓ and its z-projections m,

$$g_\ell(\boldsymbol{k}) = \sum_{m=-\ell}^{\ell} a_{\ell m}(k) Y_{\ell m}(\hat{\boldsymbol{k}}). \tag{1.16}$$

Here, $\hat{\boldsymbol{k}} = \boldsymbol{k}/k_F$ denotes the direction of the Fermi surface and $m = -\ell, -\ell{+}1, \cdots, \ell{-}1, \ell$ is the magnetic quantum number. Considering the parity of the spherical harmonics $Y_{\ell m}(\hat{\boldsymbol{k}})$, the orbital part $g_\ell(\boldsymbol{k})$ has even parity for even values of ℓ and odd parity for odd values of ℓ, namely, $g_\ell(\boldsymbol{k}) = (-1)^\ell g_\ell(-\boldsymbol{k})$. The Pauli exclusion principle requires $\Delta^\ell_{\boldsymbol{s_1},\boldsymbol{s_2}}(\boldsymbol{k})$ to be antisymmetric under particle interchange:

$$\Delta^\ell_{\boldsymbol{s_1},\boldsymbol{s_2}}(\boldsymbol{k}) = -\Delta^\ell_{\boldsymbol{s_2},\boldsymbol{s_1}}(-\boldsymbol{k}). \tag{1.17}$$

To satisfy the Eq. (1.17), either the spin part or orbital part must change its sign under the exchange of the two electrons. In the former case, ℓ is an even number, and spin singlet superconductivity is realized:

$$g_\ell(\boldsymbol{k}) = g_\ell(\boldsymbol{-k}), \quad \chi_s(\boldsymbol{s_1}, \boldsymbol{s_2}) = -\chi_s(\boldsymbol{s_2}, \boldsymbol{s_1}). \tag{1.18}$$

In the latter case, ℓ is an odd number, and spin triplet superconductivity is realized:

$$g_\ell(\boldsymbol{k}) = -g_\ell(\boldsymbol{-k}), \quad \chi_s(\boldsymbol{s_1}, \boldsymbol{s_2}) = \chi_s(\boldsymbol{s_2}, \boldsymbol{s_1}). \tag{1.19}$$

Superconductors with $\ell = 0, 1, 2, 3, 4, \ldots$ are labelled as having $S, P, D, F, G, \ldots$ wave gaps respectively. It should be noted that this classification is valid for an isotropic system. In a real system, almost all the superconductors have strong anisotropies. In that case, the superconducting gap symmetry must be classified by irreducible representations of the crystallographic point group. Strictly speaking, we should use irreducible representations of the space group. However, the crystallographic point group is enough for the discussion of the superconducting gap symmetry because the order parameter is spatially uniform for Cooper pairs with zero center-of-mass momentum. An example of the classification for D_{4h} symmetry is shown in Table 1.1.

Table 1.1: Classification of superconducting gap symmetry for D_{4h} symmetry.

SC gap symmetry	ℓ	$\Delta(\boldsymbol{k})(\propto)$	name	Irre. Rep.
S wave	0	$Y_{00}(\hat{\boldsymbol{k}}) \propto 1$	s wave	A_{1g}
P wave	1	$Y_{11}(\hat{\boldsymbol{k}}) - Y_{1-1}(\hat{\boldsymbol{k}}) \propto k_x$	p_x wave	E_u
		$Y_{11}(\hat{\boldsymbol{k}}) + Y_{1-1}(\hat{\boldsymbol{k}}) \propto k_y$	p_y wave	
		$Y_{10}(\hat{\boldsymbol{k}}) \propto k_z$	p_z wave	A_{2u}
D wave	2	$Y_{22}(\hat{\boldsymbol{k}}) + Y_{2-2}(\hat{\boldsymbol{k}}) \propto k_x^2 - k_y^2$	$d_{x^2-y^2}$ wave	B_{1g}
		$Y_{22}(\hat{\boldsymbol{k}}) - Y_{2-2}(\hat{\boldsymbol{k}}) \propto k_x k_y$	d_{xy} wave	B_{2g}
		$Y_{21}(\hat{\boldsymbol{k}}) - Y_{2-1}(\hat{\boldsymbol{k}}) \propto k_x k_z$	d_{xz} wave	E_g
		$Y_{21}(\hat{\boldsymbol{k}}) + Y_{2-1}(\hat{\boldsymbol{k}}) \propto k_y k_z$	d_{yz} wave	
		$Y_{20}(\hat{\boldsymbol{k}}) \propto 3k_z^2 - \lvert\boldsymbol{k}\rvert^2$	$d_{3z^2-r^2}$	A_{1g}
F wave	3	$Y_{33}(\hat{\boldsymbol{k}}) - Y_{3-3}(\hat{\boldsymbol{k}}) \propto k_x(k_x^2 - 3k_y^2)$	$f_{x(x^2-3y^2)}$ wave	E_u
		$Y_{33}(\hat{\boldsymbol{k}}) + Y_{3-3}(\hat{\boldsymbol{k}}) \propto k_y(k_y^2 - 3k_x^2)$	$f_{y(y^2-3x^2)}$ wave	
		$Y_{31}(\hat{\boldsymbol{k}}) - Y_{3-1}(\hat{\boldsymbol{k}}) \propto k_x(5k_z^2 - \lvert\boldsymbol{k}\rvert^2)$	$f_{x(5z^2-r^2)}$ wave	E_u
		$Y_{31}(\hat{\boldsymbol{k}}) + Y_{3-1}(\hat{\boldsymbol{k}}) \propto k_y(5k_z^2 - \lvert\boldsymbol{k}\rvert^2)$	$f_{y(5z^2-r^2)}$ wave	
		$Y_{32}(\hat{\boldsymbol{k}}) + Y_{3-2}(\hat{\boldsymbol{k}}) \propto k_z(k_x^2 - k_y^2)$	$f_{z(x^2-y^2)}$ wave	B_{2u}
		$Y_{32}(\hat{\boldsymbol{k}}) - Y_{3-2}(\hat{\boldsymbol{k}}) \propto k_x k_y k_z$	f_{xyz} wave	B_{1u}
		$Y_{30}(\hat{\boldsymbol{k}}) \propto k_z(5k_z^2 - 3\lvert\boldsymbol{k}\rvert^2)$	$f_{z(5z^2-3r^2)}$ wave	A_{2u}

Now, we go back to the gap function. The spin part $\chi_s(\boldsymbol{s_1}, \boldsymbol{s_2})$ is a product of the spinors for the two electrons. Therefore, the gap function is expressed by a 2×2 matrix in spin space:

$$\Delta_{\boldsymbol{S}}^{\ell} \equiv \Delta_{\boldsymbol{s_1},\boldsymbol{s_2}}^{\ell}(\boldsymbol{k}) = \begin{pmatrix} \Delta_{\uparrow\uparrow}^{\ell}(\boldsymbol{k}) & \Delta_{\uparrow\downarrow}^{\ell}(\boldsymbol{k}) \\ \Delta_{\downarrow\uparrow}^{\ell}(\boldsymbol{k}) & \Delta_{\downarrow\downarrow}^{\ell}(\boldsymbol{k}) \end{pmatrix}. \tag{1.20}$$

An arbitrary 2×2 matrix can be expanded in terms of four independent matrices: the unit matrix I and three Pauli matrices,

$$I = \begin{pmatrix} 1 & 0 \\ 0 & 1 \end{pmatrix}, \quad \sigma_x = \begin{pmatrix} 0 & 1 \\ 1 & 0 \end{pmatrix}, \quad \sigma_y = \begin{pmatrix} 0 & -i \\ i & 0 \end{pmatrix}, \quad \sigma_z = \begin{pmatrix} 1 & 0 \\ 0 & -1 \end{pmatrix}. \tag{1.21}$$

In the singlet state, $S = 0$, the spin part is $\chi_s(\boldsymbol{s_1}, \boldsymbol{s_2}) = |\uparrow\downarrow\rangle - |\downarrow\uparrow\rangle$ and is antisymmetric. Therefore, the gap function is given by

$$\Delta_{singlet}^{\ell}(\boldsymbol{k}) = \begin{pmatrix} 0 & \Delta_{\uparrow\downarrow}^{\ell}(\boldsymbol{k}) \\ -\Delta_{\uparrow\downarrow}^{\ell}(\boldsymbol{k}) & 0 \end{pmatrix} = \begin{pmatrix} 0 & \Delta g_\ell(\boldsymbol{k}) \\ -\Delta g_\ell(\boldsymbol{k}) & 0 \end{pmatrix} = \Delta g_\ell(\boldsymbol{k}) i\sigma_y, \tag{1.22}$$

where ℓ is an even number. The energy of single particle excitation in the singlet state is given by

$$E(\boldsymbol{k}) = \sqrt{\xi(\boldsymbol{k})^2 + \Delta^2 |g_\ell(\boldsymbol{k})|^2}. \tag{1.23}$$

For s-wave superconductors ($\ell = 0, m = 0$), $g_\ell(\boldsymbol{k}) \propto 1$. Therefore, the superconducting gap is isotropic and the excitations have a finite energy gap everywhere at the Fermi surface. On the other hand, for superconductors with finite $\ell = 2, 4, \ldots$, the gap amplitude will be anisotropic due to the component of $g_\ell(\boldsymbol{k})$.

In the triplet state, $S = 1$, the wave function has components corresponding to the three different spin projections, S_z, on the quantization axis ($|\uparrow\uparrow\rangle, |\uparrow\downarrow\rangle + |\downarrow\uparrow\rangle, |\downarrow\downarrow\rangle$). In this case, the spin part is symmetric under the exchange of electrons. Therefore, the

gap function can be written as

$$\Delta^{\ell}_{triplet}(\boldsymbol{k}) = \begin{pmatrix} g^1_\ell(\boldsymbol{k}) & g^2_\ell(\boldsymbol{k}) \\ g^2_\ell(\boldsymbol{k}) & g^3_\ell(\boldsymbol{k}) \end{pmatrix}, \tag{1.24}$$

where $g^\alpha_\ell(\boldsymbol{k})$ is given by

$$g^\alpha_\ell(\boldsymbol{k}) = \sum_{m=-\ell}^{\ell} a^\alpha_{\ell m}(k) Y_{\ell m}(\hat{\boldsymbol{k}}), \quad \alpha = 1, 2, 3. \tag{1.25}$$

On the other hand, Eq. (1.24) can be rewritten in terms of symmetric matrices $i\boldsymbol{\sigma}\sigma_y$ and the $\boldsymbol{d}$-vector:

$$\Delta^{\ell}_{triplet}(\boldsymbol{k}) = i(\boldsymbol{d}(\boldsymbol{k}) \cdot \boldsymbol{\sigma})\sigma_y = \begin{pmatrix} -d_x(\boldsymbol{k}) + id_y(\boldsymbol{k}) & d_z(\boldsymbol{k}) \\ d_z(\boldsymbol{k}) & d_x(\boldsymbol{k}) + id_y(\boldsymbol{k}) \end{pmatrix}. \tag{1.26}$$

The orbital part is expressed by these $\boldsymbol{d}$-vectors with

$$g^1(\boldsymbol{k}) = -d_x(\boldsymbol{k}) + id_y(\boldsymbol{k}), \quad g^2(\boldsymbol{k}) = d_z(\boldsymbol{k}), \quad g^3(\boldsymbol{k}) = d_x(\boldsymbol{k}) + id_y(\boldsymbol{k}), \tag{1.27}$$

and the excitation energy is given by

$$E(\boldsymbol{k}) = \sqrt{\xi(\boldsymbol{k})^2 + \Delta^2(|\boldsymbol{d}(\boldsymbol{k})|^2 \pm |\boldsymbol{d}^*(\boldsymbol{k}) \times \boldsymbol{d}(\boldsymbol{k})|)}. \tag{1.28}$$

If $\boldsymbol{d}(\boldsymbol{k})$ is unitary, $\boldsymbol{d}^*(\boldsymbol{k}) \times \boldsymbol{d}(\boldsymbol{k}) = 0$, and Eq. (1.28) can be rewritten as

$$E(\boldsymbol{k}) = \sqrt{\xi(\boldsymbol{k})^2 + \Delta^2|\boldsymbol{d}(\boldsymbol{k})|^2}. \tag{1.29}$$

1.6 Low temperature properties

The low temperature properties of superconductors are governed by the low-energy quasiparticle excitations. Therefore, the important quantity which determines the physical properties is the quasiparticle density of states. As will become clear in the next

section, the topology of the nodes in the gap function is very decisive in this respect.

1.6.1 Quasiparticle density of states

The density of states is defined as

$$N(E) = \sum_{\boldsymbol{k}} \delta(E(\boldsymbol{k}) - E) \tag{1.30}$$

where $E(\boldsymbol{k})$ is the quasiparticles spectrum

$$E(\boldsymbol{k}) = \sqrt{\xi(\boldsymbol{k})^2 + |\Delta(\boldsymbol{k})|^2}. \tag{1.31}$$

We can write the density of states in the superconducting state by using that of the normal state N_0:

$$\frac{N(E)}{N_0} = \int \frac{d\Omega}{4\pi} \mathrm{Re} \frac{E}{\sqrt{E^2 - \Delta(\Omega)^2}}. \tag{1.32}$$

The density of states for an isotropic s-wave superconductivity ($\Delta(\Omega) = \Delta$) is given by

$$\frac{N(E)}{N_0} = \begin{cases} 0 & (|E| < \Delta) \\ \dfrac{E}{\sqrt{E^2 - \Delta^2}} & (|E| \geq \Delta) \end{cases}. \tag{1.33}$$

The quasiparticle density of states is zero with energy below the gap and diverges at $E = \Delta$. At higher energies, $N(E)$ approaches the normal state value N_0.

Now, we discuss the density of states for unconventional superconductivity. For example, p -wave superconductivity ($\ell = 1$) in the isotropic system has two kinds of gap structure which reflect the spherical harmonics. One is $\Delta(\Omega) = \Delta \cos\theta$, which corresponds to $\ell = 1, m = 0$, and the other is $\Delta(\Omega) = \Delta \sin\theta e^{\pm i\phi}$, which corresponds to $\ell = 1, m = \pm 1$. In the former case, line node appears at $\theta = \pi/2$, which is called the polar state. In the latter case, point node appears at $\theta = 0, \pi$, which is called the axial state.

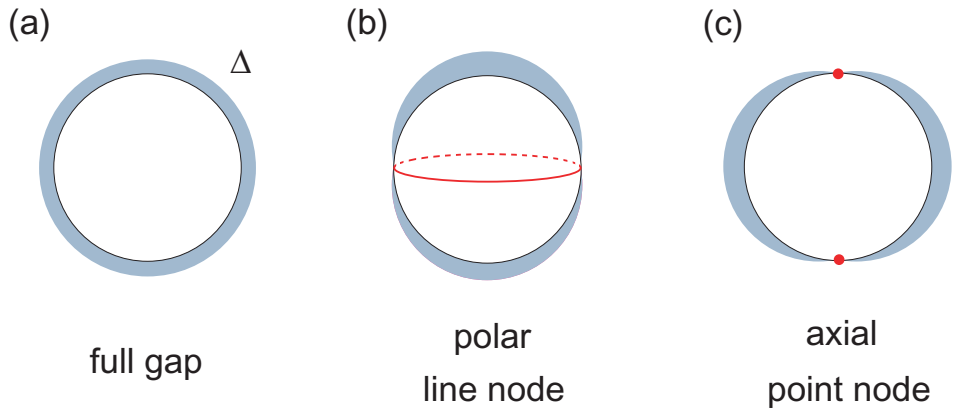

Figure 1.4: Schematic figures of the superconducting gap structure for the (a) fully gapped state, (b) polar state, and (c) axial state. The red thick line and points represent the line node and point nodes, respectively.

The density of states of polar state is given by

$$\begin{aligned}\frac{N(E)}{N_0} &= \frac{E}{4\pi}\int_0^{2\pi}\int_0^{\pi} \mathrm{Re}\left(\frac{\sin\theta}{\sqrt{E^2-\Delta^2\cos^2\theta}}\right) d\theta d\phi \\ &= \begin{cases} \dfrac{\pi}{2}\dfrac{E}{\Delta} & (|E|<\Delta) \\ \dfrac{E}{\Delta}\arcsin\left(\dfrac{\Delta}{E}\right) & (|E|\geq\Delta) \end{cases} \end{aligned} \tag{1.34}$$

A finite density of states is found below the gap, down to zero energy. It should be noted that the quasiparticle density of states is proportional to E at low energies and vanishes at zero energy in the clean limit.

The density of states of the axial state is given by

$$\begin{aligned}\frac{N(E)}{N_0} &= \frac{E}{4\pi}\int_0^{2\pi}\int_0^{\pi} \mathrm{Re}\left(\frac{\sin\theta}{\sqrt{E^2-\Delta^2\sin^2\theta}}\right) d\theta d\phi \\ &= \frac{E}{2\Delta}\ln\left|\frac{E+\Delta}{E-\Delta}\right| \qquad (1.35) \\ &\propto E^2 (|E|\ll\Delta). \qquad (1.36)\end{aligned}$$

In the case of point nodes, the density of states is proportional to E^2 at low energies.

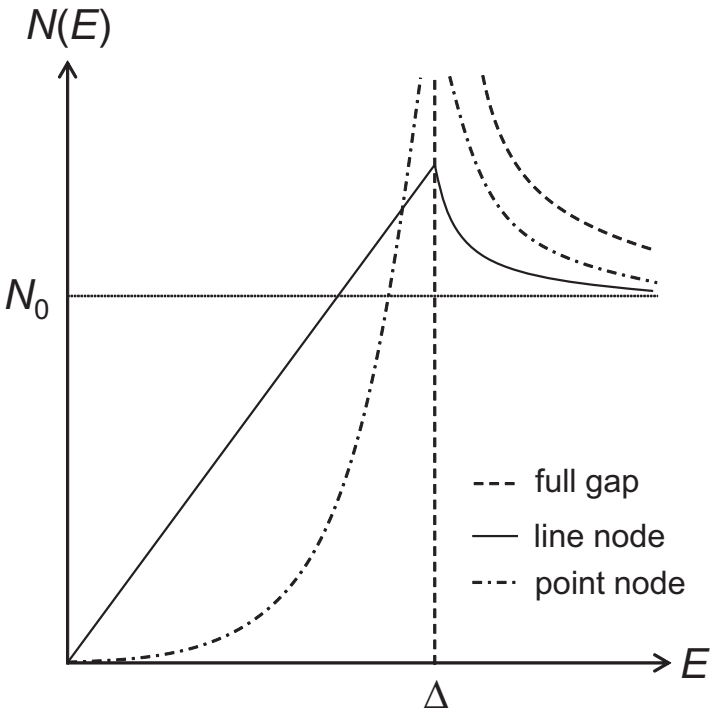

Figure 1.5: Schematic figures of quasiparticle density of states $N(E)$ for full gap (dotted line), line node (solid line), and point node cases (chain line) in the clean limit.

Summarizing the above, the energy dependence of the quasiparticle density states at low energies in the clean limit is

$$\frac{N(E)}{N_0} \propto \begin{cases} 0 & \text{(full gap)} \\ E & \text{(polar state)} \\ E^2 & \text{(axial state)} \end{cases} \tag{1.37}$$

1.6.2 Low-temperature thermodynamics

In this section, we examine the influence of the node topology on the low temperature properties using the several examples.

- **Specific heat**

We now examine the temperature dependence of the specific heat $C(T)$ at $T \ll T_c$. In

this temperature regime, the gap magnitude has saturated and does not change much anymore. Therefore, the temperature dependence of $C(T)$ is dominated by $N(E)$. $C(T)$ is given by

$$\begin{aligned} C(T) &= \frac{2}{\Omega}\sum_{\boldsymbol{k}} E(\boldsymbol{k})\frac{df(E(\boldsymbol{k}))}{dT} = \int dE N(E)\frac{df(E)}{dT} \\ &= \int dE N(E)\frac{E^2}{k_B T^2}\frac{1}{4\cosh^2(E/2k_BT)}, \end{aligned} \tag{1.38}$$

where $f(E) = 1/(e^{\beta E}+1)$ is the Fermi distribution function and $\beta = \frac{1}{k_B T}$. Substituting Eq. (1.37) into Eq. (1.38), we can obtain $C(T)$ for each state.

For the full gap state,

$$C(T) \approx \frac{N_0}{4k_BT^2}\int_{\Delta}^{\infty} dE \frac{E^3}{\sqrt{E^2-\Delta^2}} e^{-E/k_BT} \approx N_0 k_B \sqrt{2\pi k_B T \Delta}\left(\frac{\Delta}{k_BT}\right)^2 e^{-\Delta/k_BT} \tag{1.39}$$

Therefore, $C(T)$ exhibits exponential temperature dependence (thermally activated type) at $T \ll T_c$ in the full gap state.

For the polar and axial states, on the other hand, the thermally activated behavior is changed due to the low-lying quasiparticles. As discussed in the previous section, the density of states exhibits power law behavior $N(E) \propto E^n$ at $E \ll \Delta$, where $n = 1$ for the polar state and $n = 2$ for the axial state. Then, $C(T)$ is given by

$$C(T) \propto \int dE E^n \frac{E^2}{k_BT^2}\frac{1}{4\cosh^2(E/2k_BT)} \propto T^{n+1}. \tag{1.40}$$

Therefore, $C(T)$ shows power law temperature dependence at $T \ll T_c$ in the nodal state.

Summarizing the above, the temperature dependences of $C(T)$ in the clean limit are

$$C(T) \propto \begin{cases} \exp(-\Delta/k_BT) & \text{(full gap)} \\ T^2 & \text{(polar state)} \\ T^3 & \text{(axial state)} \end{cases} \tag{1.41}$$

- **Penetration depth**

The penetration depth λ is one of the most important quantities of superconductivity because λ is directly connected to the superfluid density n_s. In fact, measurement of λ is known to be a powerful probe for elucidating the superconducting gap structure.

In the superconducting state, the magnetic field decreases exponentially from the surface going into the bulk. By defining $B(0)$ as the magnetic field parallel to the surface, the magnetic field from the surface is given by [17]

$$B(x) = B(0)\exp(-x/\lambda_L). \tag{1.42}$$

Here, λ_L is the London penetration depth:

$$\lambda_L = \left(\frac{4\pi n_s e^2}{m^* c^2}\right)^{-1/2}, \tag{1.43}$$

where m^* is the effective mass and c is the speed of light. In the superconducting state, the normal fluid density n_n is given by

$$n_n = n\int dE \frac{N(E)}{N_0}\left(-\frac{\partial f}{\partial E}\right). \tag{1.44}$$

Here, we assume the simple two-fluid model. In this model, the total carrier density n is described by

$$n = n_s + n_n. \tag{1.45}$$

For the full gap state, we obtain the normal fluid density by calculating Eq. (1.44) at $T \ll T_c$:

$$n_n(T) = n\sqrt{\frac{2\pi\Delta}{k_B T}}\exp\left(-\frac{\Delta}{k_B T}\right). \tag{1.46}$$

Then, we obtain λ from Eq. (1.43),

$$\begin{aligned}\lambda(T) &= \left(\frac{4\pi(n-n_n)e^2}{m^* c^2}\right)^{-1/2} \\ &= \lambda(0)\left[1+\sqrt{\frac{\pi\Delta}{2k_B T}}\exp\left(-\frac{\Delta}{k_B T}\right)\right].\end{aligned} \tag{1.47}$$

For the polar state, the normal fluid density is calculated by substituting Eq. (1.37) into Eq. (1.44):

$$n_n(T) \approx 2n\frac{\ln 2}{\Delta}k_B T, \tag{1.48}$$

then we obtain the penetration depth:

$$\lambda(T) \approx \lambda(0)\left(1 + \frac{\ln 2}{\Delta}k_B T\right). \tag{1.49}$$

For the axial state, we can obtain the penetration depth in the same way. Finally, we can summarize the temperature dependence of λ as follows:

$$\lambda(T) \propto \begin{cases} \exp(-\Delta/k_B T) & \text{(full gap)} \\ T & \text{(polar state)} \\ T^2 & \text{(axial state)} \end{cases} \tag{1.50}$$

Table 1.2: The energy dependence of $N(E)$ and the temperature dependence of several quantities for each gap structure at low energies.

Quantity	Full gap	Polar (line nodes)	Axial (point nodes)
Density of states $N(E)$	0	E	E^2
Specfic heat $C(T)$	$\exp(-1/T)$	T^2	T^3
Penetration depth $\lambda(T)$	$\exp(-1/T)$	T	T^2
NMR relaxation rate $1/T_1$	$\exp(-1/T)$	T^3	T^5

The temperature dependences of the specific heat, penetration depth, and NMR relaxation rate for each gap structure are summarized in Table 1.2. Therefore, we can distinguish the types of the superconducting gap structure from the temperature dependences of those physical quantities at low-T. It should be noted that the above discussion is restricted to clean-limit systems without impurities. The introduction of impurities sensitively affects the quasiparticle density of states in an unconventional

superconductor. This effect will be discussed in the next section.

1.7 Impurity effect

The response to non-magnetic impurities is significantly different between sign-preserving and sign-reversing superconductivity because impurity scattering mixes the gaps on different parts of the Fermi surface. Therefore, the impurity effect has long been used as a phase-sensitive probe to determine the superconducting gap function.

1.7.1 Impurity effect on critical temperature

In conventional s-wave superconductors, although a non-magnetic impurity scatters the time-reversed pair ($\boldsymbol{k}\uparrow$, $-\boldsymbol{k}\downarrow$) to another wave vector, time-reversal symmetry is still preserved. Therefore, T_c is little affected by non-magnetic impurities. This fact is called Anderson's theorem [18].

On the other hand, magnetic impurities act as pair-breaking centers since their interaction with the electrons breaks the time-reversal symmetry of the two members of each Cooper pair. This leads to a disturbance of the relative phase of the Cooper pair wave function and then significantly reduces the T_c. The depression of the critical temperature due to magnetic impurities is well described by the Abrikosov-Gor'kov (AG) formula [19]:

$$\begin{aligned} \ln\frac{T_c}{T_{c0}} &= \psi\left(\frac{1}{2}\right) - \psi\left(\frac{1}{2}+\frac{\gamma}{2\pi k_B T_c}\right) \\ T_{c0} - T_c &= \frac{\pi\gamma}{4k_B} \qquad (\gamma \sim 0), \end{aligned} \tag{1.51}$$

where T_{c0} is the transition temperature without pair-breaking, $\gamma \equiv \hbar/2\tau_k$ (τ_k : scattering time) is the pair-breaking parameter, and ψ is the digamma function. In addition, as the pair-breaking parameter increases, a finite density of states appears at the Fermi energy. The quasiparticle density of states in the presence of magnetic impurities is described in Figure 1.6 [20].

In an unconventional superconductor, on the other hand, the gap function is anisotropic

and strongly k-dependent. For example, in d-wave superconductors, the phase of the superconducting gap function changes its sign around the Fermi surface. This sign change makes the superconductor much more sensitive to non-magnetic impurities. This results in a strong depression of T_c, even by non-magnetic impurities. In fact, the depression of T_c due to isotropic non-magnetic impurity scattering is calculated by A. I. Larkin [21], which is identical to the Eq. (1.51). This pair-breaking effect is confirmed by, for example, the d-wave superconductor $CeCoIn_5$ [22].

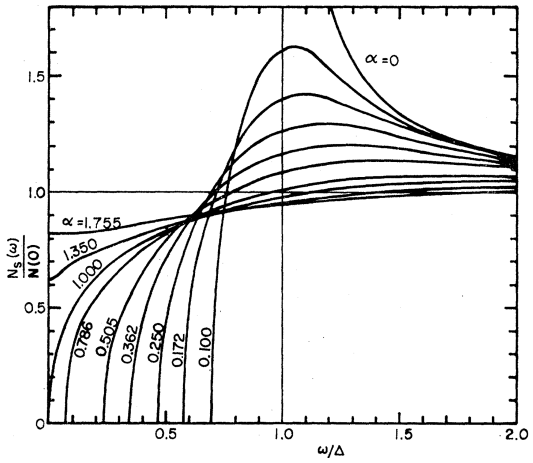

Figure 1.6: Quasiparticle density of states in the presence of magnetic impurities in a conventional s-wave superconductor [20].

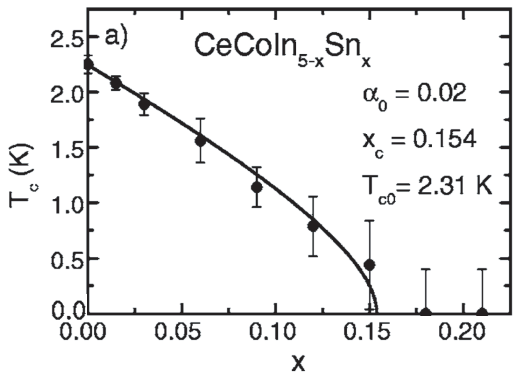

Figure 1.7: Superconducting transition temperature T_c vs. Sn doping x of the d-wave superconductor $CeCoIn_{5-x}Sn_x$. The solid line represents the AG pair-breaking formula. Experimental results are well fitted by the AG formula [22].

1.7.2 Impurity effect on the quasiparticle density of states in an unconventional superconductor

Impurity effects are characterized by the scattering phase shift δ_0, related to the impurity potential strength. Impurity scattering is often treated in two ways. One is the Born approximation, which is valid for a weak scattering potential with a small phase shift. The other is the unitary limit, which is the strong scattering limit with $\delta_0 = \pi/2$. The difference between these two limits plays an important role, especially in unconventional superconductors. In fact, we cannot explain some experimental results in heavy-fermion materials so long as one uses the Born approximation for the impurity scattering. For example, the temperature dependence of the thermal conductivity and ultrasonic attenuation in the superconducting state remains the same as those in the normal state. This problem was resolved when calculated in the unitary limit [23]. It is thought that impurities should be treated in the unitary limit, especially in heavy-fermion superconductors.

For nodal superconductors in the unitary limit, quasiparticle states are bound to a non-magnetic impurity with energy close to the Fermi energy within the energy gap. This is a consequence of the formation of the Andreev bound states. As a result, a residual density of states $N(0)$ appears at $E = 0$ and the energy dependence of the quasiparticle density of states is modified, as shown in Figure 1.8. It should be noted that $N(0)$ appears in both polar and axial states even though the pair-breaking effect is significantly weaker. This fact is opposite to the fully gapped s-wave case in which $N(0)$ appears just before the superconductivity is destroyed, as shown in Figure 1.6. In the polar state with line nodes, a residual density of states is given by

$$\frac{N(0)}{N_0} \sim \sqrt{\frac{\gamma}{\Delta} \ln \frac{2\Delta}{\gamma}}. \tag{1.52}$$

Moreover, the appearance of $N(0)$ affects the temperature dependences of the physical quantities at $k_B T < \gamma$ because $N(0)$ dominates the thermodynamic and transport properties in this temperature regime. The impurity effect on several physical quantities

is summarized in Table 1.3.

As we have seen above, the impurity effect on physical properties, including the T_c, quasiparticle density of states, and thermodynamics, is significantly different between conventional and unconventional superconductivity. Therefore, the impurity effect is used as a phase-sensitive test to determine the superconducting gap structure.

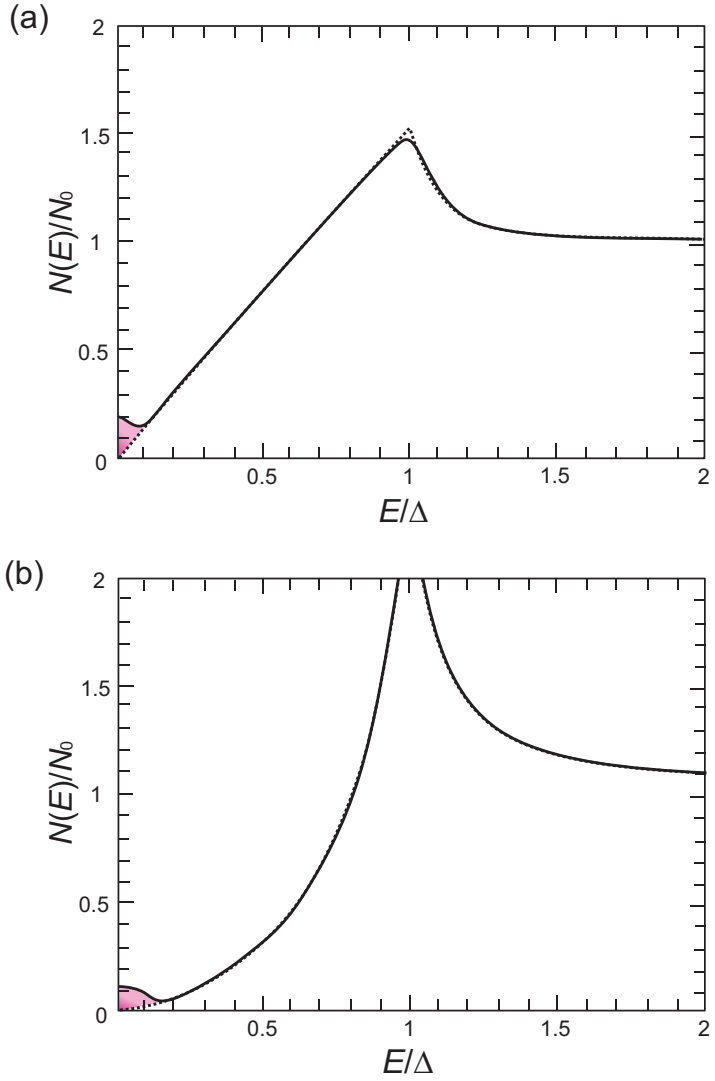

Figure 1.8: The quasiparticle density of states in the presence of non-magnetic impurities for polar (a) and axial (b) states [23]. The dashed line indicates $N(E)$ in the absence of impurities. The solid line indicates the $N(E)$ in the unitary limit with $\gamma/\Delta = 0.01$. The residual density of states $N(0)$ appears due to the impurity scattering.

Table 1.3: Temperature dependence of several physical quantities in superconductors with line nodes for a clean system and for a system with impurities.

Quantity	Clean limit	With impurities
specfic heat $C(T)$	T^2	T
penetration depth $\lambda(T)$	T	T^2
NMR relaxation rate $1/T_1$	T^3	T

1.8 Nodal superconductor in a magnetic field: Doppler shift

In the mixed state, the magnetic field response of a fully gapped superconductor and a nodal superconductor is significantly different. Therefore, the magnetic field response also can be useful probe to determine the superconducting gap structure. In order to comprehend the origin of the difference, we discuss the effect of the Doppler shift in this section.

When a magnetic field is applied on type-II superconductors, the field enters as the Abrikosov vortices with a unit of quantum flux $\Phi_0 = \frac{\hbar}{2\mathrm{e}}$, and they form an Abrikosov lattice. In the mixed state, the quasiparticle spectrum is Doppler shifted by the supercurrent flow $\boldsymbol{v}_s$ circulating around the vortices:

$$E(\boldsymbol{p}) \to E(\boldsymbol{p}) - \boldsymbol{v}_s \cdot \boldsymbol{p}. \tag{1.53}$$

In an s-wave superconductor (without gap nodes), the quasiparticle density of states at low fields, $H \ll H_{c2}$, is determined by the localized states in the vortex cores:

$$N_{\mathrm{loc}}(0) = N_0 \xi^2 \frac{H}{H_{c2}}, \tag{1.54}$$

where ξ is the coherence length [24]. This H-linear behavior, for example, is detected

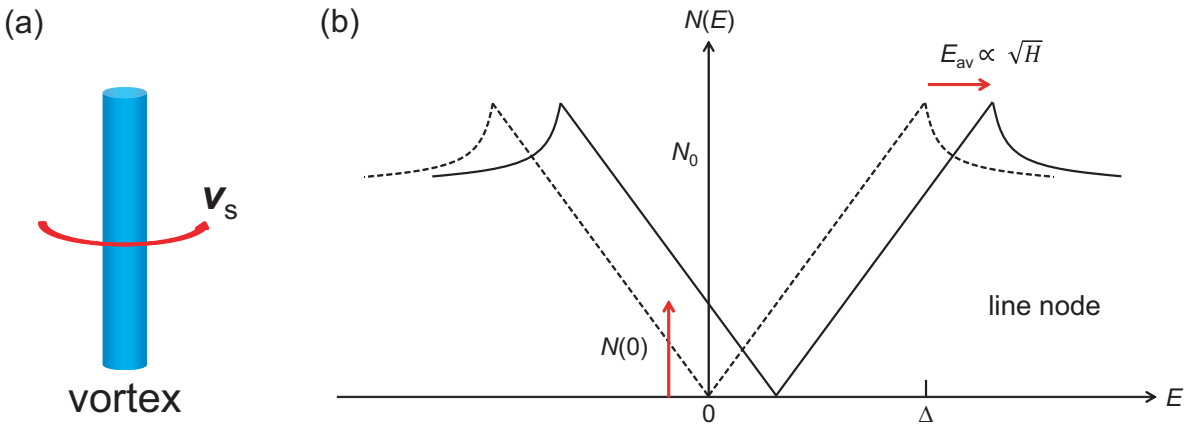

Figure 1.9: (a) Schematic figure of the Abrikosov vortex in type-II superconductors. (b) Schematic figure of the appearance of the residual density of states $N(E = 0, H)$ induced by the Doppler shift in the system with line nodes. The dashed line represents the $N(E)$ in zero field. The solid line represents the $N(E)$ in the mixed state.

through the specific heat. However, low-lying quasiparticle states do not influence the heat transport properties, such as thermal conductivity, because they are bound to vortex cores and cannot carry heat, which will be discussed in a later section.

On the other hand, in the nodal superconductor, the main contribution to the quasiparticle density of states comes from the vicinity of the gap nodes in $\boldsymbol{k}$-space and from the region outside the vortex core, namely, delocalized quasiparticles rather than localized quasiparticles [25]. Indeed, the Doppler shift becomes important due to such delocalized quasiparticles in the nodal superconductor.

To estimate the Doppler shifted energy, we can approximate the velocity field by that around a single vortex, $\boldsymbol{v}_s = \hbar\hat{\phi}/2m_e r$, where r is the distance from the center of the vortex and $\hat{\phi}$ is a unit vector along the circulating current. This expression is valid outside the vortex core and up to a cut-off of order $\min\{R, \lambda\}$, where $R = a\sqrt{\Phi_0/\pi H}$ is the inter-vortex distance and a is a geometric constant. The average Doppler shifted energy, $E_{\rm av}$, is calculated by integrating over a vortex lattice unit cell, and is given by

$$E_{\rm av} = \langle |\boldsymbol{v}_s \cdot \boldsymbol{p}| \rangle = \int_{|r|<R} \frac{\mathrm{d}^2\boldsymbol{r}}{\pi R^2} |\boldsymbol{v}_s \cdot \boldsymbol{p}| \simeq \frac{4}{a\pi} \hbar v_F \sqrt{\frac{H}{\Phi_0}}. \tag{1.55}$$

Table 1.4: The residual density of states $N(E=0,H)$ induced by the Doppler shift for superconductors with line nodes and point nodes. $N(E=0,H)$ is proportional to $\sqrt{H}$ and H for line nodes and point nodes, respectively.

Quantity	Line node	Point node
$N(E)$ at $E \ll \Delta$	E	E^2
$N(E=0,H)$	$\sqrt{H}$	H

Therefore, $E_{\rm av} \propto \sqrt{H}$ [26]. As discussed in the previous section, since the quasiparticle density of states $N(E)$ is proportional to E for a polar state at $E \ll \Delta$, a Doppler-shift-induced residual density of states $N(E=0,H)$ appears and is proportional to $E_{\rm av} \propto \sqrt{H}$. Therefore, $\sqrt{H}$-dependence is expected for physical quantities such as specific heat and thermal conductivity in a superconductor with line nodes. The field dependence of $N(E=0,H)$ is summarized in Table 1.4.

1.9 Thermal conductivity

Thermal conductivity measurement is known to be a powerful probe to investigate the superconducting gap structure. Indeed, contrary to the electrical resistivity, thermal conductance does not vanish in the superconducting state because quasiparticle excitations carry heat while Cooper pairs do not. As a result, the thermal conductivity measurement probes the delocalized low-energy quasiparticle excitations.

1.9.1 Temperature dependence

The thermal conductivity can be written as a sum of the electron and phonon contributions, $\kappa = \kappa_{el} + \kappa_{ph}$. Assuming the kinetic approximation, electronic thermal conductivity is given by [27],

$$\kappa_{el} = \frac{1}{3} C_{el} v_F l = \frac{1}{3} C_{el} v_F^2 \tau, \tag{1.56}$$

where C_{el} is the electron specific heat, v_F is the Fermi velocity, and $l = v_F\tau$ is the mean free path. By substituting the expression of C_{el} into Eq. (1.56), then we have

$$\frac{\kappa_{el}}{T} \propto N(0)v_F^2\tau, \tag{1.57}$$

where $N(0)$ is the density of states at the Fermi energy. Using the Drude conductivity $\sigma = ne^2\tau/m$, we get the relation between electronic thermal and electrical conductivities,

$$\frac{\kappa_{el}}{T} = \sigma L_0, \tag{1.58}$$

where $L_0 = (\pi^2/3)(k_B/e)^2 = 2.44 \times 10^{-8}$ WΩK^{-2} is the Lorenz number. This is the Wiedemann-Franz law. By using this, we can also estimate κ_{ph}/T $(= \kappa/T - L_0/\rho)$.

The phonon thermal conductivity can be expressed in a similar fashion. At a sufficiently low temperature, κ_{ph} in the boundary-limited scattering regime is expressed as,

$$\kappa_{ph} = \frac{1}{3}\beta\langle v_s\rangle l_{ph}T^3, \tag{1.59}$$

where β is the phonon specific heat coefficient, $\langle v_s\rangle$ is the mean acoustic phonon velocity, and l_{ph} is the phonon mean free path. For the diffuse scattering limit, l_{ph} becomes T-independent, resulting in $\kappa_{ph} \propto T^3$. On the other hand, in the case of specular reflection, l_{ph} follows a T^{-1}-dependence, leading to $\kappa_{ph} \propto T^2$. In real systems,

$$\frac{\kappa_{ph}}{T} \propto T^{\alpha-1}, \tag{1.60}$$

with α of intermediate value between 2 and 3. In fact, α = 2.74, 2.4, and 2.77 have been reported in V_3Si [28], $YBa_2Cu_3O_{6.99}$ [28], and Al_2O_3 [29], respectively.

By taking the sum of Eq. (1.57) and (1.60), the total thermal conductivity at the lowest temperatures $(T \ll \gamma/k_B)$ is written as

$$\frac{\kappa}{T} = \frac{\kappa_{00}}{T} + AT^{\alpha-1}, \tag{1.61}$$

where κ_{00}/T is the residual term (intercept coefficient) at $T = 0$ and A is a constant.

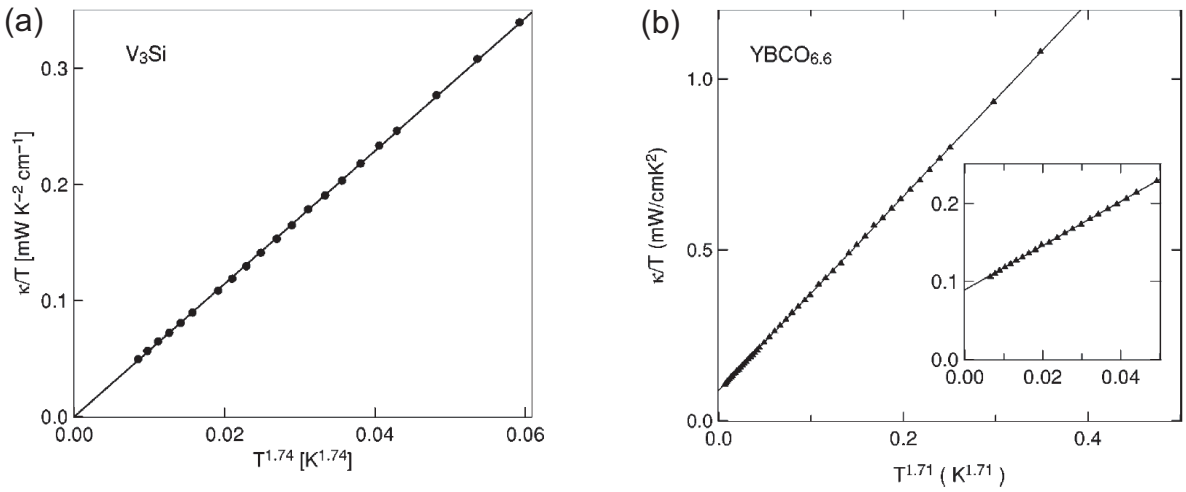

Figure 1.10: (a) κ/T vs $T^{1.74}$ in the s-wave superconductor V_3Si [28]. No κ_{00}/T is observed. (b) κ/T vs $T^{1.71}$ in the d-wave superconductor $YBa_2Cu_3O_{6.99}$ [28]. The residual κ_{00}/T is observed.

Therefore, we can discuss the superconducting gap structure by plotting the data as described in Eq. (1.61) and the extrapolation to $T \to 0$ in zero field. Indeed, in the fully-gapped superconductor, κ_{00}/T is zero because the residual $N(0) = 0$ (Figure 1.10 (a)). On the other hand, as discussed in Sec. 1.7.2, a finite $N(0)$ appears in the nodal superconductor in the presence of non-magnetic impurities. Therefore, the residual thermal conductivity κ_{00}/T appears in the nodal superconductor (Figure 1.10 (b)).

It should be noted that κ_{00}/T is independent of the impurity concentration in the line-nodal superconductor. This is because the residual density of states $N(0)$ increases while τ decreases from introducing the non-magnetic impurity, i.e., $N(0) \propto \gamma$ and $\tau \propto \gamma^{-1}$, where γ is the impurity band width. This compensation between $N(0)$ and τ leads to a universal κ_{00}/T. κ_{00}/T for line-nodal superconductors in the unitary limit is given by [30]

$$\frac{\kappa_{00}}{T} \approx \frac{L_0}{\rho_0}\frac{\xi}{l}, \tag{1.62}$$

where ξ is the coherence length.

1.9.2 Field dependence

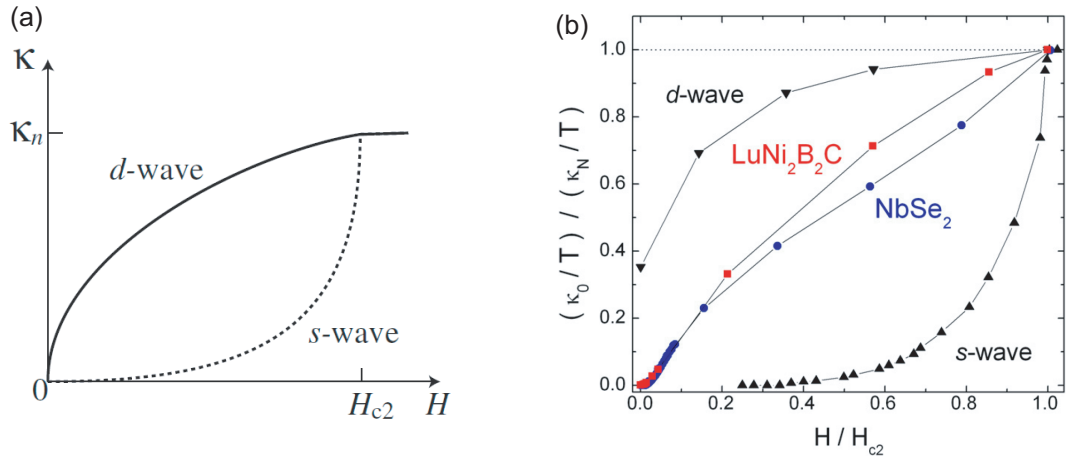

Figure 1.11: (a) Schematic figure of κ vs. H in the fully-gapped and nodal superconductor. Adapted from [26]. (b) (κ_0/T) normalized by κ_0/T in the normal state vs. H/H_{c2} for elemental Nb (▲, s-wave), $NbSe_2$ (multiband s-wave), $LuNi_2B_2C$ (highly anisotropic multiband SC), and overdoped cuprate Tl-2201 (▼, d-wave) [31].

The field dependence of the thermal conductivity also provides detailed knowledge about the superconducting gap structure. It is well established that there is an essential difference in the field dependence of the thermal conductivity between fully gapped and nodal superconductors [26]. In the former, all the quasiparticles states are bound to vortex cores and, therefore, the applied magnetic field hardly affects the thermal conduction except for in the vicinity of the upper critical field where the vortices overlap with the neighboring vortices (dashed line in Figure 1.11 (a)). It should be noted that the single exponential behavior can be modified if the system is a multiband s-wave and/or anisotropic s-wave. For example, $NbSe_2$ is a multiband s-wave superconductor, in which different Fermi surfaces exhibit different gap values. Indeed, the large gap is known to be about three times larger than the small gap. This indicates that a field H^* $\approx H_{c2}(0)/9$ will be enough to suppress the superconductivity of the Fermi surface with a small gap. In fact, the shoulder feature appears in κ_0/T vs H at about H^*, which indicates the suppression of the superconductivity with a small gap (Figure 1.11 (b)).

By contrast, in the nodal superconductor, the heat transport is dominated by delocalized quasiparticles. In the presence of a supercurrent with a velocity $\boldsymbol{v}_s$ around

the vortices induced by a magnetic field, the energy of a quasiparticle with momentum $\boldsymbol{p}$ is Doppler shifted relative to the superconducting condensate by $E(\boldsymbol{p}) \to E(\boldsymbol{p}) - \boldsymbol{v}_s \cdot \boldsymbol{p}$. Since $\kappa_{el}/T \propto N(0) v_F^2 \tau$, the Doppler shift gives rise to an initial steep increase of $\kappa(H) \propto \sqrt{H}$ for line nodes and $\kappa(H) \propto H \log H$ for point nodes.

As seen above, thermal conductivity measurement is a powerful probe to determine the superconducting gap structure.

2 Purpose of this study

As discussed above, strongly correlated materials have been one of the most fascinating systems in modern physics. They exhibit a rich variety of exotic phenomena such as non-Fermi liquid behaviour, exotic orders, coexistence of superconductivity and magnetic or exotic orders, and so on. In particular, unconventional superconductivity in the vicinity of the magnetic instability has also attracted much attention. As discussed in section 1.4, the superconducting gap structure is intimately related to the pairing mechanism. Therefore, it is important to determine the superconducting gap structure. In order to do this, we perform the thermal conductivity measurement, which is known to be a powerful probe to determine the gap structure. We have established this heat transport measurement technique via the study of BiS_2-based superconductor $NdO_{0.71}F_{0.29}BiS_2$ and heavy-fermion superconductor URu_2Si_2, which will be discussed in experimental section. Furthermore, in order to clarify whether there is sign change in the superconducting gap function, we perform the electron-irradiation experiments, which is known to be a phase sensitive probe. We apply these techniques to prototypical heavy-fermion superconductor $CeCu_2Si_2$ for the following reasons.

$CeCu_2Si_2$ is the first heavy-fermion superconductor discovered by Frank Steglich in 1979. The superconducting gap structure is believed to be *d*-wave with line nodes by several studies including NQR and neutron scattering. On the other hand, recent specific heat measurements reported fully-gapped superconductivity. However, since the specific heat mainly detects the quasiparticle with heavy mass, specific heat measurements do not exclude the possibilities of nodes on the light Fermi surface. In this manner, despite considerable experimental and theoretical efforts for almost 40 years, the superconducting gap structure of $CeCu_2Si_2$ has been still unclear.

The purpose of this study is to clarify the true superconducting gap structure of $CeCu_2Si_2$ using the two techniques described above: thermal conductivity and electron-irradiation experiments. Indeed, the thermal conductivity can sensitively detect the low-energy quasiparticle excitations from light bands. The study of superconducting gap structure of $CeCu_2Si_2$ will be discussed in section 5.

3 Experimental

3.1 Thermal conductivity and resistivity measurements at extremely low temperatures

Since $CeCu_2Si_2$ is known to be a multi gap superconductor with a T_c of about 600 mK, we have to cool it as much as possible to reveal the superconducting gap structure. We used a ^{3}He-^{4}He dilution refrigerator (Cryoconcept, DR-JT-S-200-10) which has a cooling power of 200 μW for the thermal conductivity and resistivity measurements in $CeCu_2Si_2$. By using the dilution refrigerator, we could measure the thermal conductivity and resistivity down to 40 mK, which corresponds to $T_c/15$.

The thermal conductivity is measured by the standard four-wire steady state method using one heater and two thermometers, with an applied temperature gradient less than 2 % of the sample temperature. The resistivity is also measured on the same setup continuously. The details of the experimental setups and the procedure of the thermal conductivity measurement will be explained in the next section. One of the most important things is how to make the contacts. If the contact resistance is large, the sample response may be masked at low temperature [32]. In order to decrease the contact resistance, we attached the silver wire to the sample by indium solder with the ultrasonic soldering iron (KURODA TECHNO CO., Ltd. Sunbonder USM-5). We found that the contact resistance was a few mΩ. In fact, we examined the effect of the superconductivity of indium by applying small magnetic field and found no discernible difference. In order to apply a magnetic field, we used a system with a 12-14 T solenoidal superconducting magnet (Oxford Instruments).

Figure 3.1: Picture of the measurement system with a gas handling system and superconducting magnet. The 12-14 T solenoidal superconducting magnet is placed under the floor. We operated the system by using a touch panel. In order to reduce vibration noise from the vacuum pumps, which may cause heating, we set up an anti-vibration block with several sandbags between the cryostat and the gas handling system.

3.1.1 Experimental setups for thermal conductivity measurements

The measurement cell for thermal conductivity is shown in Figure 3.2 and 3.3. The thermal conductivity was measured by the standard four-wire steady state method using one heater made of 1 kΩ chip resistor and two RuO_2 thermometers. The thermometers were carefully calibrated down to 30 mK in magnetic fields up to 12 T by using another RuO_2 thermometer calibrated in zero field. We placed the calibrated RuO_2 thermometer in a cancellation coil where the magnetic field disappear.

The resistive heater and thermometers are glued by GE varnish to polyimide tubes (DuPont, Kapton® tube) which are fixed to a frame made of fiber reinforced plastics (FRP). In order to thermally isolate each chip from the Cu heat bath, current leads connected to them are made of Manganin® (an alloy of typically 86 % copper, 12 % manganese, and 2% nickel) with a low thermal conductivity. Ag wires for reading the sample temperature (T_h and T_ℓ) and applying the heat current $\boldsymbol{Q}$ into the sample are glued to the electrical insulating surface of each chip. Moreover, Manganin wires are electrically connected to the each Ag wire and heat bath. Indeed, the Ag wire of heater, two thermometers, and heat bath can be used as the I_+, V_+, V_-, and I_-, respectively. Therefore, both the thermal and electrical transport coefficients can be measured alternatively during the same cooling run. The Ag wires from the sample are glued to the heat bath and each Ag wire of the chips by Ag paste (Ferro Electronic Material, L-200).

3.1.2 Experimental procedure

Resistivity

The resistivity was measured by the standard four-wire method. We used an AC resistance bridge LS370 (Lake Shore Cryotronics, Inc.) to measure the sample resistivity and an AVS-47B (RV-Elektroniikka Oy) to read the RuO_2 thermometers. The base temperature was monitored by an AVS-47 and controlled by the LS370.

Thermal conductivity

In a steady state, the thermal conductivity κ is defined as

$$\boldsymbol{q} = -\overline{\kappa}\nabla T, \tag{3.1}$$

where $\overline{\kappa}$ is the thermal conductivity tensor, $\boldsymbol{q}$ is the thermal current density, and ∇T is the thermal gradient. In a one-dimensional system as shown in Figure 3.3 with dimensions l, w, and t, Eq. (3.1) is expressed as

$$q = -\kappa\nabla_x T, \tag{3.2}$$

where $q = Q/S = Q/wt$ is a heat flux per unit time per unit area and $\nabla_x T = dT/dx = \Delta T/\ell$ is the temperature gradient along the length of the sample. We can make an effective temperature difference ΔT by applying the current I to a resistive heater:

$$\Delta T = [T_h(I) - T_\ell(I)] - [T_h(I = 0) - T_\ell(I = 0)], \tag{3.3}$$

where T_h and T_ℓ are the temperatures at the contacts on the side of the resistive heater and the Cu heat bath, respectively. We usually applied three different values of current (I_1, I_2, I_3) at each base temperature to confirm a linearity between Q and ΔT. Since we also measure the voltage V of the resistive heater simultaneously, we can calculate heat energy per unit time $Q = IV$. Hence, we obtain the thermal conductivity as

$$\kappa = \frac{\ell}{wt}\frac{IV}{\Delta T}. \tag{3.4}$$

The base temperature was monitored by the AVS-47 and controlled by the LS370. We use the AC resistance bridge AVS-47B to measure the resistance of the RuO_2 thermometers. We apply I to the resistive heater using Keithley 2400 SourceMeter® and measure the heater V using a Keithley 2000 multimeter.

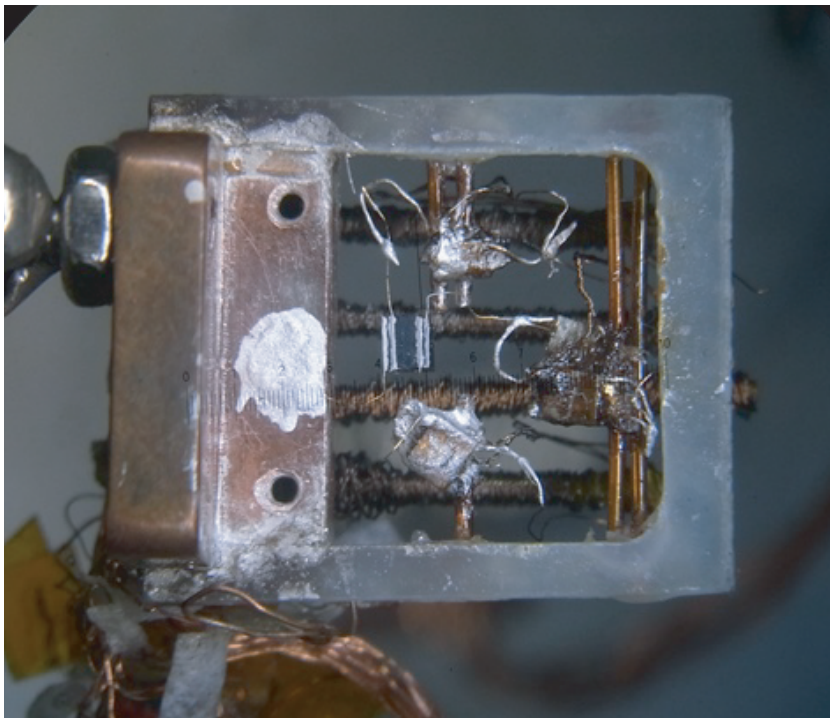

Figure 3.2: Picture of a cell for thermal conductivity and resistivity measurements with a sample.

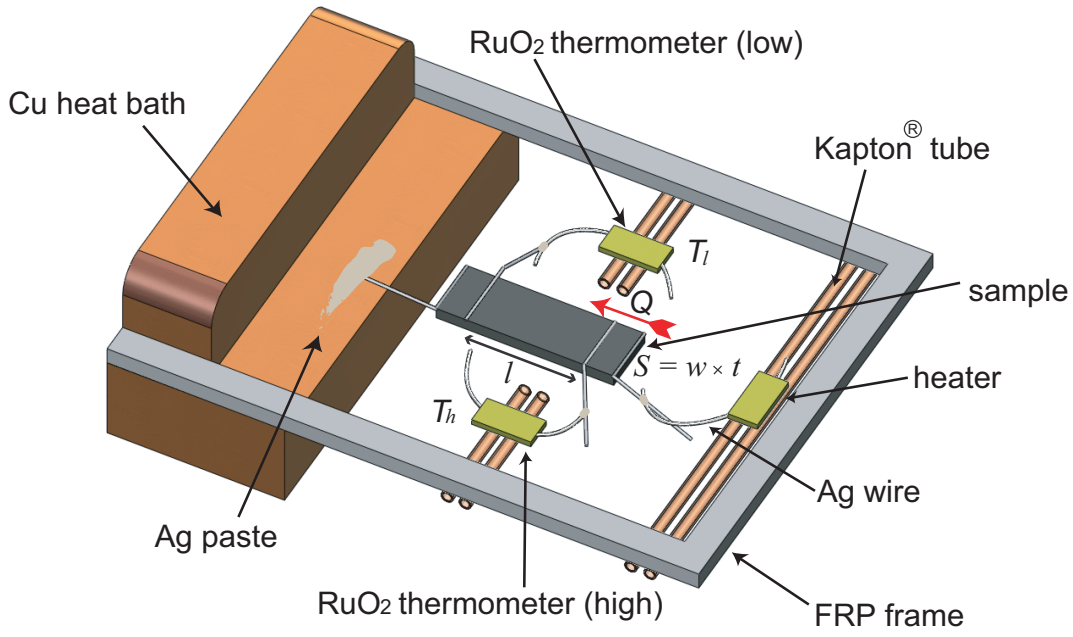

Figure 3.3: Schematic figure of a cell for thermal conductivity and resistivity measurements with a sample.

Operating system

Figure 3.4 shows the experimental setup for the thermal transport and resistivity measurement system. Each instrument of the system is operated by a personal computer through General Purpose Interface Bus (GPIB) interfaces. The measurements were operated by the LabVIEW^{TM} software (National Instruments Inc.).

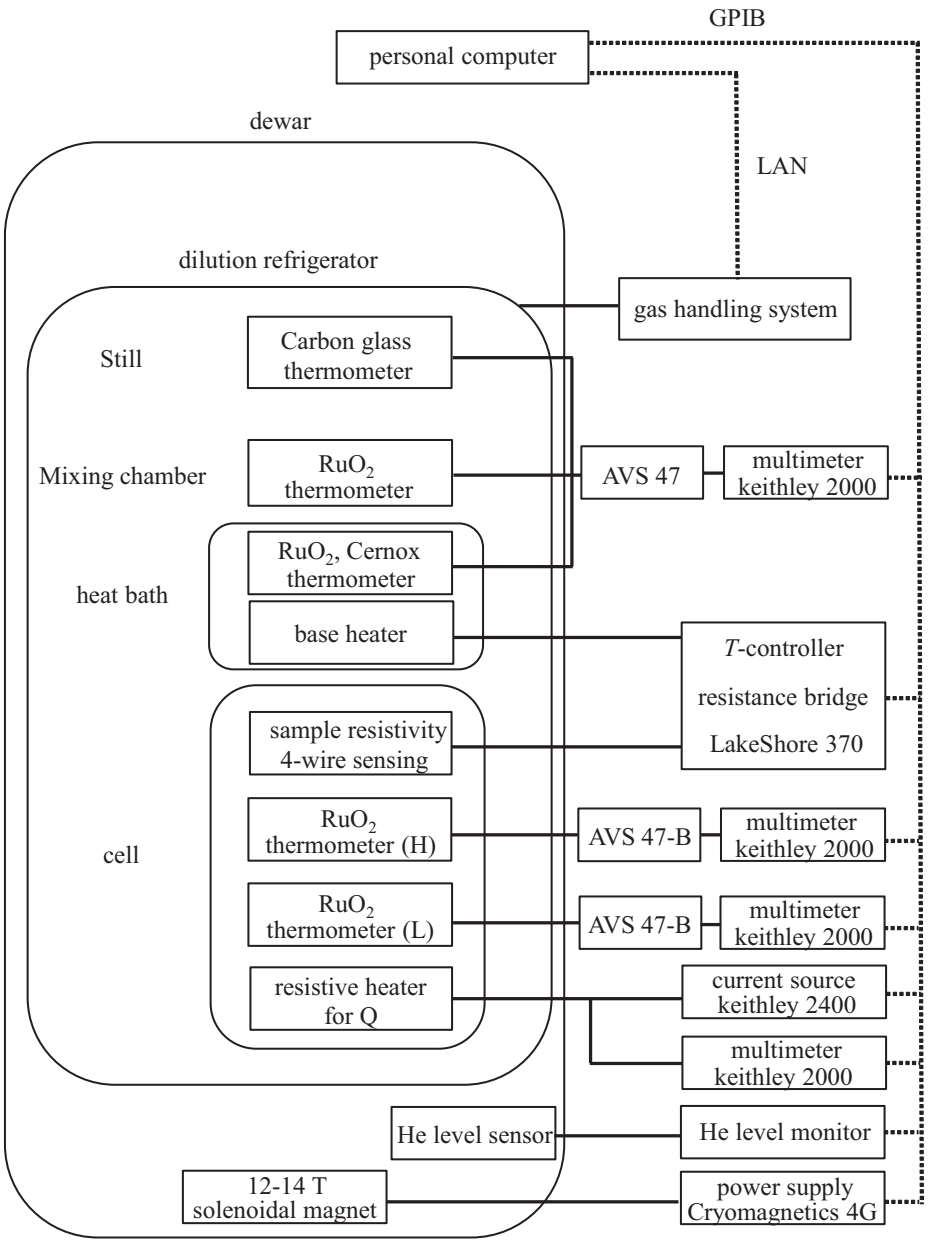

Figure 3.4: Schematic figure of measurement system.

3.2 Heat transport measurement as a powerful probe to investigate superconducting property

As discussed above, heat transport measurement is known to be a powerful probe to investigate the superconducting property. In this section, we discuss the utility of heat transport measurement with our results.

3.2.1 Conventional s-wave superconductivity in BiS_2-based $NdO_{0.71}F_{0.29}BiS_2$ revealed by thermal transport measurements

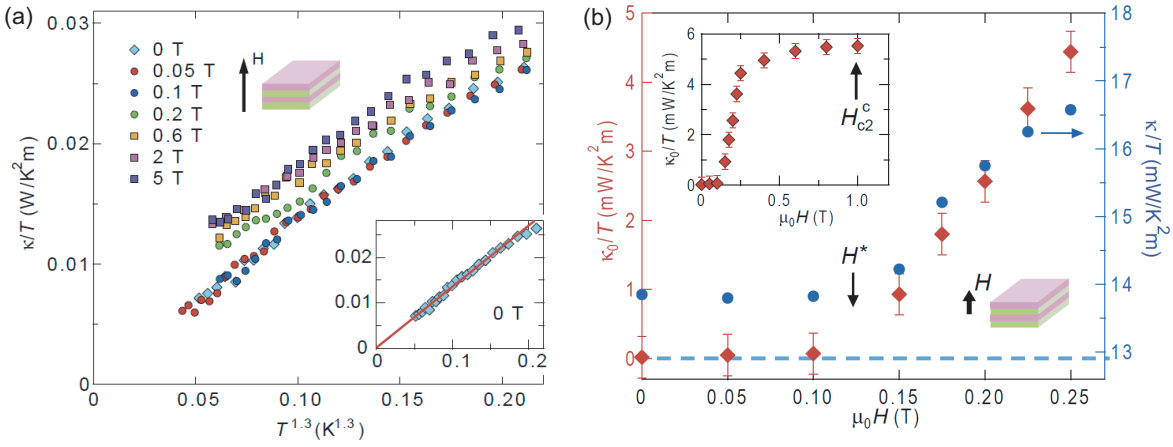

Figure 3.5: (a) Thermal conductivity divided by temperature κ/T of $NdO_{0.71}F_{0.29}BiS_2$ plotted against $T^{1.3}$ in several magnetic fields applied parallel to the c-axis. Inset: κ/T vs $T^{1.3}$ in zero field. The solid line represents a linear fit to the data below 0.3 K [33]. (b) Field dependence of the residual linear term κ_0/T (red diamonds) and κ/T at $T =$ 170 mK (blue circles) for $\boldsymbol{H} \| c$. The residual term $\kappa_0(H)/T$ is determined by fitting $\kappa(T)/T$ at different fields below 0.3 K with $\kappa_0/T + aT^{1.3}$, where κ_0/T and a are fitting parameters. Both κ_0/T and κ/T at $T = 170$ mK are independent of the magnetic field up to H^*. Inset shows κ_0/T in an extended field range. The superconducting upper critical field along c-axis H_{c2}^c is determined by the field dependence of the electrical resistivity at 0.2 K [33].

Recently, we have proved the superconducting gap structure of BiS_2-based superconductors via thermal conductivity measurements [33]. BiS_2-based superconductors are a new family of layered superconductors discovered by Y. Mizuguchi *et al.* [34,35]. Be-

cause of some common features with Fe-based high temperature superconductors, such as layered structures, BiS_2-based superconductors have aroused great interest. Indeed, several superconducting gap structures, including conventional s-, sign reversing s-, spin triplet p-, and d-wave symmetries have been proposed for BiS_2-based superconductors theoretically [36–42].

In order to determine the superconducting gap structure, we performed thermal conductivity measurements ($q \parallel a$, $H \parallel c$) on BiS_2-based $NdO_{0.71}F_{0.29}BiS_2$ single crystal (T_c = 5 K, $H_{c2}^c(0)$ = 1 T) down to 100 mK. As a result, the residual linear term in the thermal conductivity κ_0/T at $T \to 0$ is vanishingly small, indicating that the residual normal fluid, which is expected for nodal superconductors, is absent in zero field (Inset of Figure 3.5 (a)). Moreover, the applied magnetic field hardly affects the thermal conductivity in a wide range of the vortex state $H < H^*$, indicating the absence of Doppler shifted quasiparticles (Figure 3.5 (b)). It should be noted that since $NdO_{0.71}F_{0.29}BiS_2$ is a single-band system, the increase of κ_0/T above $H^* \approx 0.12\ H_{c2}^c(0)$ indicates a large anisotropic superconducting gap structure.

These results provide evidence that $NdO_{0.71}F_{0.29}BiS_2$ is a fully gapped superconductor. We also estimated the coherence length ξ_{ab} and mean free path ℓ to investigate whether the gap changes its sign. The lengths are estimated to be $\xi_{ab} = \sqrt{\Phi_0/(2\pi\mu_0 H_{c2}^c)} = 18\,\mathrm{nm}$ and $\ell = (\mu_0\lambda(0)^2 v_\mathrm{F})/\rho_0 \sim 30 - 50\,\mathrm{nm}$, where Φ_0 is the flux quantum, $\lambda(0) \approx 447$ nm is the zero temperature in-plane penetration length [43], v_F is the Fermi velocity, reported to be $v_F = 0.95 \times 10^6$ m/s by angle resolved photo emission spectroscopy [44], and $\rho_0 = 500{\sim}800\ \mu\Omega$cm for this study and previous reports [45,46]. Therefore, the in-plane mean free path ℓ is comparable to the in-plane coherence length ξ_{ab}. The robustness of the superconductivity in $NdO_{0.71}F_{0.29}BiS_2$ appears to be at odds with the unconventional pairing symmetries. These considerations lead us to conclude that $NdO_{0.71}F_{0.29}BiS_2$ is likely to be a conventional s-wave superconductor.

3.2.2 Colossal thermomagnetic response in the exotic superconductor URu_2Si_2

The heavy-fermion superconductor URu_2Si_2 (T_c = 1.45 K) has been suggested to be a candidate for a chiral d-wave superconductor that spontaneously breaks time-reversal symmetry (TRS) $\mathcal{T}$ in the superconducting state [48–51]. Indeed, the angular dependence of the thermal conductivity and specific heat in magnetic fields indicates the presence of point nodes in the order parameter, and a chiral d-wave pairing symmetry in a complex form of $k_z(k_x \pm ik_y)$ has been proposed [48, 49]. Very recently, the broken TRS has also been reported as a result of polar Kerr effect measurements [52]. On the basis of these results, possible Weyl-type topological superconducting states have been discussed [53]. It is therefore highly intriguing to examine the superconducting fluctuations in URu_2Si_2.

In order to examine the superconducting fluctuations above T_c, we have measured the transverse thermoelectric (Nernst) effect of ultraclean URu_2Si_2 single crystals (T_c = 1.45 K) [47]. The Nernst effect measurement is known to be a particularly sensitive probe for the superconducting fluctuations [54, 55].

The Nernst signal N is the electric field E_y ($||$ y) response to a transverse temperature gradient $\nabla_x T$ ($||$ x) in the presence of a magnetic field H ($||$ z), and is given by $N \equiv E_y/(-\nabla_x T)$. The schematic figure of the measurement setup is depicted in Figure 3.6 (a). The Nernst coefficient, defined as $\nu \equiv N/\mu_0 H$ above T_c, consists of two contributions generated by different mechanisms: $\nu = \nu^S + \nu^N$. The first term, ν^S, represents the contribution of superconducting fluctuations of either the amplitude or phase of the order parameter, which is always positive [56]. The second term, ν^N, represents the contribution from the normal quasiparticles, which can be either positive or negative [57]. Within the Boltzmann theory, when scattering time τ is weakly dependent on energy, ν^N can be expressed as $\nu^N = (\pi^2/3)({k_B}^2 T/m^*)(\tau/\varepsilon_F)$, where k_B is the Boltzmann constant, m^* is the effective mass and ε_F is the Fermi energy [58].

We observed fluctuation-induced steep enhancement of ν below T^* and a divergent increase on approaching T_c (Figure 3.6 (a-b)). Importantly, contrary to the conventional Gaussian fluctuation theories [56,59–61] which predict $\nu^S \propto 1/\tau$, ν^S is greatly enhanced

with τ below T^* (Figure 3.6 (a-c)). Here, ν^S can be obtained by subtracting the T-linear ν^N from ν (Figure 3.6 (b)). It is intriguing to compare the present results with $CeCoIn_5$, which shares several common features with URu_2Si_2, such as heavy-fermion unconventional superconductivity with a nodal gap and similar T_c and upper critical fields. It should be stressed that in very pure $CeCoIn_5$, with $\rho(T_c^+) \approx 4\ \mu\Omega$cm, which is of the same order as that of our URu_2Si_2 crystals, no discernible ν^S is observed [62,63]; ν^S is at least two orders of magnitude smaller in pure $CeCoIn_5$ than in URu_2Si_2. These results thus highlight an essential difference in the superconducting fluctuations between URu_2Si_2 and the other unconventional superconductors. Indeed, the most essential difference between URu_2Si_2 and $CeCoIn_5$ is that TRS is broken in the former whereas it is not broken in the latter [64].

Moreover, the fluctuation-induced off-diagonal component of the thermoelectric tensor (Peltier coefficient) α_{xy}^S divided by the magnetic field is anomalously enhanced (by a factor of $\sim 10^6$) as compared with the theoretically expected value of the conventional Gaussian superconducting fluctuations (Figure 3.6 (d)).

These results invoke possible chiral or Berry-phase fluctuations [65] associated with the broken time-reversal symmetry of the superconducting order parameter.

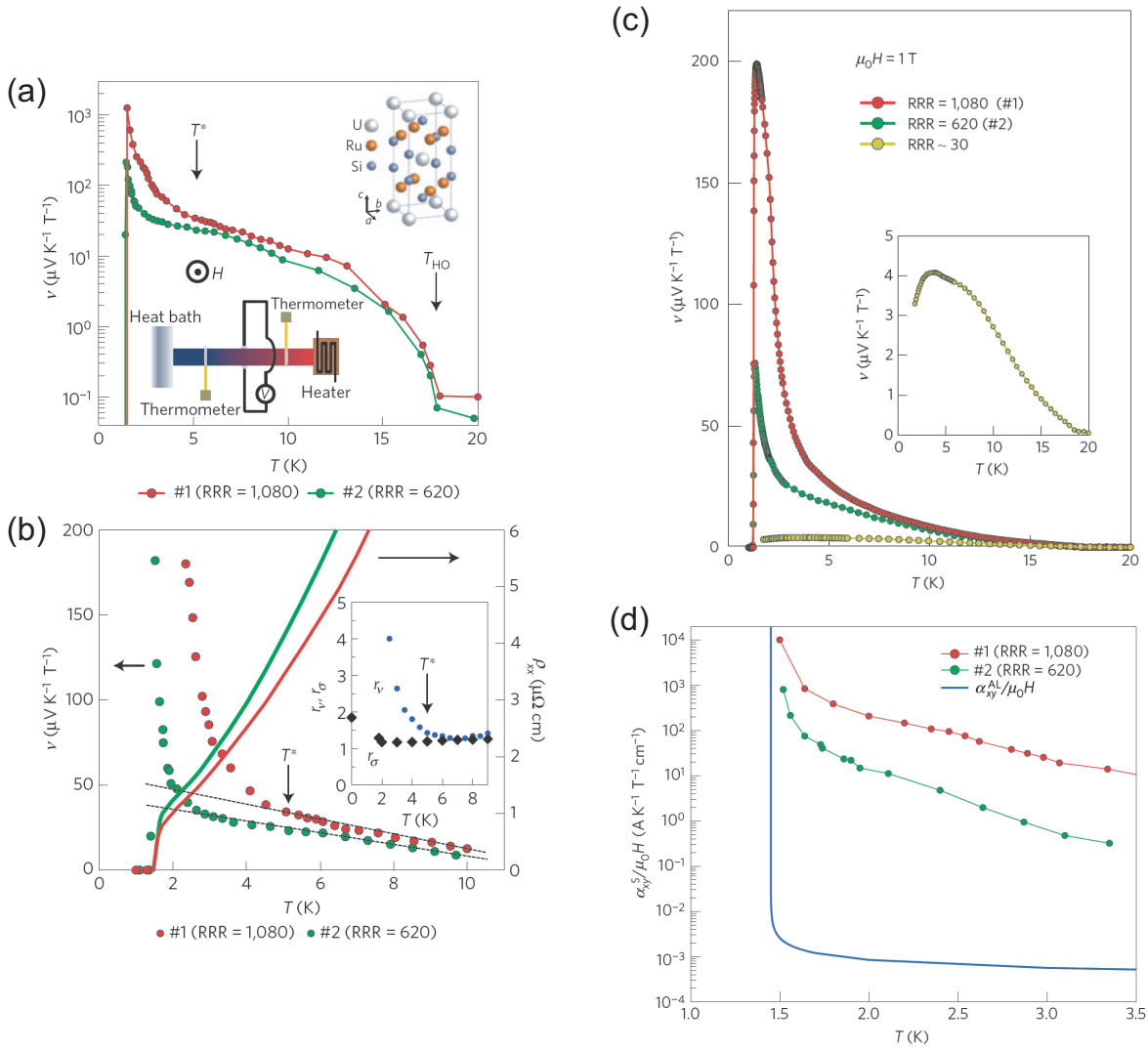

Figure 3.6: (a) T-dependence of the Nernst coefficient $\nu(T) = N/\mu_0 H$ in the zero-field limit ($\mathbf{H} \parallel c$) for single crystals #1 (RRR = 1,080) and #2 (RRR = 620). The RRR values are determined from $\rho(300\text{K})/\rho_0$ by assuming the T-dependence of the in-plane resistivity ρ_{xx} as $\rho_{xx} = \rho_0 + AT^n$, with $n = 1.5$ and 1.7 for #1 and #2, respectively, below 6 K. In both crystals, T_c defined by the point of zero resistivity is 1.45 K. The upper inset illustrates the crystal structure of URu_2Si_2 and the lower inset is a schematic of the measurement set-up. (b) Low-temperature data of $\nu(T)$ and $\rho_{xx}(T)$ for crystals #1 and #2. Below T^*, rises sharply above the T-linear dependence extrapolated from higher temperatures (dashed lines). The inset shows the T-dependence of the ratios of the Nernst coefficient and conductivity of the two crystals, $r_\nu = \nu(\#1)/\nu(\#2)$ and $r_\sigma = \rho_{xx}(\#2)/\rho_{xx}(\#1)$. (c) Comparison of the $\nu(T)$ data at $\mu_0 H = 1$ T between samples with different scattering rates (RRR = 1,080, 620 and 30). The data for RRR $\sim$ 30 (expanded in the inset) is taken from [66]. (d) T-dependence of the fluctuation-induced Peltier coefficient divided by the magnetic field, $\alpha_{xy}^S/\mu_0 H$ for crystals #1 and #2. The blue line represents the Peltier coefficient that results from Gaussian-type (Aslamazov-Larkin) fluctuations.

3.3 Point defects introduced by electron irradiation

As mentioned in section 1.7, the impurity effect can be used as a probe of a sign-changing gap. In particular, the effect of disorder has been studied intensively in Fe-based superconductors because the multiband nature leads to a variety of candidates for the superconducting symmetry, including sign-preserving s_{++}, sign-changing $s_{\pm}$ with and without nodes, d-wave, and so on [67–74].

There are several ways to introduce the disorder into the sample. One of the simplest ways is chemical substitutions. However, the foreign ions may change not only the scattering, but also other quantities, including the Fermi energy and band structure. Moreover, we cannot introduce the defects in the same sample.

An alternative way is irradiation with energetic particles. Depending on the particle type and energy, the induced defects have a characteristic structure (Figure 3.7). Heavy-ion irradiation creates complex columnar trucks [75]. α particle and proton irradiation create cascades of point defects [76]. In contrast, electron irradiation creates uniformly distributed point defects over the entire crystal. The pairs of interstitial ions and vacancies are called Frenkel pairs. Indeed, only electrons with energies of 1-10 MeV can produce the point defects which act as perfect scattering centers [76]. Such point defects play an important role to distinguish between s_{++} and $s_{\pm}$-wave symmetry. If the defects induce small momentum transfer Q scattering, intraband scattering becomes dominant. This leads to much weaker T_c vs. $\Delta\rho_0$ suppression rates, even in the sign-reversing $s_{\pm}$ [77]. Moreover, small Q scattering also masks the $s_{\pm}$ nature, for example, in the

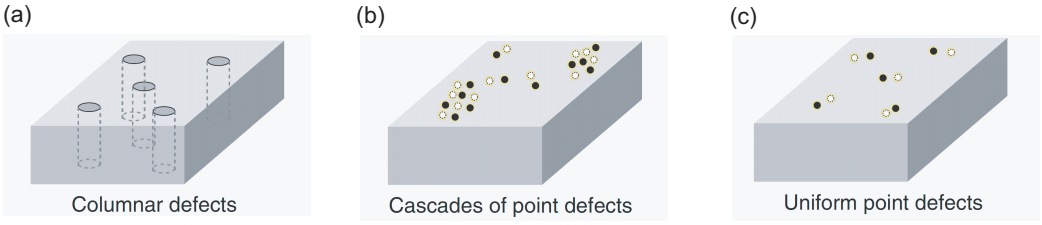

Figure 3.7: Schematic figure of (a) columnar defects induced by heavy-ion irradiation, (b) clusterlike cascades of point defects induced by α particle and proton irradiation, and (c) uniform point defects induced by electron irradiation. Adapted from [78].

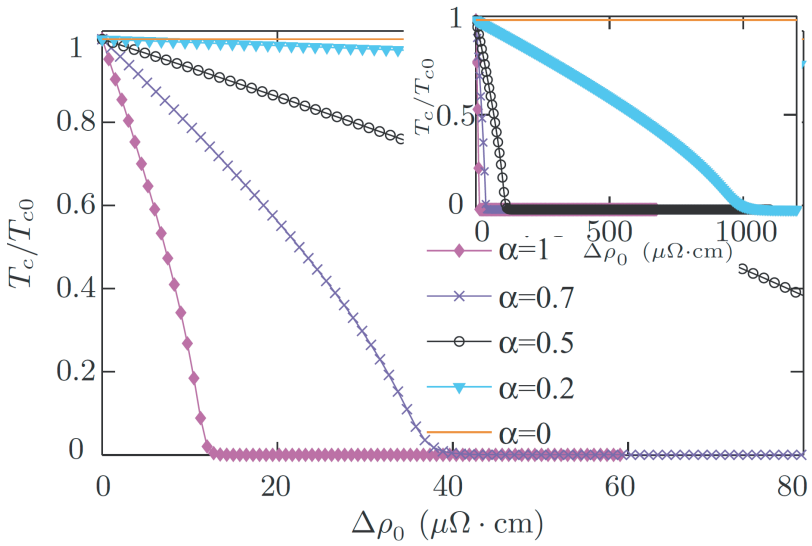

Figure 3.8: Normalized critical temperature T_c/T_{c0} vs. disorder-induced resistivity change $\Delta\rho_0$ for isotropic $s_{\pm}$-wave pairing for various values of the inter- to intraband scattering ratio α [77]. Inset: Same quantity plotted over a larger $\Delta\rho_0$ scale.

temperature dependence of penetration depth [79]. However, point defects created by electron irradiation induce large Q scattering, which contribute the interband scattering channel. Therefore, we can firmly distinguish between s_{++} and $s_{\pm}$-wave symmetry by electron irradiation [78]. Another advantage of electron irradiation is that, unlike the chemical substitutions, the disorders can be introduced in the same sample without changing carrier density and lattice constants.

We performed the electron irradiation experiments in the electron irradiation facility SIRIUS at the Laboratoire des Solid Irradiés in the École Polytechnique, France. We used electrons with incident energy of 2.5 MeV, for which the energy transfer from the impinging electron to the lattice is above the threshold energy for the formation of Frenkel pairs that act as point defects. In order to prevent point defect clustering, irradiation is performed at 25 K using an H_2 recondenser.

4 Heavy-fermion compound $CeCu_2Si_2$

$CeCu_2Si_2$ is a prototypical heavy-fermion superconductor with a T_c of 0.6 K, discovered by F. Steglich in 1979 [3]. The large specific heat jump at T_c indicates that the heavy electrons form Cooper pairs. Moreover, the unusual physical properties cannot be explained by the conventional BCS theory. Therefore, $CeCu_2Si_2$ opened the new era of unconventional superconductivity. In this section, heavy-fermion physics and quantum criticality will be discussed in brief. Then, we will discuss the physical properties of $CeCu_2Si_2$.

4.1 Introduction of heavy-fermion

Some kind of intermetallic compounds, containing the elements with $4f$ or $5f$ electrons, have attracted much attention. They show several ground states, which is determined by the competition between the Kondo interaction and Ruderman-Kittel-Kasuya-Yosida (RKKY) exchange interaction. The f-electron compounds are commonly described by Kondo-lattice systems. The Kondo-lattice Hamiltonian is given by

$$\mathscr{H}_{KL} = \sum_{ij} t_{ij} c^{\dagger}_{i\sigma} c_{j\sigma} + J \sum_{i} \boldsymbol{S}_i \cdot \boldsymbol{s}_i, \tag{4.1}$$

where t_{ij} is the hopping matrix element, $c^{\dagger}_{i\sigma}$ ($c_{i\sigma}$) is the creation (annihilation) operator of the conduction-electrons, $\boldsymbol{S}_i$ is the local spin, $\boldsymbol{s}_i$ is the conduction-electron spin, J is the antiferromagnetic Kondo coupling constant. The second term describes the Kondo interaction between localized f-electrons and conduction c-electrons. For the temperature well above the characteristic Kondo temperature T_K, the system is paramagnetic states described by a Curie-Weiss law. On the other hand, for the temperature below T_K, they start to form a Kondo singlet and the f-electron is screened by the conduction

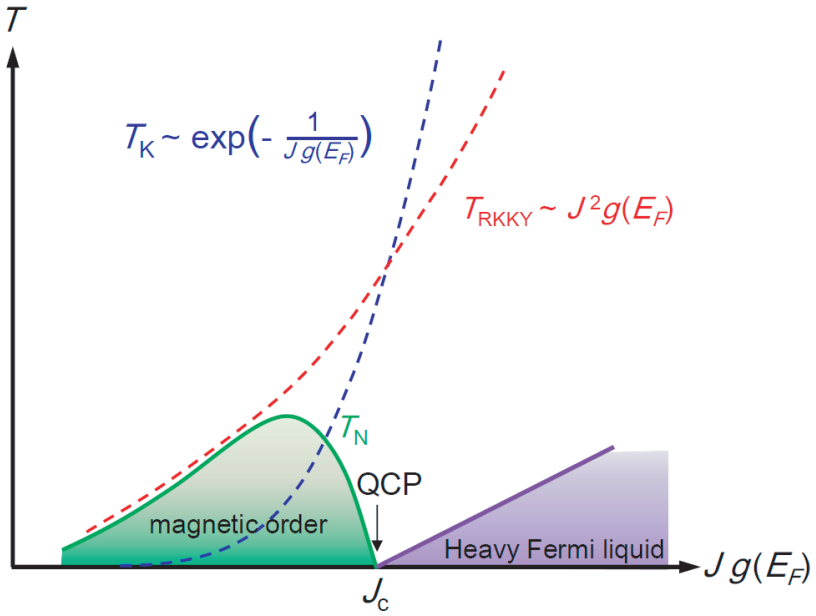

Figure 4.1: Schematic figure of the Doniach phase diagram. In the weak coupling regime ($J < J_c$) where $T_{\mathrm{RKKY}} > T_K$, a magnetic ordered ground state appears below T_N. In the strong coupling regime ($J > J_c$) where $T_K > T_{\mathrm{RKKY}}$, on the other hand, the ground state is a paramagnetic heavy Fermi liquid.

electron sea. The Kondo temperature is given by

$$k_B T_K \sim \frac{1}{g(E_F)} \exp\left(-\frac{1}{Jg(E_F)}\right) \tag{4.2}$$

where $g(E_F)$ is the density of states at the Fermi energy. For $T \ll T_K$, since the Kondo singlets form a periodic Kondo lattice, Bloch's theorem causes the Kondo singlets to couple coherently. Therefore, the narrow quasiparticle band is formed near the Fermi energy through c-f hybridization. As a result, the quasiparticle effective mass m^* is strongly enhanced, and is one or two orders of magnitude larger than the bare electron mass.

The RKKY exchange interaction is a conduction-electron-mediated indirect interaction between the f-local moments which promotes long-range magnetic ordering. The

RKKY Hamiltonian is given by

$$\mathscr{H}_{\mathrm{RKKY}} = \sum_{ij} J_{ij} \boldsymbol{S}_i \cdot \boldsymbol{S}_j \tag{4.3}$$

$$J_{ij} \propto J^2 g(E_F) \frac{\cos(2k_F r_{ij})}{r_{ij}^3}, \tag{4.4}$$

where J_{ij} is the RKKY coupling constant. The characteristic temperature is given by

$$k_B T_{\mathrm{RKKY}} \sim J^2 g(E_F), \tag{4.5}$$

Contrary to the case of the Kondo effect which leads to the non-magnetic ground state, the RKKY exchange interaction stabilizes the magnetic ordered ground state. The competition between the Kondo and RKKY exchange interaction is visualized in the so-called Doniach phase diagram, in which the Kondo coupling constant J dependence of the characteristic temperature T_K and T_{RKKY} are shown. In the weak coupling regime ($J < J_c$) where $T_{\mathrm{RKKY}} > T_K$, the magnetic ordered ground state appears below T_N. In the strong coupling regime ($J > J_c$) where $T_K > T_{\mathrm{RKKY}}$, on the other hand, the ground state is paramagnetic heavy Fermi liquid. In the heavy-fermion material, such as some sorts of Ce compounds and Yb compounds, T_K is enhanced due to the orbital degeneracy:

$$k_B T_K \sim \frac{1}{g(E_F)} \exp\left(-\frac{1}{(2\ell+1) J g(E_F)}\right), \tag{4.6}$$

and can exceed T_{RKKY} [81].

At $J = J_c$, as mentioned in section 1.3, the quantum critical point appears.

4.2 Crystal structure and phase diagram

As with many other 122 compounds, $CeCu_2Si_2$ crystallizes in a body-centered tetragonal $ThCr_2Si_2$ crystal structure (Figure 4.2 (a)). As shown in Figure 4.2 (b), $CeCu_2Si_2$ has a wide variety of ground states, which is determined by the competition between the Kondo and RKKY interaction. Indeed, the ground state depends very delicately on the actual stoichiometry [83, 84].

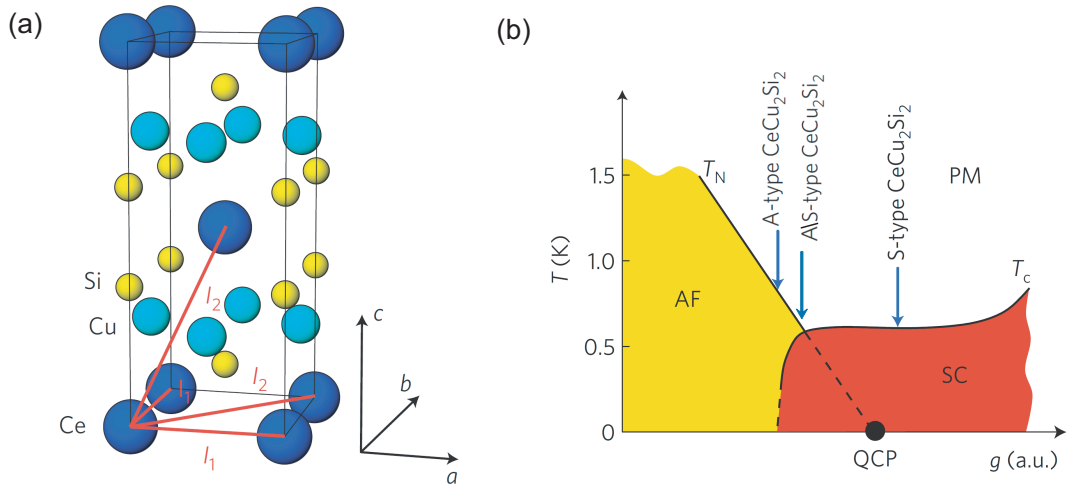

Figure 4.2: (a)Tetragonal crystal structure (space group: I4/mmm) of $CeCu_2Si_2$. (b)Schematic T-g phase diagram of $CeCu_2Si_2$ (g is a coupling constant). Superconductivity emerges around the antiferromagnetic (AF) quantum critical point (QCP). The positions of the A-type, A/S-type, and the S-type $CeCu_2Si_2$ in the phase diagram are marked by blue arrows [82].

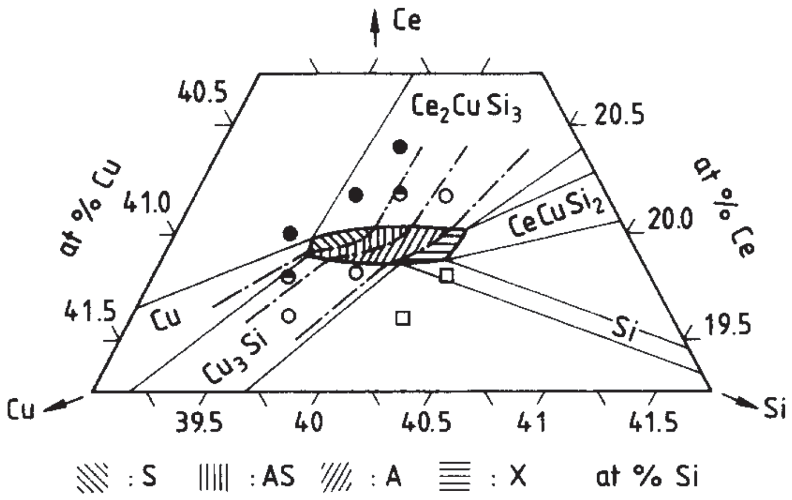

Figure 4.3: The ternary phase diagram for various Ce : Cu: Si compositions (dashed: $CeCu_2Si_2$ homogeneity range) [84]. "A" (○), "S" (●), and "A/S" (circle with upper half black) represent the antiferromagnetic order phase, superconducting phase, and competition phase between them, respectively.

A tiny Cu-deficient sample exhibits only an antiferromagnetic order phase (so-called A-type). On the other hand, a tiny Cu-rich sample exhibits only a superconducting phase (so-called S-type). In fact, the 1:2:2 stoichiometric sample exhibits both antiferromagnetic order and a superconducting phase (so-called A/S-type). The detailed explanation for each phase in $CeCu_2Si_2$ will be discussed in a later section.

4.3 Fermi surface

The Fermi surface topology is important for understanding unconventional superconductivity. However, only a few experimental studies, such as de Haas-van Alphen measurements [85], have been carried out in $CeCu_2Si_2$. Indeed, the dHvA branches could not be detected completely due to very small signals by heavy masses, as was pointed out in theoretical calculations [86].

On the other hand, earlier theoretical calculations proposed two possible Fermi surface topologies. Figure 4.4 depicts the two Fermi surface topologies obtained from local density approximation (LDA) calculations [86] and the renormalization band method [87]. From both calculations, we can see that $CeCu_2Si_2$ has two separate Fermi surfaces (FS). One is the light-hole FS (Figure 4.4 (a) and (b)) and the other is the heavy-electron FS (Figure 4.4 (c) and (d)). Although the light-hole FSs are rather similar to each other, the heavy-electron FSs are quite different.

Very recently, other LDA and LDA + U calculations were carried out [88]. In the LDA case (Figure 4.5 (a)), a cubic-like electron sheet and a tiny electron sheet around Γ and a complex hole sheet are found. In the LDA + U case (Figure 4.5 (b)), on the other hand, a corrugated-cylindrical heavy-electron FS around X and complex light hole FSs are found. The FSs in the LDA + U is similar to those in the renormalization band method [87].

Importantly, the FS topology derived from LDA + U can explain the neutron scattering results [93]. Indeed, the magnetic RPA susceptibility is strongly enhanced at around $\boldsymbol{Q}$ = (0.21 0.21 0.5) (Figure 4.5 (d)) owing to the nesting property in the corrugated-cylindrical heavy-electron FS around X, which is, as will be discussed in

more detail in a later section, consistent with the experimentally observed incommensurate SDW propagation vector τ = (0.215 0.215 0.53) [93]. The heavy-electron FS derived by the renormalization band method can also explain the observed SDW order induced by FS instability. Conversely, the LDA calculations cannot explain the neutron scattering results. Therefore, LDA + U FSs is one of the most promising FSs in $CeCu_2Si_2$ at ambient pressure.

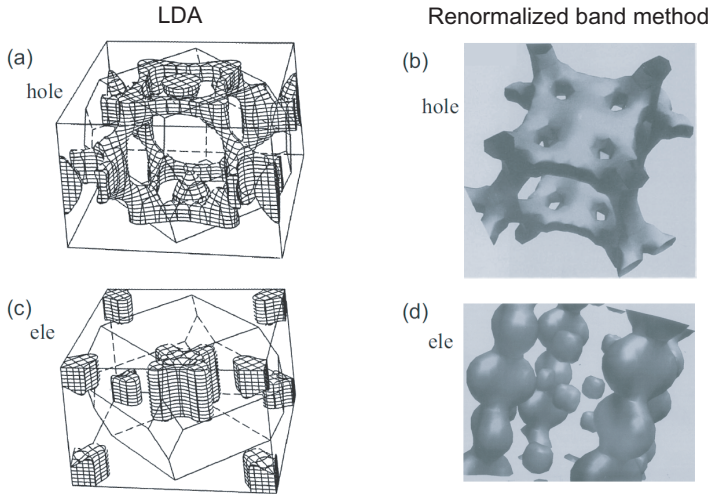

Figure 4.4: The Fermi surface of $CeCu_2Si_2$ calculated by (a), (c) LDA calculations [86] and (b), (d) the renormalized band method [87].

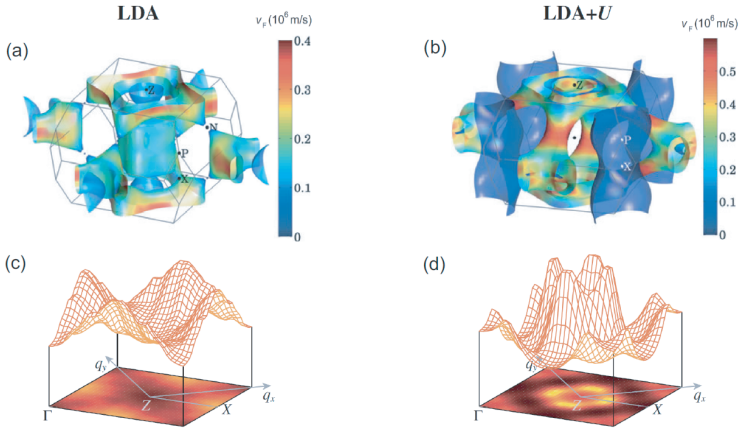

Figure 4.5: The Fermi surface of $CeCu_2Si_2$ calculated by (a) LDA and (b) LDA + U calculations. (c), (d) Magnetic RPA susceptibilities for $\boldsymbol{q} = (q_x\ q_y\ 0.5)$ [88].

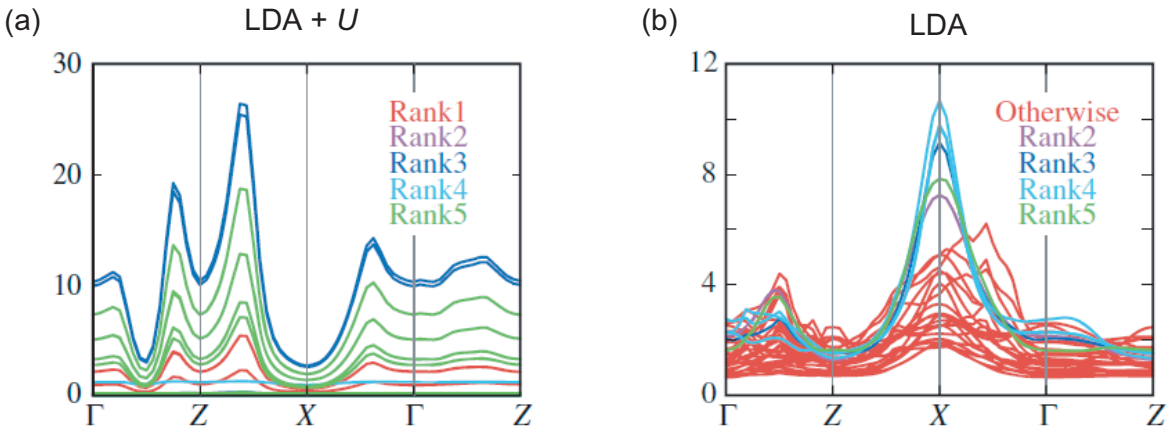

Figure 4.6: Multipole susceptibility along the high symmetry line [88]. (a) LDA + U case. (b) LDA case.

In ref. [88], multipole susceptibility is also calculated along the high-symmetry line. The multipole degrees of freedom is caused by entanglement between orbital and spin degrees of freedom due to the presence of strong spin-orbit coupling in the f-electron systems. Indeed, $J = 5/2$ multiplet with six j_z component leading to 36 multipole degrees of freedom, which are classified into rank 0, 1, ..., 5. In the LDA + U case, octupole fluctuations are dominantly enhanced, and next are dotriacontapole fluctuations (Figure 4.6 (a)). This is consistent with the fact that the ground-state orbital is $j_z = \pm 3/2$ mixed with a small weight of $j_z = \mp 5/2$. In the LDA case, on the other hand, non-magnetic orbital fluctuations are largely enhanced (Figure 4.6 (b)). As will be discussed in a later section, the second high-pressure superconducting dome is located far away from AF QCP and the superconductivity at high-P region is thought to be mediated by non-magnetic valence-fluctuations. If the non-magnetic orbital fluctuations are related to the valence-fluctuations, the LDA Fermi surface may be the candidate for the high-pressure region.

4.4 A-phase in $CeCu_2Si_2$

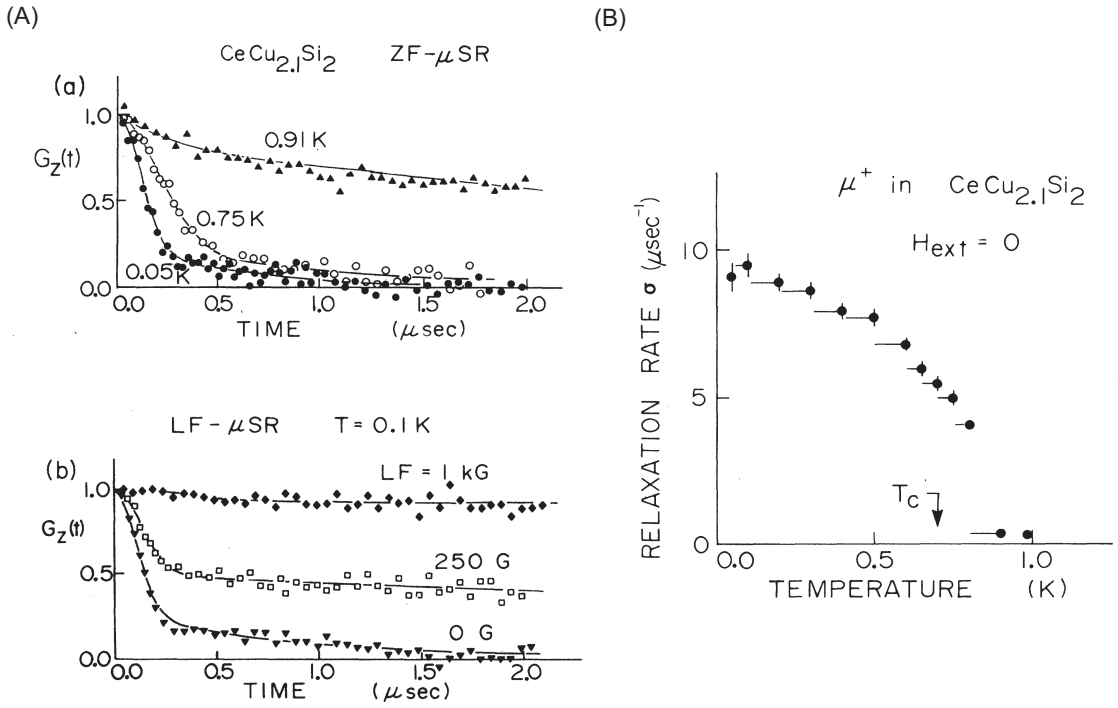

Figure 4.7: μSR measurements on a polycrystalline sample of $CeCu_{2.1}Si_2$. (A) Muon-spin-relaxation function $G_z(t)$ (a) in zero field and (b) at $T = 0.1$ K in longitudinal external fields. (B) Muon-spin-depolarization rate σ vs. T in zero field [91].

10 years after discovering its superconductivity, NMR [89] and muon spin rotation (μSR) [90, 91] revealed that an unusual magnetic order phase, the so-called A-phase, exists in $CeCu_2Si_2$. The rapid increase of the μSR relaxation rate below 0.8 K suggests the existence of a static internal local field or fluctuating dynamical local fields (Figure 4.7). The latter possibility is excluded because longitudinal external fields reduce the relaxation rate remarkably. Moreover, since the μSR relaxation function $G_z(t)$ shows no precession behavior which occurs in uniform ferro- or antiferromagnets, the magnitude of the local fields at muon sites seems to vary widely. These results indicate that the unusual magnetic order occurs below 0.8 K with a small ordered moment of 0.1 μ_B. μSR measurements on A-type single crystals also reported the same results [92].

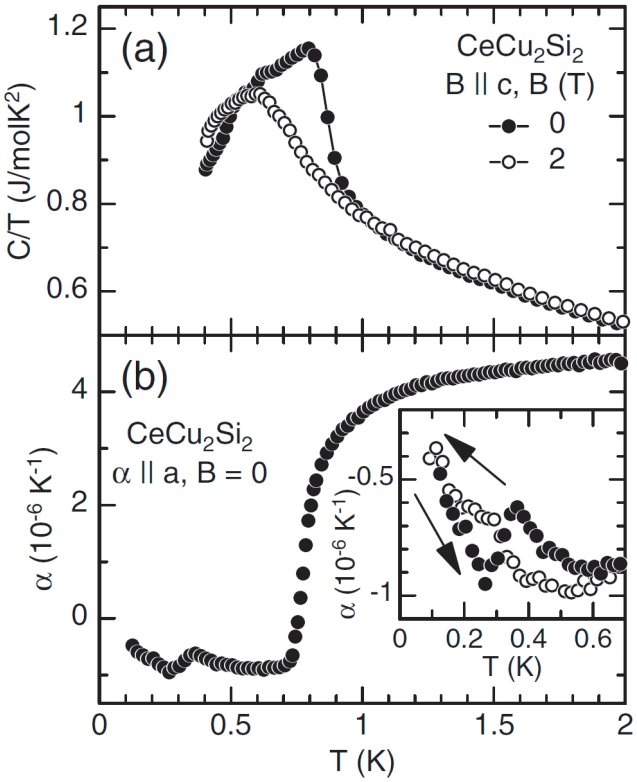

Figure 4.8: (a) Temperature dependence of the specific heat at $H = 0$ T and 2 T. A large jump occurs at $T_N = 0.86$ K. The magnetic field decreases the transition temperature. (b) The temperature dependence of the thermal expansion coefficient α along the a axis in zero field. A large jump anomaly is also observed in α at T_N. Inset: the hysteretic behavior associated with the lock-in transition at low temperatures [93].

The existence of the A-phase is also suggested by the measurements of the thermodynamic properties [93, 94]. Figure 4.8 (a) shows the temperature dependence of the specific heat. In zero field, the specific heat shows a large jump at $T_N = 0.86$ K. At $H = 2$ T, where the superconductivity is completely suppressed, the anomaly still appears even though the magnetic field reduces the onset temperature. Figure 4.8 (b) shows the temperature dependence of the thermal expansion coefficient α along the a axis in zero field. The thermal expansion coefficient also shows the large jump at T_N. These jumps in the thermodynamic quantities at T_N are indicative of a second order transition into the A-phase.

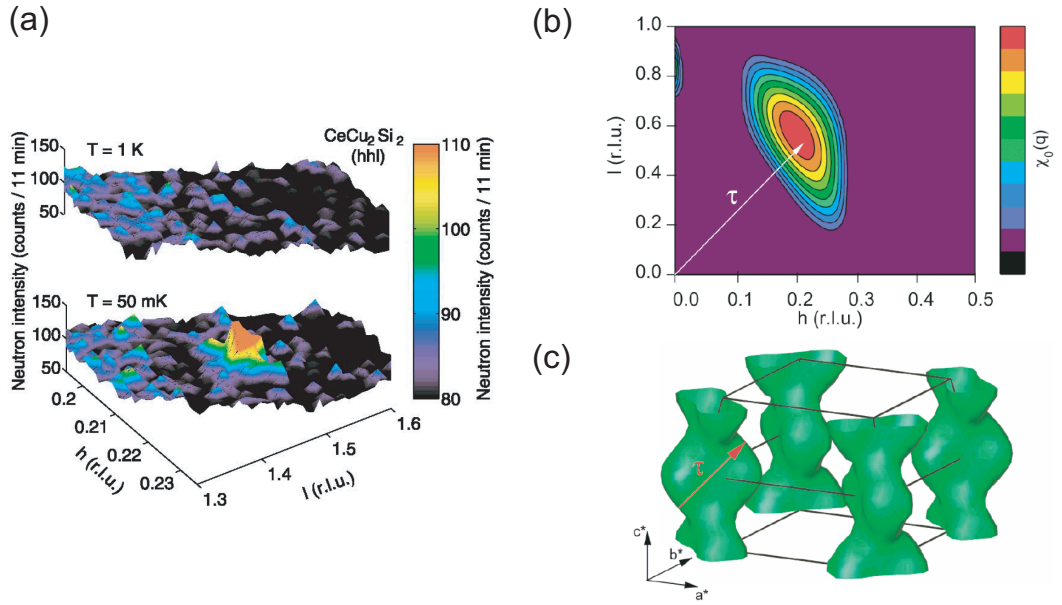

Figure 4.9: (a) Neutron scattering intensity map around $q = (0.21\ 0.21\ 1.45)$ at $T = 50$ mK and 1 K. Below T_N of 0.86 K, the magnetic peak appears at q which corresponds to the incommensurate SDW propagation vector $\tau = (0.215\ 0.215\ 0.53)$. (b) Theoretical intensity map for magnetic susceptibility $\chi_0(q)$. $\chi_0(q)$ shows a pronounced maximum at τ. (c) Heavy Fermi surface calculated by renormalized band method. The nesting vector coincides with the SDW propagation vector τ [93].

In order to reveal the nature of the A-phase, neutron diffraction experiments were performed on an A-type $CeCu_2Si_2$ single crystal [93]. The magnetic superstructure peaks only appear below T_N at $q = (0.21\ 0.21\ 1.45)$, which is a satellite of the (0 0 2) nuclear peak (Figure 4.9 (a)). Therefore, the nature of the A-phase is characterized by the incommensurate spin-density wave (SDW) order with a propagation vector of $\tau = (0.215\ 0.215\ 0.53)$. It is noted that τ decreases with lowering temperature and then become T-independent below 0.3 K. This lock-in transition is observed as a first order transition in the thermal expansion measurements (inset of Figure 4.8 (b)).

The calculated magnetic susceptibility $\chi_0(q)$ shows a pronounced maximum at τ. Moreover, τ coincides with the nesting vector connecting the flat parts of the corrugated-cylinder heavy Fermi surface calculated by the renormalized band method (Figure 4.9 (c)). Hence, the incommensurate SDW order in the A-phase is the result of the Fermi surface instability.

4.5 A/S-phase in $CeCu_2Si_2$

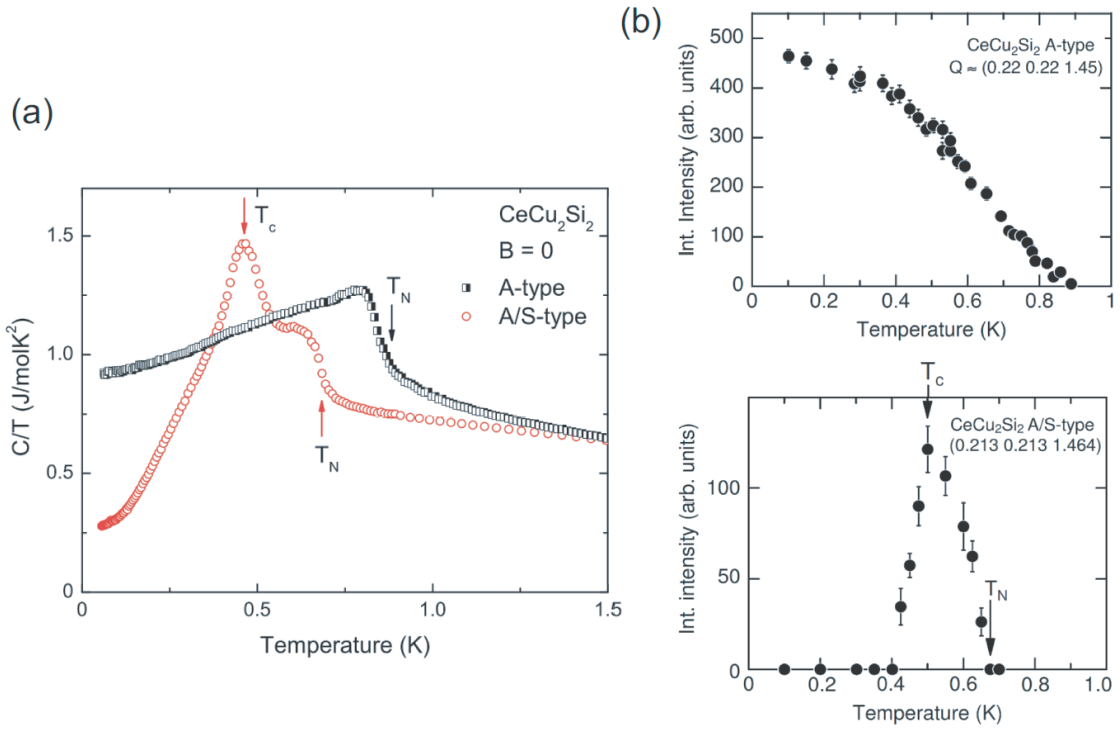

Figure 4.10: (a) Specific heat data of A-type and A/S-type $CeCu_2Si_2$ single crystals in zero field. A/S-type shows a transition into the incommensurate SDW order phase at $T_N \sim 0.7$ K and the superconducting phase at $T_c \sim 0.5$ K [95]. (b) (upper panel) The integrated neutron intensity of the magnetic Bragg peak at $q = (0.22\ 0.22\ 1.45)$ in the A-type. (bottom panel) Same plot at $q = (0.213\ 0.213\ 1.464)$ in the A/S-type [96].

As mentioned before, the 1:2:2 stoichiometric sample exhibits both an antiferromagnetic order phase and a superconducting phase (so-called A/S-type). Figure 4.10 (a) depicts the temperature dependence of C/T of the A-type and A/S-type $CeCu_2Si_2$ single crystals in zero field [95]. A/S-type $CeCu_2Si_2$ shows a transition into the incommensurate SDW order phase at $T_N \sim 0.7$ K and the superconducting phase at $T_c \sim 0.5$ K. Figure 4.10 (b) depicts the temperature dependence of integrated neutron intensity of the magnetic Bragg peak at $q = (0.22\ 0.22\ 1.45)$ in A-type and $q = (0.213\ 0.213\ 1.464)$ in the A/S-type $CeCu_2Si_2$ [96]. The intensity increases while below T_N, whereas above T_N it disappears both in the A and A/S-types. However, in A/S-type $CeCu_2Si_2$, the magnetic signal rapidly decreases below T_c and finally vanishes at $T = 400$ mK.

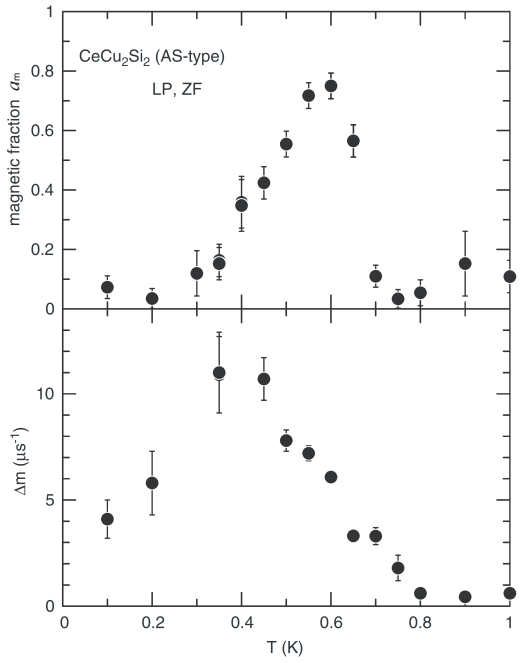

Figure 4.11: μSR measurements performed on the A/S-type $CeCu_2Si_2$ single crystal in zero field [92]. (a) The temperature dependence of the magnetic volume fraction $a_{\rm m}$. (b) The temperature dependence of the depolarization rate $\Delta_{\rm m}$.

Here the question arises: whether the SDW order and superconductivity compete with each other. However, since the magnetic Bragg intensities are written as the product of the square of the ordered magnetic moment and the magnetic volume, we cannot answer this question from the neutron scattering measurements.

In order to see the microscopic nature of the A/S-phase, μSR measurements were performed on an A/S-type single crystal ($T_N \sim 0.7$ K, $T_c \sim 0.5$ K) [92]. In Ref. [92], the μSR relaxation function $G(t)$ was fitted by

$$G(t) = a_{\rm m} G_{\rm m}(t) + a_{\rm pm} G_{\rm pm}(t), \qquad a_{\rm m} + a_{\rm pm} = 1, \tag{4.7}$$

where $a_{\rm m}$ and $a_{\rm pm}$ are the magnetic and paramagnetic (superconducting) volume fractions, respectively. The first term describes the depolarization in the magnetic volume with depolarization rate $\Delta_{\rm m}$ and the second term describes the depolarization in the paramagnetic volume with depolarization rate $\Delta_{\rm pm}$. Below T_N, $\Delta_{\rm m}$, which represents the SDW order parameter, increases with decreasing temperature. Importantly,

a_m rapidly decreases while Δ_m still increases just below T_c. This indicates that the SDW-ordered regions are expelled by the superconducting region in the superconducting state. Therefore, the phase separation with a first order transition from SDW to superconducting phase occurs at low temperatures.

4.6 S-phase in $CeCu_2Si_2$

4.6.1 Prototypical heavy-fermion Superconductor

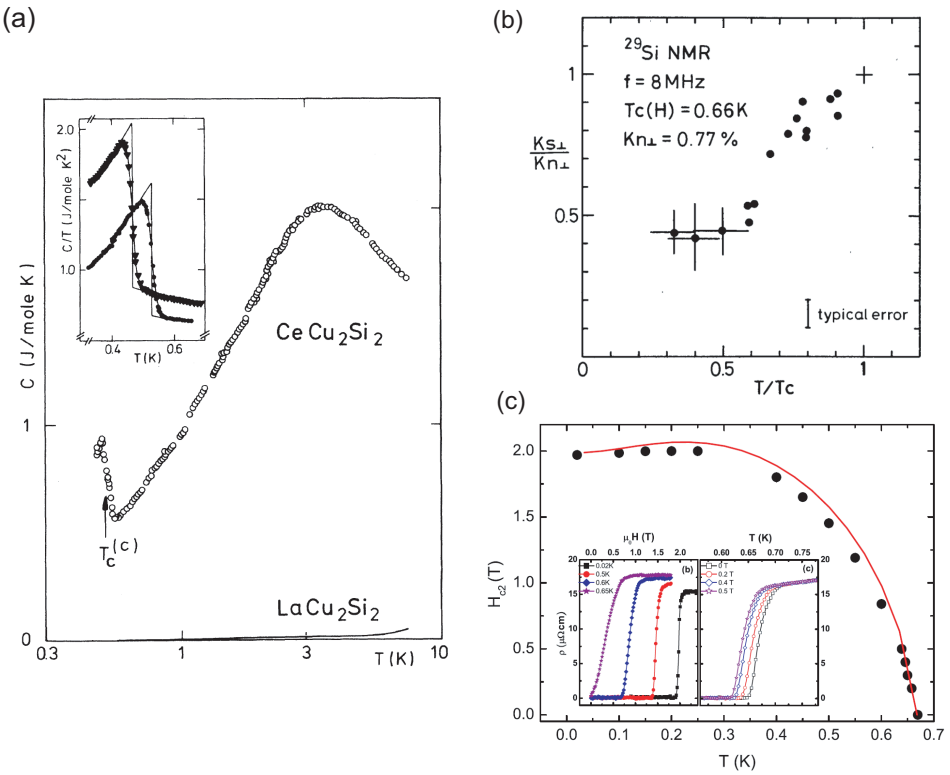

Figure 4.12: (a) C vs. T in zero field. Inset shows C/T vs. T of two other $CeCu_2Si_2$ samples [3] (b) Temperature dependence of the normalized NMR Knight shift [97]. (c) H-T phase diagram.

Again, $CeCu_2Si_2$ is a prototypical heavy-fermion superconductor with a T_c of 0.6 K, discovered by F. Steglich in 1979 [3]. The large specific heat jump at T_c indicates that the heavy electrons form Cooper pairs (Figure 4.12 (a)). The remarkable decrease of the NMR Knight shift below T_c (Figure 4.12 (b)) [97,98] and the Pauli-limited behavior of H_{c2} [99] (Figure 4.12 (c)) indicate the spin-singlet superconductivity.

4.6.2 Superconductivity near magnetic instability

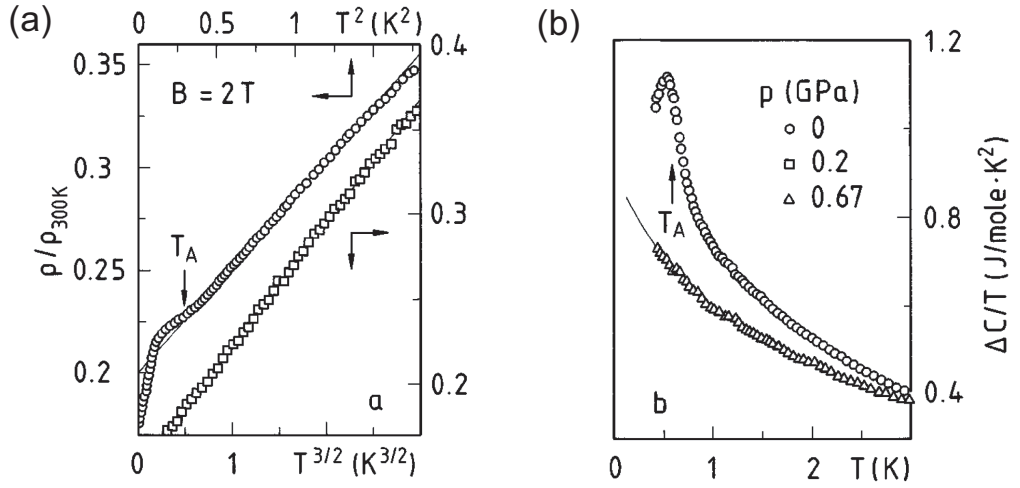

Figure 4.13: (a) $\rho/\rho_{300\mathrm{K}}$ vs. T^2 (upper scale) and $\rho/\rho_{300\mathrm{K}}$ vs. $T^{3/2}$ (lower scale), (b) γ vs T at $B = 2$ T and at $p = 0$, 0.2, and 0.67 GPa in an A-type $CeCu_2Si_2$ polycrystal [100] .

Schematic phase diagram for $CeCu_2Si_2$ (Figure 4.2 (b)) tells us that the superconductivity emerges when the AF order is suppressed by increasing the external parameter g. Here the question arises whether there actually is an antiferromagnetic QCP in $CeCu_2Si_2$.

Figure 4.13 depicts the temperature dependence of the resistivity ρ and the electronic specific heat coefficient γ of an A-type $CeCu_2Si_2$ polycrystal for $B = 2$ T and at $p = 0$, 0.2, and 0.67 GPa [100]. At ambient pressure, the transition into A-phase is observed and ρ shows the T^2 heavy Landau Fermi-liquid behavior at $T > T_A$. On the other hand, at $p > p_c \sim 0.1$ GPa, the A-phase is completely suppressed, and superconductivity occurs instead at 0 T. Importantly, both ρ and γ show non-Fermi-liquid behavior above p_c, i.e.,

$$\rho = \rho_0 + \beta T^{3/2} \tag{4.8}$$

$$\gamma = \gamma_0 - \alpha T^{1/2}. \tag{4.9}$$

These temperature dependencies are expected for three-dimensional antiferromagnetic quantum critical fluctuations [12, 101, 102]. Moreover, ρ and γ in S-type single crystal

at ambient pressure, where the same situation occurs as in the A-type at $p > p_c$, also show non-Fermi-liquid behavior at low fields (Figure 4.14). These results suggest that the superconductivity emerges in the vicinity of the three-dimensional SDW QCP. At high fields, the magnetic-field-induced recovery of T^2 Fermi-liquid behavior appears in ρ, which is similar to other heavy-fermion compounds in the vicinity of QCPs, such as $CeCoIn_5$ and $YbRh_2Si_2$ [103, 104].

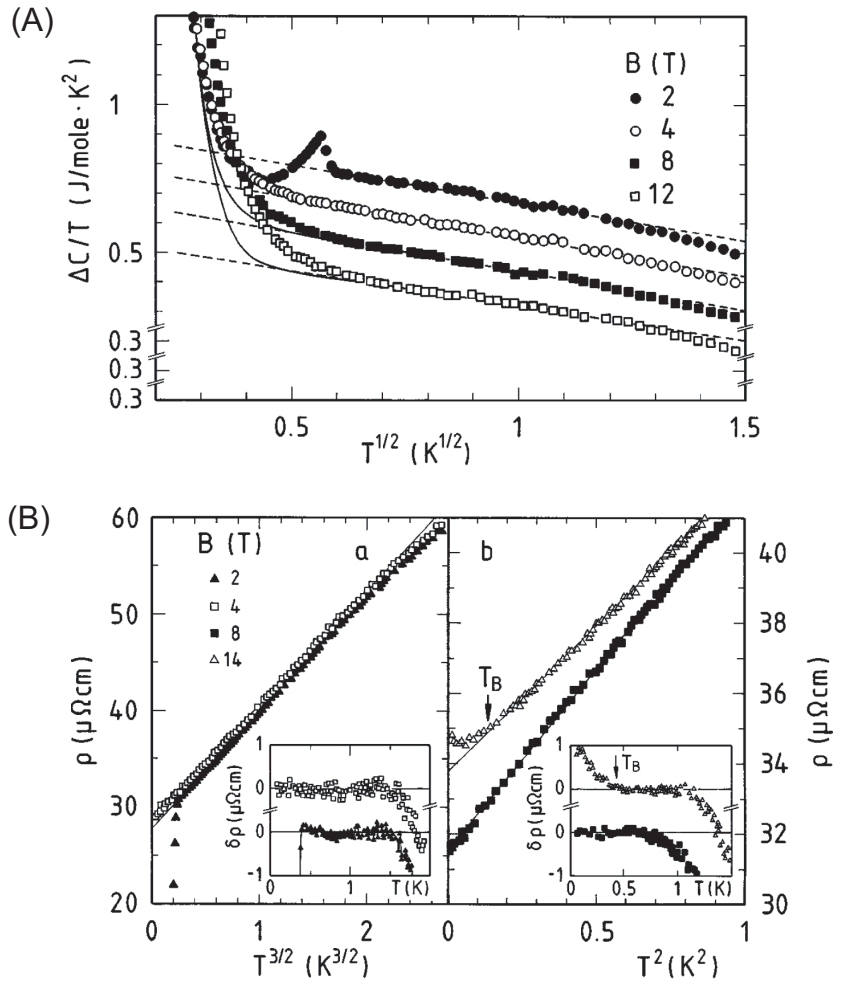

Figure 4.14: (A) γ vs. $T^{1/2}$ at ambient pressure for several magnetic fields in an S-type $CeCu_2Si_2$ single crystal. (B-a) ρ vs. $T^{3/2}$ at low fields and (B-b) ρ vs. T^2 at high fields at ambient pressure in an S-type $CeCu_2Si_2$ single crystal. At high fields, the signature of a field induced SDW ordered B-phase [105] transition was observed at T_B [100].

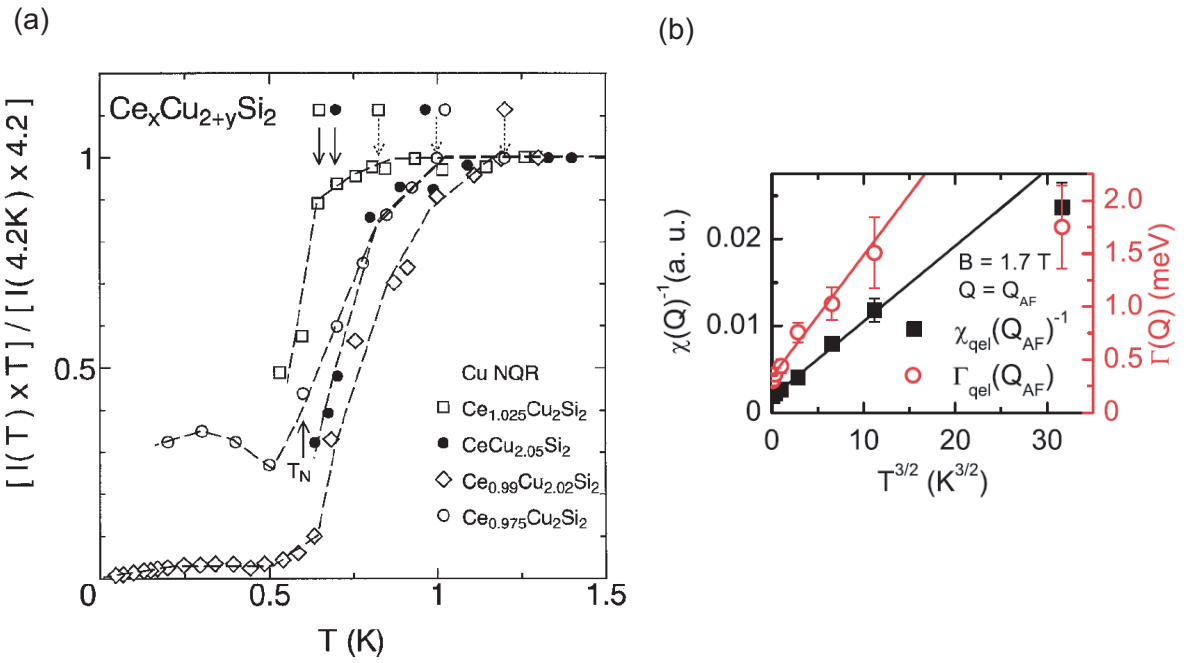

Figure 4.15: (a) Cu-NQR intensity multiplied by temperature $I \times T$ vs T normalized by $I \times T$ at 4.2 K in polycrystal $Ce_xCu_{2+y}Si_2$ [106]. $CeCu_{2.05}Si_2$ and $Ce_{1.025}Cu_2Si_2$ exhibit bulk superconductivity. Dotted and solid arrows indicate T_m and T_c, respectively. (b) Neutron scattering results for $Q = Q_{\rm AF}$ at $B = 1.7$ T [107]. $\chi^{-1}(Q_{\rm AF})$ vs $T^{3/2}$ (black symbols) and $\Gamma(Q_{\rm AF})$ vs. $T^{3/2}$ (red symbols) in the normal state. The small residual value at $T = 0$ is due to the fact that this sample is slightly away from the AF QCP.

Other measurements also provide evidence for the existence of the AF QCP. The Cu-NQR measurements in polycrystal $Ce_xCu_{2+y}Si_2$ [106] revealed the decrease in NQR intensity I multiplied by temperature T, $I \times T$, below T_m but far above T_c due to a critical slowing down of the magnetic response. This unusual magnetic phase with slow magnetic fluctuations is expelled below T_c by the superconducting state.

Neutron scattering measurements [107] in the normal state of S-type $CeCu_2Si_2$ revealed that the temperature dependences of both the inverse spin susceptibility $\chi^{-1}(Q_{\rm AF})$ and energy width of the quasielastic contribution to the neutron scattering intensity $\Gamma(Q_{\rm AF})$ which describes the fluctuation rate obey a $T^{3/2}$-law, as expected for a three-dimensional SDW QCP [101,102]. This result indicates the critical slowing down of the magnetic response.

These results, therefore, have led to a wide belief that antiferromagnetic fluctuations are responsible for the pairing interaction in $CeCu_2Si_2$.

4.6.3 Two distinct superconducting domes

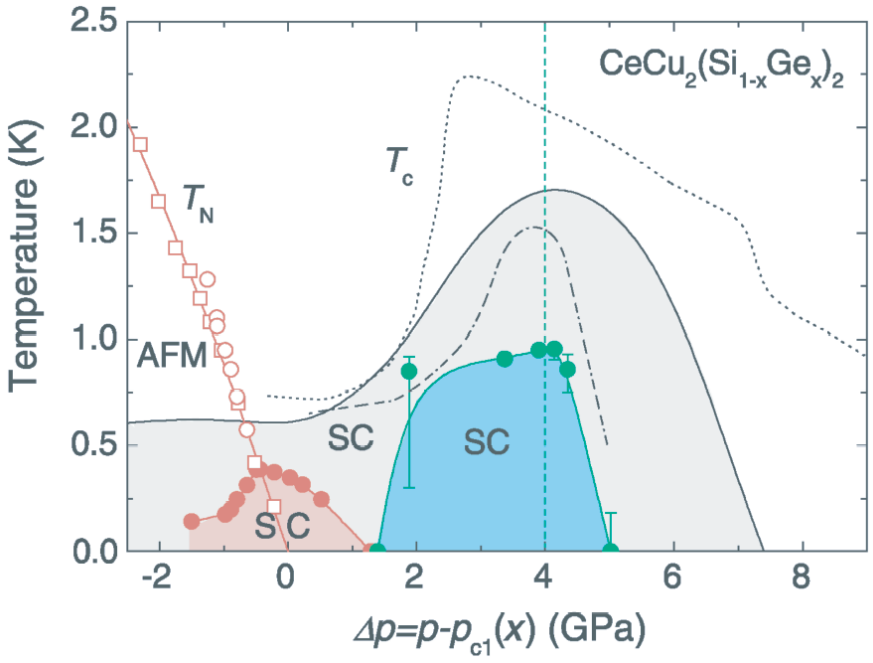

Figure 4.16: T-p phase diagram in $CeCu_2(Si_{1-x}Ge_x)_2$ [108]. The open and closed symbols indicate T_N and T_c, respectively. p_{c1} is defined as the pressure at the AF QCP. T_cs in pure $CeCu_2Si_2$ (p_{c1} = 0.4 GPa) are shown by the dotted line [109] and dashed-dotted line [110]. T_cs in pure $CeCu_2Ge_2$ (p_{c1} = 11.5 GPa) are shown by the continuous line [111]. The circles and squares represent $CeCu_2(Si_{0.9}Ge_{0.1})_2$ (p_{c1} = 1.5 GPa) and $CeCu_2(Si_{0.75}Ge_{0.25})_2$ (p_{c1} = 2.4 GPa), respectively.

The superconducting dome of pure $CeCu_2Si_2$ (Figure 4.2 (b)) extends to the high pressure region and T_c reaches its maximum far away from the AF QCP [109, 110]. It has been thought that there may be second quantum critical point on the high-pressure side of the T-p phase diagram. In order to reveal this, a doping study on $CeCu_2Si_2$ was performed [108] via the partial substitution of Si by isoelectronic Ge. This partial substitution causes a widening of the lattices and enhanced disorder scattering which will decrease T_c. The doping study revealed that there are two distinct superconducting domes (Figure 4.16). The lower superconducting dome (red dome, in Figure 4.16) saddles the magnetic QCP. On the other hand, the higher superconducting dome (blue dome, in Figure 4.16) develops far away from AF QCP and T_c reaches its maximum at around $\Delta p \sim 4$ GPa, where a volume collapse transition related to an abrupt valence

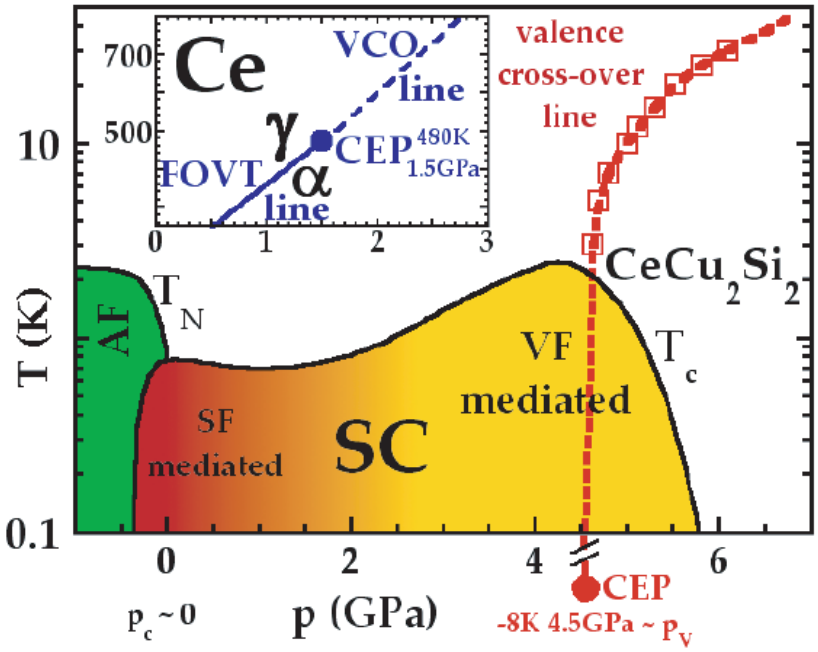

Figure 4.17: T-p phase diagram in pure $CeCu_2Si_2$ [113]. Valence crossover line and its critical end point (CEP) are determined by the pressure dependence of the resistivity data. T_c reaches its maximum at CEP. Inset shows the T-p phase diagram of elementary Ce. The first order valence transition (FOVT) line and the valence crossover (VCO) line have been determined by several measurements [115, 116].

change of the Ce ion is observed [112]. Moreover, another pressure study on a pure $CeCu_2Si_2$ single crystal reported that the critical end point of the valence cross-over line exists at $T = -8$ K and $p = 4.5$ GPa (corresponding to $\Delta p \sim 4$ GPa in Figure 4.16) at which T_c reaches maximum [113]. Indeed, at $\Delta p \sim 4$ GPa, the T-linear resistivity, enhanced residual resistivity, and steep drop of the A-coefficient in ρ are observed and well explained by the valence fluctuation mechanism [114]. These results indicate that the superconductivity in the high-p region is mediated by valence fluctuations.

To summarize above, superconductivity in the low-p regions occurs in the vicinity of the AF QCP, and hence is thought to be mediated by spin-fluctuations. On the other hand, superconductivity in the high-p regions occurs in the vicinity of the critical end point of the valence crossover, and hence is thought to be mediated by valence fluctuations.

4.7 Superconducting gap structure

4.7.1 Sign-changing – inelastic neutron scattering

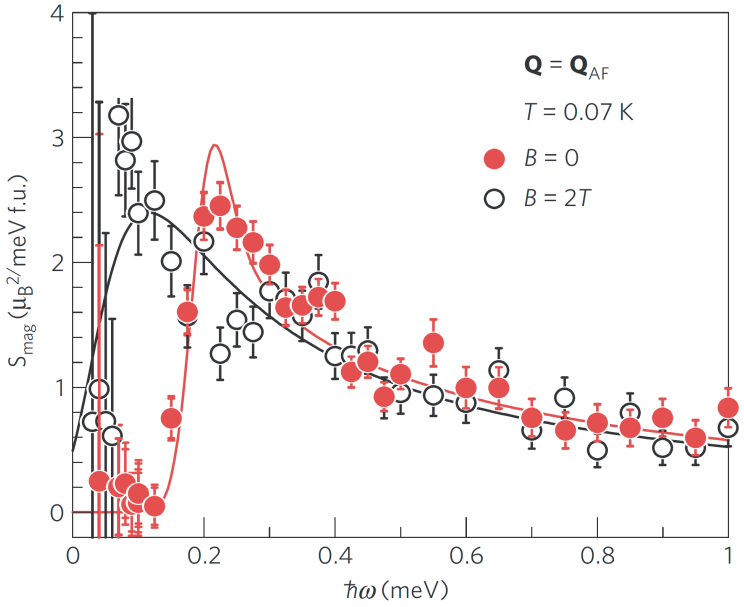

Figure 4.18: Inelastic magnetic response at $\boldsymbol{Q}_{\mathrm{AF}} = (0.215\ 0.215\ 1.458)$ and $T = 0.07$ K. In the superconducting state ($B = 0$ T), magnetic response enhances around $\hbar\omega_{\mathrm{gap}} \sim 0.2$ meV [82].

Inelastic neutron scattering measurements on an S-type single crystal reported an enhancement of the inelastic magnetic response at around $\hbar\omega_{\mathrm{gap}} \sim 0.2$ meV in the superconducting state (Figure 4.18) [82]. Since the peak position is lower than the superconducting gap $\hbar\omega = 2\Delta \sim 2.6$ meV determined by NQR measurements [106, 117], the enhancement could be interpreted in terms of a spin-resonance expected in superconductors with a sign-changing gap.

However, the enhancement is very broad compared to some cuprates [118] and $CeCoIn_5$ (Figure 4.19) [119], so it is not clearly a spin-resonance peak which is expected to be sharp in energy. Moreover, recent calculations show that a broad maximum at $\hbar\omega \sim 2\Delta$ appears even in superconductors without sign-changing gaps [120]. Therefore, the neutron scattering results do not provide conclusive evidence for a sign-changing gap structure.

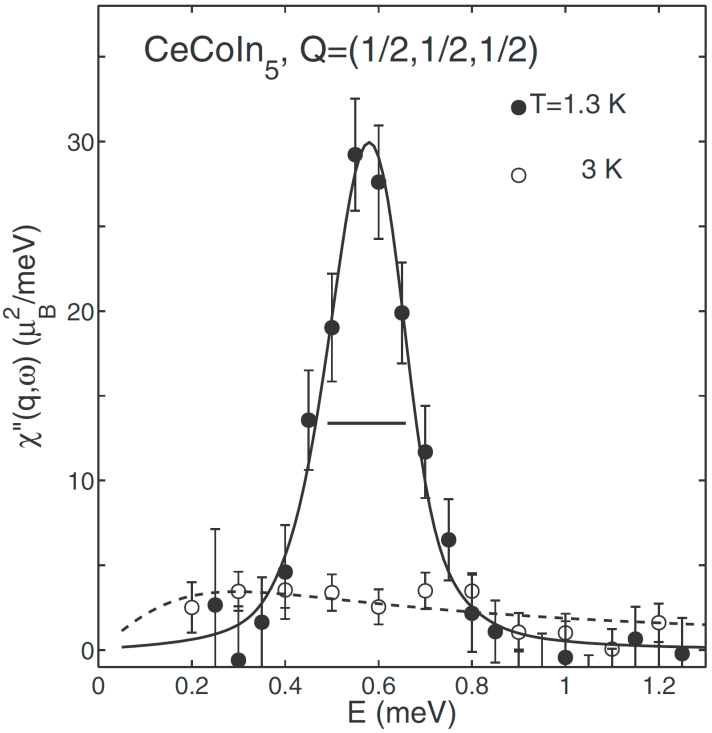

Figure 4.19: Energy dependence of the imaginary part of the dynamical spin susceptibility at $\boldsymbol{Q}_{\mathrm{AF}} = (1/2\ 1/2\ 1/2)$, at $T = 1.3$ K (SC state) and 3 K (normal state) in the d-wave superconductor $CeCoIn_5$. A sharp spin resonance develops in the superconducting state [119].

4.7.2 Line nodes – nuclear quadrupole resonance

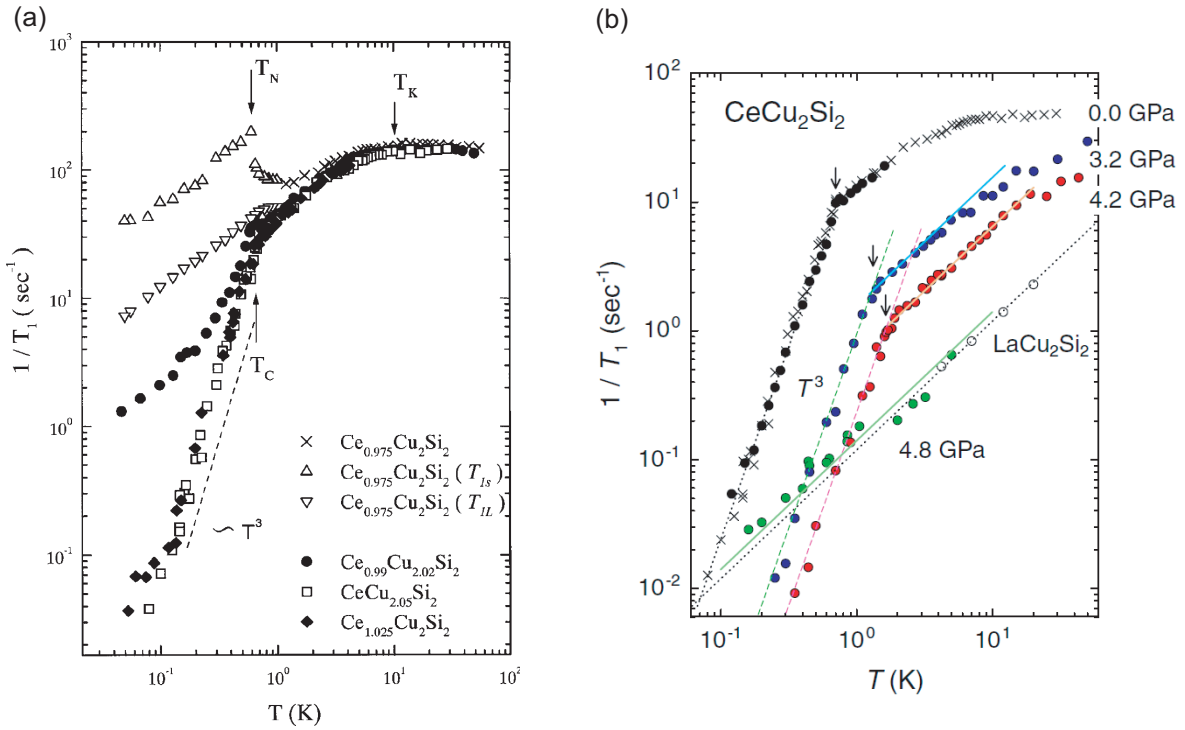

Figure 4.20: (a) $1/T_1$ vs T in polycrystalline $Ce_xCu_{2+y}Si_2$ at ambient pressure [106]. $CeCu_{2.05}Si_2$ and $Ce_{1.025}Cu_2Si_2$ exhibit superconductivity below T_c. T_N and T_K denote the AFM transition temperature and Kondo temperature, respectively. (b) $1/T_1$ vs. T under several pressures in polycrystalline $CeCu_{2.05}Si_2$ [117].

So far, several groups have performed nuclear quadrupole resonance (NQR) measurements on $CeCu_2Si_2$ [106, 117]. Figure 4.20 shows the temperature dependence of the nuclear spin-lattice relaxation time $1/T_1$ in the superconducting state for the polycrystalline samples of $Ce_xCu_{2+y}Si_2$. In the bulk superconducting samples $CeCu_{2.05}Si_2$ (denoted by $CeCu_2Si_2$ in [117]) and $Ce_{1.025}Cu_2Si_2$, $1/T_1$ decreases rapidly just below T_c and shows the T^3-dependence which can be characterized by unconventional superconductivity with line nodes such as high-T_c cuprates. Moreover, both samples do not show the Hebel-Slichter coherence peak, which is expected for a conventional s-wave superconductor. Therefore, the superconducting gap is suggested to have line nodes in $CeCu_2Si_2$ at ambient pressure.

NQR measurements under high pressure have also been performed (Figure 4.20 (b))

[117]. In the normal state, $1/T_1$ decreases with increasing pressure because the system goes away from the AFM QCP with pressure. The sudden drop of $1/T_1$ and suppression of superconductivity between 4.2 GPa and 4.8 GPa are related to the valence transition around 4.5 GPa [113]. More importantly, the T^3-dependence and no Hebel-Slichter coherence peak in $1/T_1$ just below T_c also observed even under high pressure far from the AFM QCP. Therefore, these results suggest that the superconducting gap has line nodes both in low-P and high-P superconducting domes.

It should be noted, however, that the T-dependence of $1/T_1$ will be complex in a multiband system. In addition, as discussed in Fe-pnictides, the lack of the Hebel-Slichter peak can be explained in the framework of the nodeless $s_{\pm}$-wave state with impurity scattering [121]. Furthermore, the Hebel-Slichter peak can be suppressed even in the s_{++}-wave state due to the inelastic quasiparticle damping [122]. Hence, it is difficult to determine the gap symmetry of the multiband superconductor $CeCu_2Si_2$ from the present NQR data.

4.7.3 Loop nodal $s_{\pm}$ − LDA + U calculation

In ref. [88], superconducting gap has been calculated using linearized gap equation in multiorbital systems. The information of multipole fluctuations discussed in ref. [88] is included in the susceptibility $\chi_{\ell m,\ell' m'}(\boldsymbol{q})$. They calculated by second-order perturbation and obtained complex loop-nodal $s_{\pm}$-wave state for the LDA + U Fermi surface (Figure 4.21 (a)), which is similar to that discussed in Fe-pnictide $BaFe_2(As_{1-x}P_x)_2$ [123]. However, since the obtained nodal feature is not symmetry protected, the loop-nodes can be lifted by, for example, the intrinsic attractive on-site pairing term. Moreover, the nodal structure strongly depends on the magnitude of U. Therefore, detailed experimental study is required to identify the theoretical calculation.

The $s_{\pm}$-wave state is also obtained for the LDA Fermi surface (Figure 4.21 (b)), which is suggested to be realized in the high-p region.

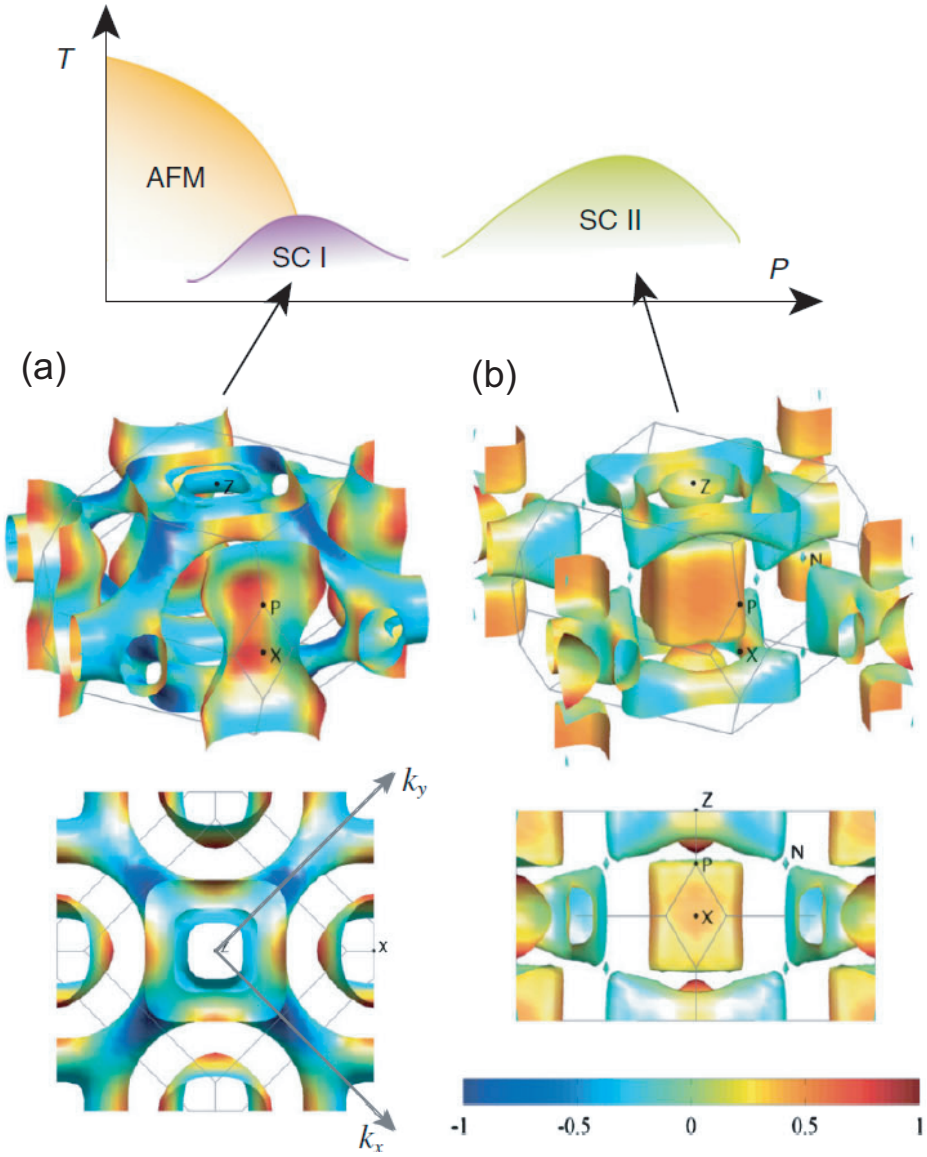

Figure 4.21: Superconducting gap structures calculated in ref. [88]. (a) $s_{\pm}$-wave state obtained in the LDA + U Fermi surface. (b) $s_{\pm}$-wave state obtained in the LDA Fermi surface, which is suggested to be realized in the high-p region.

4.7.4 Multigap – specific heat

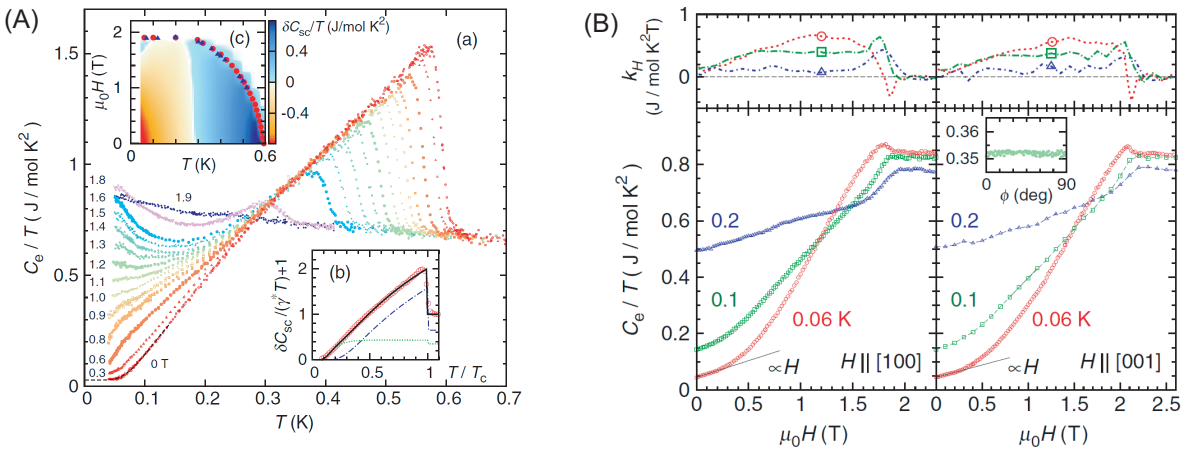

Figure 4.22: (A) The temperature dependences of C_e/T in several magnetic fields. (B) The field dependences of C_e/T at several temperatures. Inset: the angular dependence of C_e/T [124].

Recent specific heat measurements on s-type single crystal down to 40 mK exhibited unexpected behavior [124]. At $H = 0$ T, although the C_e/T exhibits a nearly T-linear dependence down to 100 mK which is consistent with the NQR results [106,117], C_e/T shows a large positive curvature in the lowest temperature region (Figure 4.22 (A-a)). Indeed, the data can be fit by exponential function: $C_e = A\exp(-\Delta_0/T) + \gamma_0 T$ where $\Delta_0 = 0.39$K and $\gamma_0 = 0.028$ J/(mol·K^2) (dashed line in Fig. 4.22 (A-a)). The small but finite γ_0 suggests the inclusion of non-superconducting 'A' type material. Since $CeCu_2Si_2$ is mutiband superconductor [88], they fit the data using two gaps model. The overall T-dependence of C_e/T is well reproduced by two-gap model within the BCS framework with $\Delta_1/k_BT_c = 1.76$ (65 %) and $\Delta_2/k_BT_c = 0.7$ (35 %) (Figure 4.22 (A-b)). In fact, major full and minor line-nodes gaps model cannot reproduce the T-dependence of C_e/T ([124], Supplemental material). The field dependence of C_e/T exhibits H-linear dependence at low-H at the lowest temperature, which is in contrast to the $\sqrt{H}$ behavior for nodal superconductors (Figure 4.22 (B)). Moreover, no-angular oscillation of C_e/T was observed (Figure 4.22 (B) inset).

These results imply the fully-gapped superconductivity. However, since the specific heat is dominated by the parts of the Fermi surface where the Fermi velocity is low (or

mass is large), the C/T data suggest the absence of line nodes in the *heavy* electron band. Indeed, C/T data [124] has only excluded the possibility of $d_{x^2-y^2}$-wave symmetry. The possibilities of existence of nodes in the *light* hole bands, e.g. d_{xy}-wave symmetry, still remain. Therefore, experimental studies which can sensitively detect the low-energy quasiparticle excitations from light-band, such as thermal conductivity and penetration depth measurements, are required to reveal the true superconducting gap structure.

4.8 Purpose of this study

As discussed in the previous section, despite considerable experimental and theoretical efforts for almost 40 years, the superconducting gap symmetry of $CeCu_2Si_2$ has been still unclear. In order to clarify the superconducting gap structure, we performed the low-temperature specific heat, thermal conductivity, and magnetic penetration depth measurements in *S*-type single crystal $CeCu_2Si_2$. In fact, the thermal conductivity and magnetic penetration depth are dominated by the low mass, high velocity parts of the Fermi surface. Moreover, in order to reveal whether there is sing change in the superconducting order parameter, we also performed electron-irradiation experiments, which is known to be a phase-sensitive probe.

5 Study of superconducting gap structure in prototypical heavy-fermion $CeCu_2Si_2$

5.1 Introduction

As mentioned before, the discovery of heavy-fermion superconductivity in $CeCu_2Si_2$ was an important turning point in the history of superconductivity, because it led to the birth of research on non-electron-phonon mediated pairing [3, 125]. Heavy-fermion superconductivity is usually intimately related to magnetism in some form. In particular, superconductivity often occurs in the vicinity of a zero-temperature magnetic instability known as a quantum-critical point (QCP) [125–127]. Thus it is widely believed that in these materials Cooper pairing is mediated by magnetic fluctuations. The superconducting gap structure is a direct consequence of the mechanism producing the pairing. In phonon-mediated conventional superconductors with a finite on-site pairing amplitude in real space (Fig. 5.1 A), the superconducting gap function $\Delta(\boldsymbol{k})$ is isotropic in momentum space (Fig. 5.1 B). On the other hand, in magnetically-mediated unconventional superconductors, the on-site pairing amplitude vanishes due to strong Coulomb repulsion and superconductivity is caused by a potential that is only attractive for particular displacements between the electrons forming the Cooper pair [13] (Fig. 5.1 C). A net attractive interaction can be realized if the superconducting gap changes sign on the Fermi surface (Fig. 5.1 D and E). In some materials, such as cuprates [16] and the heavy-fermion $CeCoIn_5$, the sign change of the gap leads to gap functions with nodes along certain momentum directions [127–129]. However, in certain iron-pnictide superconductors the gap function has no nodes but may change sign between the well separated electron and hole Fermi surface pockets [67, 130].

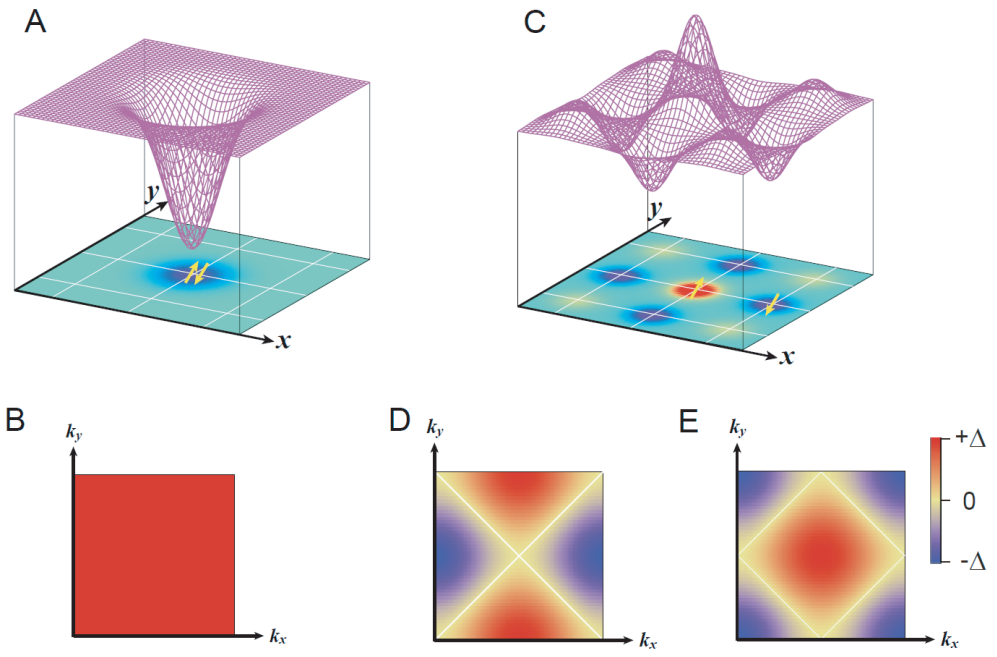

Figure 5.1: Pairing interactions and superconducting gap functions. (**A**) The pairing interaction in real space for attractive force mediated by electron-phonon interaction. Blue part corresponds to attractive region. Both electrons composing the Cooper pair can occupy the same atom. (**B**) Isotropic s-wave superconducting state in the momentum space driven by the attractive force shown in (**A**). The gap function is constant in the entire Brillouin zone. (**C**) The pairing interaction due to magnetic fluctuations. The red and blue parts correspond to repulsive and attractive regions, respectively. Both electrons cannot occupy the same atom. Superconductivity is caused by the attractive part of the oscillating pairing interaction. (**D** and **E**) Examples for the gap structures in momentum space for unconventional superconductors caused by an on-site repulsive force, $d_{x^2-y^2}$ symmetry (**D**) and $s_{\pm}$ -symmetry (**E**). Due to the sign change of the superconducting order parameter, the gap vanishes on the yellow lines. When the Fermi surface crosses these lines, gap nodes appear.

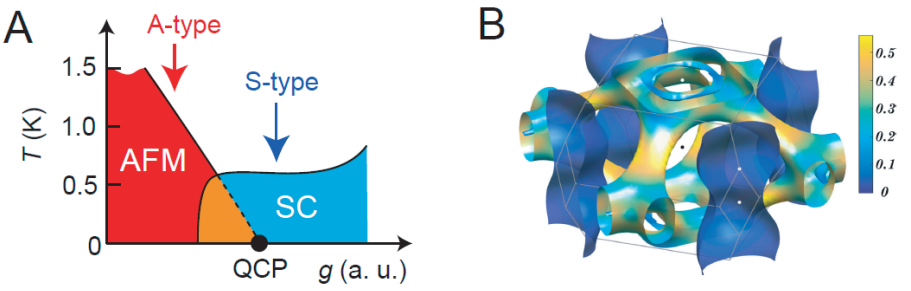

Figure 5.2: Phase diagrams and electronic structure of $CeCu_2Si_2$. (**A**) Schematic T-g phase diagram, where g is a non-thermal control parameter, such as pressure, substitution or Cu-deficiency. Red and blue arrows indicate two different types of $CeCu_2Si_2$ with antiferromagnetic (A-type) and superconducting (S-type) ground states, respectively. S-type crystal locates very close to AFM QCP. (**B**) Fermi surface colored by the Fermi velocity (in units of 10^6 m/s) obtained by the LDA + U calculation [88]. Fermi surface consists of separated electron and hole pockets: heavy electron pockets with cylindrical shape around X-point and rather complicated light hole pockets centred at Γ-point.

$CeCu_2Si_2$ is a prototypical heavy-fermion superconductor near a magnetic instability [3, 108] with transition temperature $T_c \simeq 0.6$ K [3] (Fig. 5.2 A). The Fermi surface consists of heavy electron and light hole bands (Fig. 5.2 B) [88]. Slight variations in stoichiometry lead to 'A' type and 'S' type crystals; the former is antiferromagnetic and the latter is superconducting without magnetic ordering but lying very close to a magnetic QCP (Fig. 5.2 A). The in-plane resistivity above T_c in zero field, which follows a power-law $\rho_a = \rho_{a0} + AT^{\epsilon}$ with $\epsilon = 1.5$ along with the heat capacity, which follows $C/T = \gamma_N - a\sqrt{T}$ in the normal state slightly above the upper critical field, are consistent with non-Fermi-liquid behaviors expected for three dimensional antiferromagnetic quantum critical fluctuations [100, 131, 132]. A critical slowing down of the magnetic response revealed by neutron scattering [107] and nuclear quadrupole resonance (NQR) [106] in the normal state, has also been attributed to antiferromagnetic fluctuations near the QCP. These results have led to a wide belief that antiferromagnetic fluctuations are responsible for the pairing interaction in $CeCu_2Si_2$. Here, we report a comprehensive study of the gap structure of S-type $CeCu_2Si_2$ using several different probes which together are sensitive to the gap structure on all Fermi surface sheets and also any possible changing of gap-sign between sheets.

5.2 Experimental

5.2.1 Sample characterization

S-type single crystals of $CeCu_2Si_2$ grown by the flux method [133] were provided by Dr. Christoph Geibel group at Max Planck Institute for Chemical Physics of Solids.

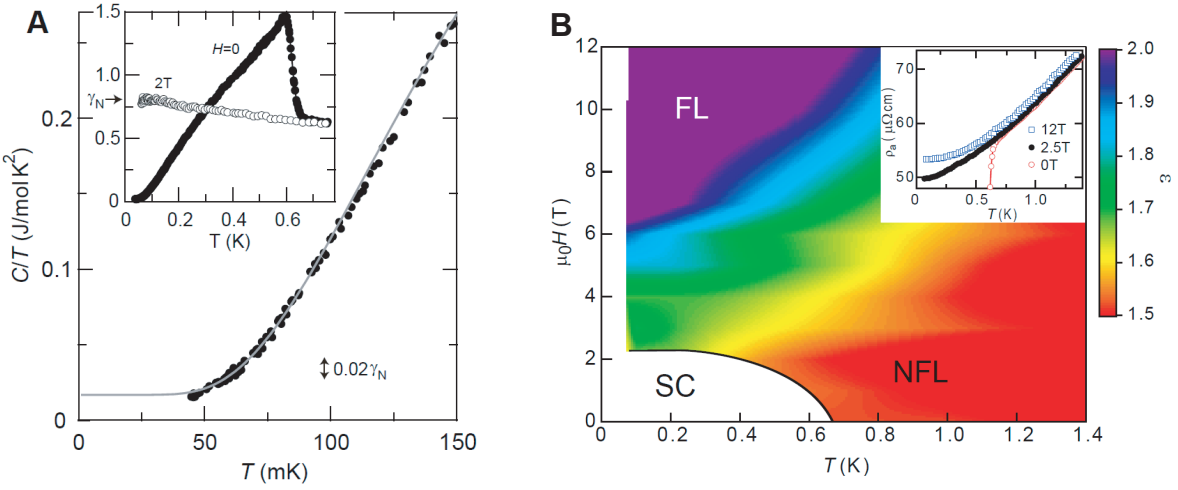

Figure 5.3: (**A**) Inset shows the specific heat divided by temperature C/T in zero field and in the normal state at $\mu_0 H = 2\,\mathrm{T}$ for $\boldsymbol{H} \| ab$ plane. The main panel shows C/T at low temperatures. The gray solid line is an exponential fit of the data, yielding $\Delta = 0.39\,\mathrm{K}$. (**B**) H-T phase diagram with color-coding of T-exponent (ϵ) of the in-plane electrical resistivity, $\rho(T) = \rho_0 + AT^{\epsilon}$ for $\boldsymbol{H} \parallel c$. Inset shows the T-dependence of $\rho(T)$ in zero field and in magnetic fields of 2.5 and 12 T applied along the c axis.

Figure 5.3 (A) and its inset depict the specific heat C/T for a crystal used in the present study. The specific heat was measured by the standard quasi-adiabatic heat-pulse method. In this sample, no discernible Schottky contribution is observed. At zero field C/T exhibits a sharp transition at T_c and tends towards saturation at the lowest temperature. The C/T value at the lowest temperature, $15\,\mathrm{mJ/K^2mol}$, is less than 2% of γ_N, which is nearly half of that in the previous report [124]. This extremely small C/T indicates a very low number of quasiparticle excitations and that any inclusion of non-superconducting 'A' type material is very small. The data are well fitted by an exponential T dependence showing a lack of thermally induced excitations at the lowest

temperatures in agreement with a previous study [124]. A linear behavior does not fit our C/T data but if it was forced to then a fit above 90 mK in Figure 5.3 (A) would lead to an unphysical negative intercept at $T = 0$ K. This is indicative of a fully gapped state with minimal disorder. More precisely, since the specific heat is dominated by the parts of the Fermi surface where the Fermi velocity is low (or mass large), the C/T data suggest the absence of line nodes in the *heavy* electron band.

Figure 5.3 (B) depicts the H-T phase diagram with color-coding of T-exponent (ϵ) of the in-plane electrical resistivity ρ_a in our sample. The in-plane resistivity above T_c in zero field, which follows a power-law $\rho_a = \rho_{a0} + AT^{\epsilon}$ with $\epsilon = 1.5$ is consistent with non-Fermi-liquid behaviors expected for three dimensional antiferromagnetic quantum critical fluctuations [100, 131, 132]. The magnetic-field-induced recovery of Fermi-liquid behavior with $\epsilon = 2$ shown in Figure 5.3 (B) bears striking resemblance to other heavy-fermion compounds in the vicinity of QCPs, such as $CeCoIn_5$ and $YbRh_2Si_2$ [103, 104].

5.2.2 Methods

Thermal conductivity

The thermal conductivity κ was measured using a dilution refrigerator down to 40 mK ($\sim T_{c0}/15$) by a standard four-wire steady-state method in several configurations, i.e, (i) $\boldsymbol{Q} \parallel a$, $\boldsymbol{H} \parallel c$. (ii) $\boldsymbol{Q} \parallel \boldsymbol{H} \parallel c$ and (iii) $\boldsymbol{Q} \parallel c$, $\boldsymbol{H} \parallel a$. The contacts were made by indium solder with contact resistance less than few mΩ. We examined the effect of superconductivity of indium by applying small magnetic field and found no discernible difference.

Penetration depth

The penetration depth λ was measured down to 50 mK by our collaborators T. Takenaka *et al.* at the university of Tokyo. The temperature dependence of penetration depth $\lambda(T)$ was measured by using the tunnel diode oscillator technique operating at $\sim$ 14 MHz. Weak ac magnetic field ($\sim 1\mu$ T) is applied along the c axis inducing screening currents in the ab plane.

Electron irradiation

Electron irradiation was performed in the electron irradiation facility SIRIUS at École Polytechnique. We used electrons with incident energy of 2.5 MeV for which the energy transfer from the impinging electron to the lattice is above the threshold energy for the formation of vacancy interstitial (Frenkel) pairs that act as point defects. In order to prevent the point defect clustering, irradiation is performed at 25 K using a H_2 recondenser. For 1 C/cm^2 dose, irradiation causes about 1-2 vacancies per 1000 Ce atoms. However, because of the defect annihilations due to annealing effect at room temperature, the number of vacancies is not directly proportional to the dose density.

5.3 Results

5.3.1 Thermal conductivity

Temperature dependence

Thermal conductivity is a bulk, directional probe of the quasiparticle excitations, and like penetration depth, is dominated by the high velocity parts of the Fermi surface [26]. Figure 5.4 (A) and its inset show the T-dependence of the in-plane thermal conductivity κ_a/T (with heat current $\boldsymbol{Q} \parallel a$). The thermal conductivity in the normal state at $T \to 0$ slightly above the upper critical field for $\boldsymbol{H} \parallel c$ obeys well the Wiedemann-Franz law, $\kappa_a/T = L_0/\rho_a$ (Fig. 5.4 (A), dashed line), where L_0 is the Lorenz number and ρ_a is the in-plane resistivity. At the lowest temperatures κ_a/T extrapolated to $T = 0$ is zero within our experimental resolution and is at least an order of magnitude smaller than that expected for line nodes. Indeed, at $T = 40$ mK, in-plane phonon conductivity $\kappa_a^{\rm ph}/T$ estimated by using the Wiedemann-Franz law in the normal state, $\kappa_a^{\rm ph}/T = \kappa_a(H_{c2})/T - L_0/\rho_a(T)$, is ~ 4 mW/K^{2}m, which yields in-plane quasiparticle thermal conductivity $\kappa_a^{\rm qp}/T \sim$3 mW/K^{2}m in zero field. The residual thermal conductivity expected for line node is estimated as $\kappa_{a0}/T \approx (L_0/\rho_{a0}) \cdot (\xi_{ab}/\ell_{ab}) \sim$ 32 mW/K^{2}m [30]. Here $\xi_{ab} = 4.7$ nm is the in-plane coherence length estimated by the orbital limited upper critical field of 14.7 T for $\boldsymbol{H} \parallel c$ [124] and $\ell_{ab} \sim 8$ nm is the

in-plane mean free path obtained from $\ell_{ab} = v_F^{ab}\lambda_{ab}^2(0)\mu_0/\rho_{a0}$, using $\rho_{a0} = 43\,\mu\Omega$cm, $\lambda_{ab}(0) = 700\,$nm from Hall-probe magnetometery measurements of the lower critical field H_{c1} and the average of in-plane Fermi velocity $v_F^{ab} \sim 5800\,$m/s for the hole band calculated by LDA + U, taking into account the mass renormalization $z = 1/50$ which is determined by the specific heat measurements. These results indicate that the residual thermal conductivity at $T \to 0$, if present, is considerably smaller than that expected for line node. A similar conclusion is obtained for the out-of-plane thermal conductivity κ_c ($\boldsymbol{Q} \parallel c$).

Field dependence

Further evidence for the absence of any nodes is provided by H-dependence of κ. In fully gapped superconductors, where all the quasiparticles states are bound to vortex cores, the magnetic field hardly affects κ except in the vicinity of the upper critical field H_{c2}. By contrast, in nodal superconductors, heat transport is dominated by the delocalized quasiparticles. In the presence of a supercurrent with velocity $\boldsymbol{v}_s$ around the vortices, the energy of a quasiparticle with momentum $\boldsymbol{p}$ is Doppler shifted relative to the superfluid by $E(\boldsymbol{p}) \to E(\boldsymbol{p}) - \boldsymbol{v}_s \cdot \boldsymbol{p}$, giving rise to an initial steep increase of $\kappa(H)/T \propto \sqrt{H}$ for line nodes and $\kappa(H)/T \propto H \log H$ for point nodes. Thermal conductivity selectively probes the quasiparticles with momentum parallel to the thermal current ($\boldsymbol{p}\cdot\boldsymbol{Q} \neq 0$) and with momentum perpendicular to the magnetic field ($\boldsymbol{p}\times\boldsymbol{H} \neq 0$) because $\boldsymbol{H} \perp \boldsymbol{v}_s$ [26]. To probe the quasiparticle excitations on the whole Fermi surface, we performed measurements for three different configurations, (i) κ_a for $\boldsymbol{H} \parallel c$, (ii) κ_c for $\boldsymbol{H} \parallel c$, and (iii) κ_c for $\boldsymbol{H} \parallel a$ (Figs. 5.4 (B), (C)). For (i) and (ii), thermal conductivity selectively probes the quasiparticles with in-plane momentum, whereas for (iii) it selectively probes quasiparticles with out-of-plane momentum. For configuration (ii), there is structure at $\mu_0 H \sim 1\,$T, which indicates the presence of multiple superconducting gaps. The H-dependence for configuration (iii) shown in Figure 5.4 (D) is similar to configuration (i). Remarkably, in all configurations, magnetic field hardly affects the thermal conduction in the low field regime (Figs. 5.4 (B), (C)); the field-induced enhancement, $\Delta\kappa(H) \equiv \kappa(H) - \kappa(0)$ is less than 1/100 of the normal-

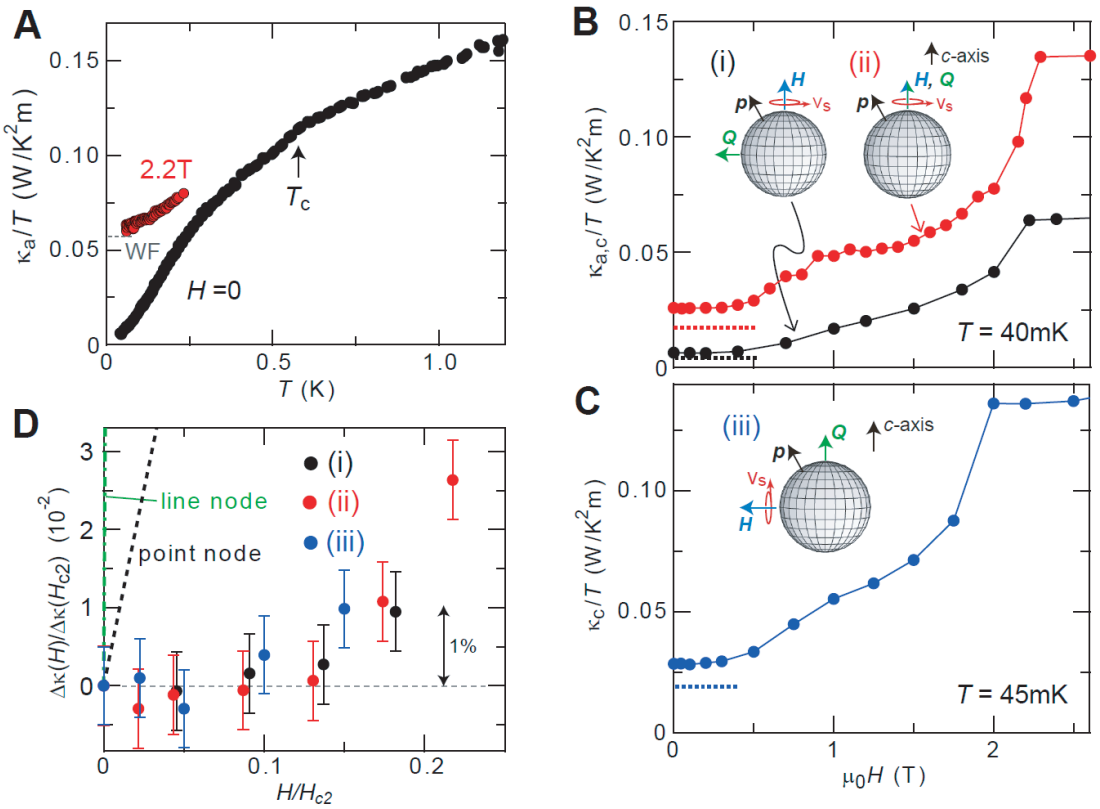

Figure 5.4: Thermal conductivity of $CeCu_2Si_2$ for various directions of thermal current and magnetic field. (**A**) Temperature dependence of the in-plane thermal conductivity divided by temperature κ_a/T in zero field and in magnetic field of $\mu_0 H = 2.2\,\mathrm{T}$ applied along the c axis. WF refers to κ/T at $T \to 0$ calculated from the Wiedemann-Franz law. (**B**) Field dependence of κ/T for two different configurations. (i) κ_a/T ($\boldsymbol{Q} \parallel a$) in $\boldsymbol{H} \parallel c$ and (ii) κ_c/T ($\boldsymbol{Q} \parallel c$) in $\boldsymbol{H} \parallel c$. In these configurations, thermal conductivity selectively probes the excited quasiparticles with in-plane momentum. The dashed horizontal lines represent the phonon contribution, κ_{ph}/T, estimated from the WF law above upper critical field (see the main text). (**C**) Field dependence of κ_c/T for configuration (iii), where $\boldsymbol{Q} \parallel c$ and $\boldsymbol{H} \parallel a$. In this case, thermal conductivity selectively probes the excited quasiparticles with out-of-plane momentum. (**D**) Field-induced enhancement of thermal conductivity $\Delta\kappa(H) \equiv \kappa(H) - \kappa(0)$ normalized by the normal state value, $\Delta\kappa(H)/\Delta\kappa(H_{c2})$ for the configurations (i), (ii) and (iii) plotted against the magnetic field normalized by the upper critical fields. Black and green broken lines represent the field dependencies expected for line and point nodes.

state value $\Delta\kappa(H_{c2})$ even at $H/H_{c2} \sim 0.15$, demonstrating a vanishingly small number of delocalized quasiparticles excited by magnetic field. As shown by the dashed lines in Fig. 5.4 (D), $\Delta\kappa(H)/\Delta\kappa(H_{c2})$ is far smaller than that expected for line and point nodes.

5.3.2 Penetration depth

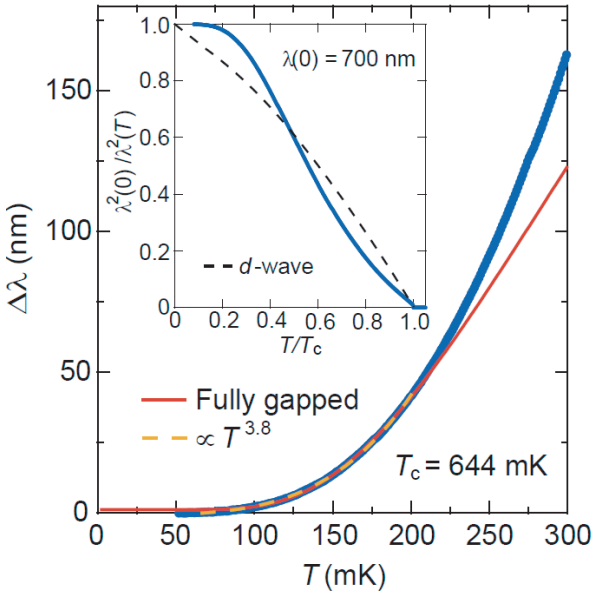

Figure 5.5: Temperature dependent change in the in-plane penetration depth $\Delta\lambda$ in a single crystal of $CeCu_2Si_2$. The dashed (solid) line is a fit to a power-law (exponential) temperature dependence up to 0.2 K. Inset shows the normalized superfluid density $\rho_s(T) = \lambda^2(0)/\lambda^2(T)$ as a function of T/T_c, extracted by using a value of $\lambda(0) = 700$ nm. The dashed line is the temperature dependence of $\rho_s(T)$ in the simple d-wave case.

The magnetic penetration depth measures the surface of the sample (to depth of a few micron), and is dominated by the low mass, high velocity parts of the Fermi surface. We find that the in-plane penetration depth $\lambda_{ab}(T)$ at low temperatures ($T \ll T_c$) exhibits strong curvature and tends towards becoming T-independent (Fig. 5.5), similar to the results for C/T and in contrast to the T-linear dependence expected for clean superconductors with line nodes [134]. A fit to a power-law T dependence $\Delta\lambda(T)(= \lambda_{ab}(T) - \lambda_{ab}(0)) \propto T^n$ gives a high power $n > 3.5$, which is practically indistinguishable from the exponential dependence expected in fully gapped superconductors. Since λ_{ab} measures the in-plane superfluid response, our data show that gap nodes, at which quasiparticles with momentum parallel to the ab plane are excited, are absent on the light hole bands.

For more detailed analysis of the superconducting gap structure, the absolute value of $\lambda_{ab}(0)$ is necessary so that the normalized superfluid density $\rho_s(T) = \lambda^2_{ab}(0)/\lambda^2_{ab}(T)$

can be calculated. Unfortunately previous measurements have reported a wide spread of values of $\lambda_{ab}(0)$ (120 to 950 nm [135, 136]) which probably reflects differences in sample stoichiometry between studies. We have estimated $\lambda_{ab}(0) = 700\,\text{nm}$ from Hall-probe magnetometery measurements of the lower critical field H_{c1} in the same samples as used for our $\Delta\lambda(T)$ study. The inset of Fig. 5.5 shows the T-dependence of $\rho_s(T)$. Near T_c, we find convex curvature in $\rho_s(T)$, which is a signature frequently observed in multigap superconductors [137].

5.3.3 Electron irradiation

The above measurements of $C(T)$, $\Delta\lambda(T)$ and $\kappa(T, H)$ demonstrate the absence of any kind of nodes in the gap function on the whole Fermi surface. To further distinguish between the remaining possible gap structures we have measured the effect of impurity-induced pair-breaking on T_c. These measurements are a sensitive test of possible sign changes in the gap function either between different Fermi surface sheets or on a single sheet. Impurity induced scattering between sign changing areas of Fermi surface will reduce T_c very rapidly whereas if there is no sign change the reduction will be much slower or even zero. To introduce impurity scattering by homogeneous point defects in a controllable way, we employed electron irradiation with incident energy of 2.5 MeV [78], which according to our calculation of electron scattering cross sections, mainly removes Ce atoms. Electronic-structure calculations of $CeCu_2Si_2$ [88] show that the bands crossing the Fermi level are mainly composed of a single Ce f-manifold, so removing Ce atoms by electron irradiation will act as a strong point scatterer and induce both intra- and inter-band impurity scattering with similar amplitude.

Our results show that T_c of $CeCu_2Si_2$ is decreased slowly with increasing dose (inset of Fig. 5.6). The transition width remains almost unchanged after irradiation, indicating good homogeneity of the point defects. The Kondo temperature ($T_K \sim$ 15 K) almost unchanged after irradiation (Figure 5.7). Moreover, the resistivity increases almost parallelly via irradiation. Therefore, Ce vacancy increases the elastic part of scattering without changing c-f mixing. In- and out-of-plane residual resistivities reach $\rho_{a0} \sim 120\,\mu\Omega\text{cm}$ and $\rho_{c0} \sim 110\,\mu\Omega\text{cm}$ for irradiated crystals (inset of

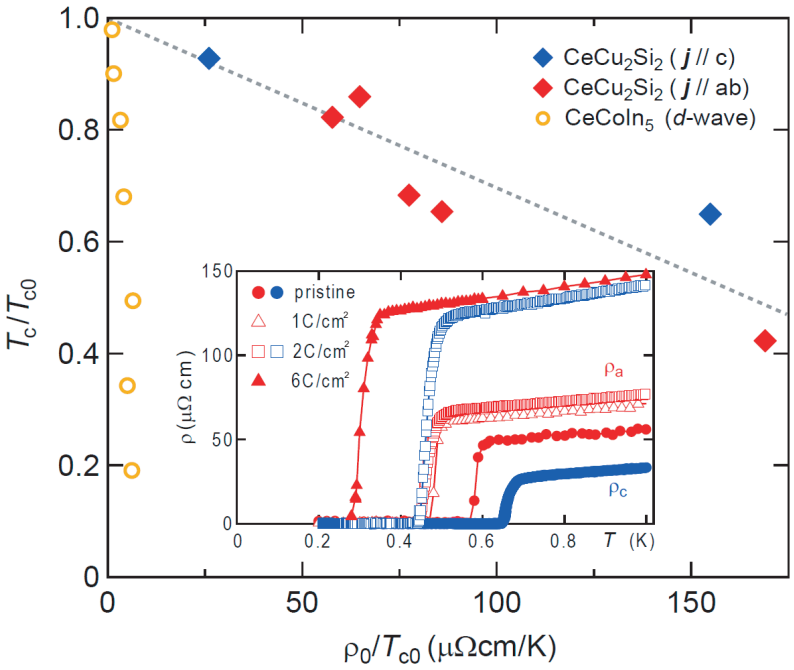

Figure 5.6: Pair-breaking effect of $CeCu_2Si_2$. Suppression of superconducting transition temperature T_c/T_{c0} as a function of ρ_0/T_{c0}, which is proportional to the pair breaking parameter, for $CeCu_2Si_2$ and Sn-substituted $CeCoIn_5$ (d-wave) [22]. Here T_{c0} is the transition temperature with no pair-breaking effect and ρ_0 is the residual resistivity. For $CeCu_2Si_2$, $T_{c0} = 0.71$ K is used. Inset shows the temperature dependence of resistivity in $CeCu_2Si_2$ before and after electron irradiation that creates point defects.

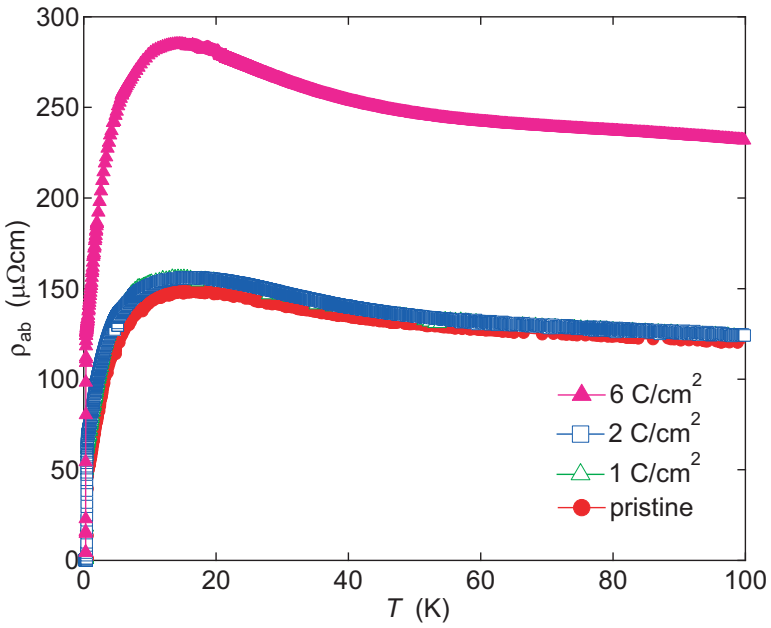

Figure 5.7: ρ_{ab} vs T in zero field. The Kondo temperature ($T_K \sim 15$ K) almost unchanged after irradiation.

Fig. 5.6). Using $\ell_j = v_F^j \lambda_j^2(0)\mu_0/\rho_{j0}$ ($j = ab$ or c), we obtain in- and out-of-plane mean free paths, $\ell_{ab} \sim 3.0\,\mathrm{nm}$ and $\ell_c \sim 1.8\,\mathrm{nm}$, respectively. Here, we used averaged in-plane (out-of-plane) Fermi velocity $v_F^{ab} \sim 5800\,\mathrm{m/s}$ ($v_F^c \sim 6800\,\mathrm{m/s}$) of the light hole band, $\lambda_c(0) = \lambda_{ab}(0)(\xi_{ab}/\xi_c) = 480\,\mathrm{nm}$, where in-plane and out-of-plane coherence lengths determined by the orbital limited upper critical fields, $\xi_{ab} = 4.7\,\mathrm{nm}$ and $\xi_c = 6.9\,\mathrm{nm}$, respectively. These mean free paths are obviously shorter than ξ_{ab} and ξ_c. For unconventional pairing symmetries such as d-wave, superconductivity is completely suppressed at $\ell \lesssim 4\xi$. In stark contrast, T_c of $CeCu_2Si_2$ is still as high as $\sim T_{c0}/2$ even for $\ell_c/\xi_c \sim 0.26$ and $\ell_{ab}/\xi_{ab} \sim 0.64$. We note that this ℓ/ξ is the upper limit value, because ℓ is estimated from the penetration depth and conductivity, both of which are governed by the light bands, while ξ is determined by the upper critical field which is governed by heavy bands. Thus this result demonstrates that superconductivity in $CeCu_2Si_2$ is robust against impurities. This is also seen clearly by comparison to the d-wave superconductor $CeCoIn_5$ [22], which has comparable effective mass and carrier number. Figure 5.6 displays the residual resistivity dependence of T_c/T_{c0}, where T_{c0} is the transition temperature with no pair breaking. In $CeCoIn_5$, T_c is suppressed to zero in the sample with ρ_0/T_{c0} smaller than $10\,\mu\Omega\mathrm{cm/K}$ [22], while T_c in $CeCu_2Si_2$ is still $\sim 50\,\%$ of T_{c0} even for the sample with ρ_0/T_{c0} larger than $150\,\mu\Omega\mathrm{cm/K}$, indicating that the pair breaking effect in $CeCu_2Si_2$ is fundamentally different from that in $CeCoIn_5$.

Comparison to other materials (cuprates and iron-pnictides) with sign changing gaps confirms the much weaker effect of impurities in $CeCu_2Si_2$. In Fig. 5.8 we plot the impurity induced T_c reduction in a number of materials as function of the scattering rate, estimated from ρ_0/λ, divided by T_{c0}. Plotting the data in this way takes out the effect of difference in T_c and carrier density between the different materials, and it can be seen that the T_c reduction in $CeCu_2Si_2$ is much weaker than the archetypal cuprate $YBa_2Cu_3O_7$ [138] which has a sign-changing $d_{x^2-y^2}$ gap function. The iron-pnictides $Ba(Fe_{0.76}Ru_{0.24})_2As_2$ [141] present an very unusual system where the $\boldsymbol{k}$-dependence of the scattering is critical to the effect of impurities on T_c. Assuming that the pairing in these materials is caused by a inter-band spin-fluctuation interactions, then the gap function will change sign between the electron and hole electron sheets ($s_\pm$ pairing).

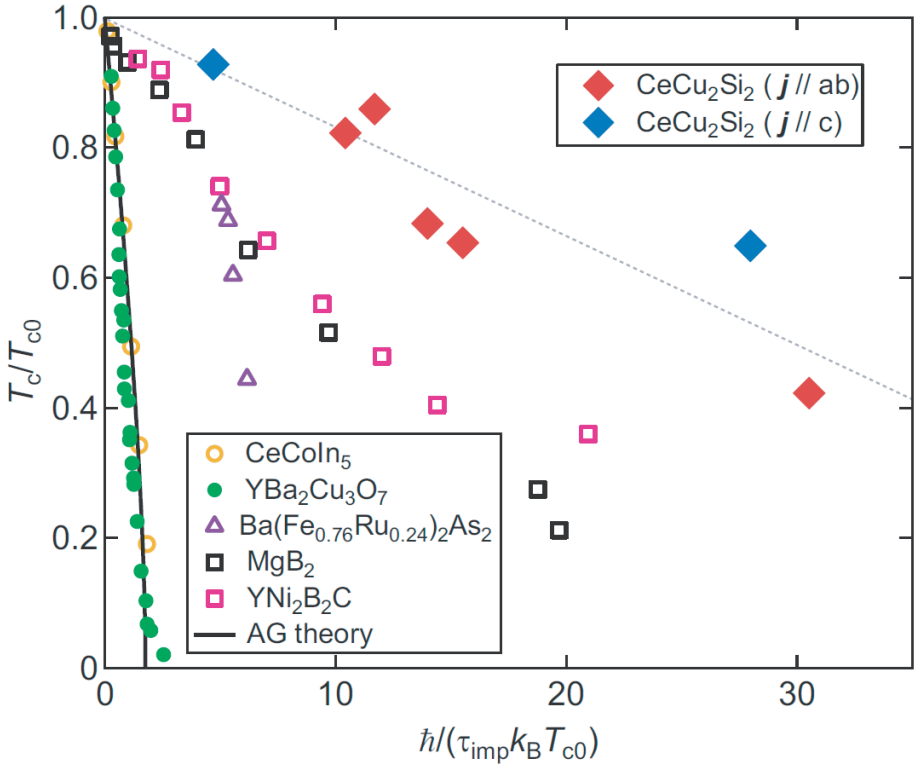

Figure 5.8: Comparison of impurity effect of $CeCu_2Si_2$ with those of other superconductors. Suppression of superconducting transition temperature T_c/T_{c0} as a function of dimensionless scattering rate $\hbar/\tau_{\rm imp}k_BT_{c0}$, where $\tau_{\rm imp}$ is the impurity scattering time estimated from residual resistivity ρ_0 and the penetration depth, $\tau_{\rm imp} = \mu_0\lambda_{ab}\lambda_c/\rho_0$. The solid line shows the prediction of the Abrikosov-Gorkov (AG) theory for an isotropic s-wave superconductor with magnetic impurities. We also plot the data for Sn-substituted $CeCoIn_5$ (d-wave) [22], electron-irradiated $YBa_2Cu_3O_{7-\delta}$ (d-wave) [138], electron-irradiated $Ba(Fe_{0.76}Ru_{0.24})_2As_2$ (possibly $s_\pm$-wave) [141], and neutron-irradiated MgB_2 [139] and YNi_2B_2C [140]. The value of T_{c0} is estimated by extrapolating two initial data points to zero $1/\tau_{\rm imp}$ limit. Rather weak pair-breaking effect in $Ba(Fe_{0.76}Ru_{0.24})_2As_2$ has been attributed to a large imbalance between intra- and interband scattering [141]. For MgB_2 data, we use the value of $\lambda_{ab}(0) = \lambda_c(0) = 100\,$nm [142]. For YNi_2B_2C data, we use $\lambda_{ab}(0) = 110\,$nm [143] and $\lambda_c(0) = \lambda_{ab}(0)H_{c2}^{ab}/H_{c2}^{c} = 140\,$nm [144], where H_{c2}^{ab} and H_{c2}^{c} are upper critical field parallel and perpendicular to the ab plane.

Inter-band impurity scattering will then increase ρ_0 and decrease T_c in a similar way to other sign-changing gap materials, however, if the scattering is purely intra-band then this would increase ρ_0 but would not decrease T_c [77]. It is highly unlikely that such an anomalous situation could occur in $CeCu_2Si_2$ because the Fermi surface sheets are not well separated and, as described above, Ce vacancies would produce non-$\boldsymbol{k}$-selective scattering.

The slow but finite reduction in T_c as function of ρ_0 we see in $CeCu_2Si_2$ can be explained qualitatively by the moderate gap anisotropy we have observed in our $C(T)$ and $\lambda(T)$ measurements. In cases where there is gap anisotropy, scattering will tend to average out the gap thus depressing T_c. However, crucially this will be at a much slower rate than for a sign changing gap, as illustrated in Fig. 5.8 by data for the non-sign changing s-wave superconductors MgB_2 [139] and YNi_2B_2C [140] which are known to have very anisotropic energy gaps. Our observed slower decrease in T_c as a function of impurity scattering in $CeCu_2Si_2$ compared to these materials is consistent with our observed moderate anisotropy.

5.4 Discussion

The combination of our measurements and previous results rules out all but one possible gap structure. The strong reduction of the spin susceptibility in the superconducting state observed by nuclear magnetic resonance Knight shift indicates spin singlet pairing [98] which rules out any odd-momentum (p or f) states, including those, such as the Balain-Werthamer state [145] which are fully gapped [146]. This is consistent with the observation that H_{c2} is Pauli limited [99]. In fact, in the present crystal, orbital-limited upper critical fields at $T = 0$ calculated from $H_{c2}^{\rm orb} = -0.7T_c(dH_{c2}/dT)_{T_c}$ are 10.0 and 14.7 T for $\boldsymbol{H} \parallel a$ and $\boldsymbol{H} \parallel c$, respectively. These values are much larger than the observed H_{c2} of 2.0 T for $\boldsymbol{H} \parallel a$ and 2.3 T for $\boldsymbol{H} \parallel c$.

Our observation that superconductivity is robust against inter-band and intra-band impurity scattering rules out any sign-changing gap functions such as d-wave or the recently proposed sign changing $s_\pm$ state [88]. Both the d-wave and $s_\pm$ states are

also highly unlikely because neither could be nodeless in $CeCu_2Si_2$ where the electron and hole Fermi surface sheets are not well separated. Finally, unconventional states which combine irreducible representations of the gap function, such as $d_{xy} + id_{x^2-y^2}$ or $s + id_{x^2-y^2}$ can be ruled out because such states would be highly sensitive to impurities and furthermore as these representations are not in general degenerate we would expect to see two distinct superconducting transitions. If there was accidental degeneracy, this would be broken by pressure or doping but no double transitions are observed in these conditions either [108]. This leads us to the surprising conclusion that the pairing in $CeCu_2Si_2$ is a fully-gapped non-sign changing s-wave state.

Previously, evidence for line-nodes in $CeCu_2Si_2$ has been suggested by measurements of the NQR relaxation rate $1/T_1$ where a T^3-dependence below T_c was observed [106]. However, these results would also be explained by the multigap nature of the superconductivity shown here by our $C(T)$, $\lambda(T)$ and $\kappa(H)$ measurements. Inelastic neutron scattering shows an enhancement of magnetic spectral weight at around $E \sim 2\Delta$ [82] which could be interpreted in terms of a spin-resonance expected in superconductors with a sign-changing gap. However, this enhancement is very broad compared with some cuprates [118] and $CeCoIn_5$ [119] so is not clearly a resonance peak which is expected to be sharp in energy. Moreover, recent calculations show that a broad maximum at $E \sim 2\Delta$ appears even in superconductors without sign changing gaps [120]. Hence the NQR and neutron results do not provide conclusive evidence for a sign changing gap structure and are not necessarily inconsistent with the results here.

At first sight our finding that $CeCu_2Si_2$ has a non-sign changing s-wave gap function casts doubt on the long-standing belief that it is a magnetically-driven superconductor, despite overwhelming evidence that this compound is located near a magnetic QCP. It is unlikely that the conventional electron-phonon interaction could overcome the on-site strong Coulomb repulsive force, which enhances the effective mass to nearly one thousand times the bare electron mass, in this heavy fermion metal which does not have high energy strong-coupled phonons. Recent dynamic mean field theory calculations however, have shown that robust s-wave superconductivity driven by *local* spin-fluctuations is found in solutions to the Kondo-lattice model which is commonly

used to describe heavy-fermion metals [147]. Other recent theoretical work has shown that electron-phonon coupling could be strongly enhanced near a quantum critical point again stabilizing s-wave superconductivity [148]. Our results might therefore support a new type of unconventional superconductivity where the gap function is s-wave but the pairing is nevertheless driven by strong magnetic fluctuations.

6 Conclusion

Study of superconducting gap structure in prototypical heavy-fermion $CeCu_2Si_2$

We performed low-temperature specific heat, thermal conductivity and magnetic penetration depth measurements in $CeCu_2Si_2$, demonstrating the absence of gap nodes at any point on the Fermi surface. Moreover, electron-irradiation experiments revealed that the superconductivity survives even when the electron mean free path becomes substantially shorter than the superconducting coherence length. This indicates that superconductivity is robust against impurities, implying that there is no sign change in the gap function. These results show that, contrary to long-standing belief, heavy electrons with extremely strong Coulomb repulsions can condense into a fully-gapped s-wave superconducting state, which has an on-site attractive pairing interaction.

References

[1] H. Kamerlingh Onnes, Comm. Phys. Lab. Univ. Leiden, Nos. 122 and 124 (1911).

[2] J. Bardeen, L. N. Cooper and J. R. Schrieffer, Phys. Rev. **108**, 1175 (1957).

[3] F. Steglich, F. Aart, C. D. Bredl, W. Lieke, D. Meschede, W. Franz and H. Schafer, Phys. Rev. Lett. **43**, 1892 (1979).

[4] J. G. Bednorz and K. A. Müller, Z. Phys. B **64**, 189 (1986).

[5] N. Takeshita, A. Yamamoto, A. Iyo and H. Eisaki, J. Phys. Soc. Jpn. **82**, 023711 (2013).

[6] Y. Kamihara, H. Hiramatsu, M. Hirano, R. Kawamura, H. Yanagi, T. Kamiya and H. Hosono, J. Am. Chem. Soc. **128**, 10012 (2006).

[7] Y. Kamihara, T. Watanabe, M. Hirano and H. Hosono, J. Am. Chem. Soc. **130**, 3296 (2008).

[8] T. Park, F. Ronning, H. Q. Yuan, M. B. Salamon, R. Movshovich, J. L. Sarrao, and J. D. Thompson, Nature **440**, 65 (2006).

[9] T. Shibauchi, A. Carrington, and Y. Matsuda, Annu. Rev. Condens. Matter Phys. **5**, 113 (2014).

[10] D. Faltermeier, J. Barz, M. Dumm, M. Dressel, N. Drichko, B. Petrov, V. Semkin, R. Vlasova, C. Meźière, and P. Batail, Phys. Rev. B **76**, 165113 (2007).

[11] B. Keimer, S. A. Kivelson, M. R. Norman, S. Uchida, and J. Zaanen, Nature **518**, 179 (2015).

[12] T. Moriya and K. Ueda, Adv. In Phys. **49**, 555606 (2000).

[13] D. J. Scalapino, Phys. Rep. **250**, 329 (1995).

[14] M. Sigrist and T. M. Rice, Phys. Rep. **67**, 503 (1995).

[15] D. J. Van Hariingen, Rev. Mod. Phys. **67**, 515 (1995).

[16] C. C. Tsuei and J. R. Kirtley, Rev. Mod. Phys. **72**, 969 (2000).

[17] M. Tinkham, Introduction to Superconductivity, McGraw-Hill, Inc., New York, 2nd edition, 1996.

[18] P. W. Anderson, J. Phys. Chem. Solids **11**, 26-30 (1959).

[19] A. A. Abrikosov and L. P. Gor'kov, Sov. Phys. JETP **12**, 1243 (1961).

[20] V. Ambegaokar and A. Griffin, Phys. Rev. **137**, A1151 (1965).

[21] A. I. Larkin, JETP Letters **2**, 130 (1965).

[22] E. D. Bauer, F. Ronning, C. Capan, M. J. Graf, D. Vandervelde, H. Q. Yuan, M. B. Salamon, D. J. Mixson, N. O. Moreno, S. R. Brown, J. D. Thompson, R. Movshovich, M. F. Hundley, J. L. Sarrao, P. G. Pagliuso and S. M. Kauzlarich, Phys. Rev. B **73**, 245109 (2006).

[23] K. Miyake, J. Magn. Magn. Mat. **63/64**, 411-419 (1987).

[24] C. Caroli, P. G. de Gennes and J. Matricon, Phys. Lett. **9**, 307 (1964).

[25] G. E. Volovik, JETP Lett. **58**, 469 (1993).

[26] Y. Matsuda, K. Izawa and I. Vekhter, J. Phys.: Cond. Mat. **18**, R705 (2006).

[27] N. W. Ashcroft and N. D. Mermin, Solid State Physics, Thomson Learning (1976).

[28] M. Sutherland, D. G. Hawthorn, R. W. Hill, F. Ronning, S. Wakimoto, H. Zhang, C. Proust, E. Boaknin, C. Lupien, L. Taillefer, R. Liang, D. A. Bonn, W. N. Hardy, R. Gagnon, N. E. Hussey, T. Kimura, M. Nohara, and H. Takagi, Phys. Rev. B **67**, 174520 (2003).

[29] R. O. Pohl and B. Stritzker, Phys. Rev. B **25**, 3608 (1982).

[30] M. J. Graf, S. K. Yip, J. A. Saul and D. Rainer, Phys. Rev. B **53**, 15147 (1996).

[31] H. Shakeripour, C. Petrovic and L. Taillefer, New Journal of Phys. **11**, 055065 (2009).

[32] M. F. Smith, J. Paglione, M. B. Walker and L. Taillefer, Phys. Rev. B **71**, 014506 (2005).

[33] T. Yamashita, Y. Tokiwa, D. Terazawa, M. Nagao, S. Watauchi, I. Tanaka, T. Terashima and Y. Matsuda J. Phys. Soc. Jpn. **85**, 073707 (2016)

[34] Y. Mizuguchi, H. Fujihisa, Y. Gotoh, K. Suzuki, H. Usui, K. Kuroki, S. Demura, Y. Takano, H. Izawa and O. Miura, Phys. Rev. B **86**, 220510 (2012).

[35] Y. Mizuguchi, S. Demura, K. Deguchi, Y. Takano, H. Fujihisa, Y. Gotoh, H. Izawa, and O. Miura, J. Phys. Soc. Jpn. **81**, 114725 (2012).

[36] H. Usui, K. Suzuki, and K. Kuroki, Phys. Rev. B **86**, 220501 (2012).

[37] T. Agatsuma and T. Hotta, J. Magn. Magn. Mater. **400**, 73 (2016).

[38] X. Wan, H.-C. Ding, S. Y. Savrasov, and C.-G. Duan, Phys. Rev. B **87**,115124 (2013).

[39] T. Yildirim, Phys. Rev. B **87**, 020506 (2013).

[40] Y. Liang, X. Wu, W.-F. Tsai, and J. Hu, Front. Phys. **9**, 194 (2014).

[41] Y. Yang, W.-S. Wang, Y.-Y. Xiang, Z.-Z. Li, and Q.-H. Wang, Phys. Rev. B **88**, 094519 (2013).

[42] G. B. Martins, A. Moreo, and E. Dagotto, Phys. Rev. B **87**, 081102(R) (2013).

[43] L. Jiao, Z. Weng, J. Liu, J. Zhang, G. Pang, C. Guo, F. Gao, X. Zhu, H.-H. Wen, and H. Q. Yuan, J. Phys.: Condens. Matter **27**, 225701 (2015).

[44] Z. R. Ye, H. F. Yang, D. W. Shen, J. Jiang, X. H. Niu, D. L. Feng, Y. P. Du, X. G. Wan, J. Z. Liu, X. Y. Zhu, H. H. Wen and M. H. Jiang, Phys. Rev. B **90**, 045116 (2014).

[45] J. Liu, D. Fang, Z. Wang, J. Xing, Z. Du, S. Li, X. Zhu, H. Yang and H.-H. Wen, Europhys. Lett. **106**, 67002 (2014).

[46] M. Nagao, S. Demura, K. Deguchi, A. Miura, S. Watauchi, T. Takei, Y. Takano, N. Kumada, and I. Tanaka, J. Phys. Soc. Jpn. **82**, 113701 (2013).

[47] T. Yamashita, Y. Shimoyama, Y. Haga, T. D. Matsuda, E. Yamamoto, Y. Onuki, H. Sumiyoshi, S. Fujimoto, A. Levchenko, T. Shibauchi and Y. Matsuda, Nature Physics **11**, 1720 (2015).

[48] Y. Kasahara, T. Iwasawa, H. Shishido, T. Shibauchi, K. Behnia, Y. Haga, T. D. Matsuda, Y. Onuki, M. Sigrist and Y. Matsuda, Phys. Rev. Lett. **99**, 116402 (2007).

[49] K. Yano, T. Sakakibara, T. Tayama, M. Yokoyama, H. Amitsuka, Y. Homma, P. Miranovi, M. Ichioka, Y. Tsutsumi and K. Machida, Phys. Rev. Lett. **100**, 017004 (2008).

[50] R. Okazaki, M. Shimozawa, H. Shishido, M. Konczykowski, Y. Haga, T. D. Matsuda, E. Yamamoto, Y. $\overline{\text{O}}$nuki, Y. Yanase, T. Shibauchi and Yuji Matsuda, J. Phys. Soc. Jpn **79**, 084705 (2010).

[51] G. Li, Q. Zhang, D. Rhodes, B. Zeng, P. Goswami, R. E. Baumbach, P. H. Tobash, F. Ronning, J. D. Thompson, E. D. Bauer and L. Balicas, Phy. Rev. B **88**, 134517 (2013).

[52] E. R. Schemm, R. E. Baumbach, P. H. Tobash, F. Ronning, E. D. Bauer, and A. Kapitulnik, Phys. Rev. B **91**, 140506(R) (2015).

[53] P. Goswami and L. Balicas, arXiv:1312.3632 (2013).

[54] Z. A. Xu, N. P. Ong, Y. Wang, T. Kakeshita and S. Uchida, Nature **406**, 486-488 (2000).

[55] Y. Wang, L. Li and N. P. Ong, Phys. Rev. B **73**, 024510 (2006).

[56] I. Ussishkin, S. L. Sondhi and D. A. Huse, Phys. Rev. Lett. **89**, 287001 (2002).

[57] V. Oganesyan and I. Ussishkin, Phys. Rev. B **70**, 054503 (2004).

[58] K. Behnia, J. Phys. Condens. Matter **21**, 113101 (2009).

[59] M. N. Serbyn, M. A. Skvortsov, A. A. Varlamov and Victor Galitski, Phys. Rev. Lett. **102**, 067001 (2009).

[60] K. Michaeli and A. M. Finkel'stein, Europhys. Lett. **86**, 27007 (2009).

[61] A. Levchenko, M. R. Norman and A. A. Varlamov, Phys. Rev. B **83**, 020506 (2011).

[62] R. Bel, K. Behnia, Y. Nakajima, K. Izawa, Y. Matsuda, H. Shishido, R. Settai and Y. Onuki, Phys. Rev. Lett. **92**, 217002 (2004).

[63] K. Izawa, K. Behnia, Y. Matsuda, H. Shishido, R. Settai, Y. Onuki and J. Flouquet, Phys. Rev. Lett. **99**, 147005 (2007).

[64] W. Higemoto, A. Koda, R. Kadono, Y. Kawasaki, Y. Haga, D. Aoki, R. Settai, H. Shishido and Y. $\overline{\text{O}}$nuki, J. Phys. Soc. Jpn. **71**, 1023-1026 (2002).

[65] H. Sumiyoshi and S. Fujimoto, Phys. Rev. B **90**, 184518 (2014).

[66] R. Bel, H. Jin, K. Behnia, J. Flouquet and P. Lejay, Phys. Rev. B **70**, 220501(R) (2004).

[67] P. J. Hirschfeld, M. M. Korshunov and I. I. Mazin, I. I., Rep. Prog. Phys. **74**, 124508 (2011).

[68] I. I. Mazin, D. J. Singh, M. D. Johannes and M. H. Du, Phys. Rev. Lett. **101**, 057003 (2008).

[69] K. Kuroki, H. Usui, S. Onari, R. Arita and H. Aoki, Phys. Rev. B **79**, 224511 (2009).

[70] S. Graser, T. A. Maier, P. J. Hirschfeld and D. J. Scalapino, New J. Phys. **11**, 025016 (2009).

[71] T. Maier, S. Graser, P. J. Hirschfeld and D. J. Scalapino, Phys. Rev. B **79**, 224510 (2009).

[72] H. Kontani and S. Onari, Phys. Rev. Lett. **104**, 157001 (2010).

[73] T. Saito, S. Onari and H. Kontani, Phys. Rev. B **88**, 045115 (2013).

[74] R. Thomale, C. Platt, W. Hanke, J. Hu and B. A. Bernevig, Phys. Rev. Lett. **107**, 117001 (2011).

[75] Y. Nakajima, Y. Tsuchiya, T. Taen, T. Tamegai, S. Okayasu and M. Sasase, Phys. Rev. B **80**, 012510 (2009).

[76] A. C. Damask and G. J. Dienes, Point Defects in Metals (Gordon & Breach, London) (1963).

[77] Y. Wang, A. Kreisel, P. J. Hirschfeld and V. Mishra Phys. Rev. B **87**, 094504 (2013).

[78] Y. Mizukami, M. Konczykowski, Y. Kawamoto, S. Kurata, S. Kasahara, K. Hashimoto, V. Mishra, A. Kreisel, Y. Wang, P.J. Hirschfeld, Y. Matsuda and T. Shibauchi, Nature Commun. **5**, 5657 (2014).

[79] C. P. Strehlow, M. Konczykowski, J. A. Murphy, S. Teknowijoyo, K. Cho, M. A. Tanatar, T. Kobayashi, S. Miyasaka, S. Tajima and R. Prozorov, Phys. Rev. B **90**, 020508(R) (2014).

[80] S. Doniach, Physica B+C **91**, 231-234 (1977).

[81] K. Yamada, K. Yosida and K. Hanzawa, Prog. Theor. Phys. **71**, 450 (1984).

[82] O. Stockert, J. Arndt, E. Faulhaber, C. Geibel, H. S. Jeevan, S. Kirchner, M. Loewenhaupt, K. Schmalzl, W. Schmidt, Q. Si and F. Steglich, Nat. Phys. **7**, 119-124 (2011).

[83] R. Modler, M. Lang, C. Geibel, C. Schank, R. Mfiller-Reisener, P. Hellmann, A. Link, G. Sparn, W. Assmus, F. Steglich, Physica B **206**&**207**, 586-588 (1995).

[84] F. Steglich, P. Gegenwart, C. Geibel, R. Helfrich, P. Hellmann, M. Lang, A. Link, R. Modler, G. Sparn, N. Biittgen and A. Loidl, Physica B **223**&**224**, 1-8 (1996).

[85] M. Hunt, P. Meeson, P. -A. Probst, P. Reinders, M. Springford, W. Assmus and W. Sun, J. Phys.: Cond. Matt. **2**, 6859-6864 (1990).

[86] H. Harima and A. Yanase, J. Phys. Soc. Jpn. **60**, 21 (1991).

[87] G. Zwicknagl and U. Pulst, Physica B **186** - **188**, 895-898 (1993).

[88] H. Ikeda, M. -T Suzuki and R. Arita, Phys. Rev. Lett. **114**, 147003 (2015)

[89] H. Nakamura, Y. Kitaoka, H. Yamada and K. Asayama, J. Magn. Magn. Mater. **76**&**77**, 517-519 (1988).

[90] Y. J. Uemura, W. J. Kessler, X. H. Yu, H. E. Schone, J. R. Kempton, C. E. Stronach, S. Barth, F. N. Gygax, B. Hitti, A. Schenck, C. Baines, W. F. Lankford, Y. $\overline{\text{O}}$nuki and T. Komatsubara, Physica C $\mathbf{153-155}$, 455 (1988) .

[91] Y. J. Uemura, W. J. Kossler, X. H. Yu, H. E. Schone, J. R. Kempton, C. E. Stronach, S. Barth, F. N. Gygax, B. Hitti, A. Schenck, C. Baines, W. F. Lankford, Y. $\overline{\text{O}}$nuki and T. Komatsubara, Phys. Rev. B **39**, 4726 (1989).

[92] O. Stockert, D. Andreica, A. Amato, H. S. Jeevan, C. Geibel and F. Steglich, Physica B **374**&**375**, 167-170 (2006).

[93] O. Stockert, E. Faulhaber, G. Zwicknagl, N. Stüßer, H. S. Jeevan, M. Deppe, R. Borth, R. Küchler, M. Loewenhaupt, C. Geibel and F. Steglich, Phys. Rev. Lett. **92**, 136401 (2004).

[94] O. Stockert, E. Faulhaber, K. Schmalzl, W. Schmidt, H. S. Jeevan, M. Deppe, C. Geibel, T. Cichorek, T. Nakanishi, M. Loewenhaupt, and F Steglich, J. Phys.: Conf. Ser. **51**, 211-218 (2006).

[95] J. Arndt, O. Stockert, E. Faulhaber, P. Fouquet, H. S. Jeevan, C. Geibel, M. Loewenhaupt and F. Steglich, J. Phys: Conf. Ser. **200**, 012009 (2010).

[96] O. Stockert, M. Nicklas, P. Thalmeier, P. Gegenwart and F. Steglich, *Handbook of Magnetism and Advanced Magnetic Materials* vol **4**, ed H. Kronmüßller and S. Parkin (John Wiley & Sons, Ltd.) p 1 (2007).

[97] K. Ueda, Y. Kitaoka, H. Yamada, Y. Kohori, T. Kohara and K. Asayama, J. Phys. Soc. Jpn. **56**, 867-870 (1987).

[98] Y. Kitaoka, H. Yamada, K. Ueda, Y. Kohori, T. Kohara, Y. Oda and K. Asayama, Jpn. J. Appl. Phys. **26**, 1221 (1987).

[99] H. A. Vieyra, N. Oeschler, S. Seiro, H. S. Jeevan, C. Geibel, D. Parker and F. Steglich Phys. Rev. Lett. **106**, 207001 (2011).

[100] P. Gegenwart, C. Langhammer, C. Geibel, R. Helfrich, M. Lang, G. Sparn, F. Steglich, R. Horn, L. Donnevert, A. Link and W. Assmus, Phys. Rev. Lett. **81**, 1501 (1998).

[101] T. Moriya and T. Takimoto, J. Phys. Soc. Jpn. **64**, 960 (1995).

[102] A. J. Millis, Phys. Rev. B **48**, 7183 (1993).

[103] J. Paglione, M. A. Tanatar, D. G. Hawthorn, E. Boaknin, R. W. Hill, F. Ronning, M. Sutherland, L. Taillefer, C. Petrovic and P. C. Canfield, Phys. Rev. Lett. **91**, 246405 (2003).

[104] J. Custers, P. Gegenwart, H. Wilhelm, K. Neumaier, Y. Tokiwa, O. Trovarelli, C. Geibel, F. Steglich, C. Pépin and P. Coleman, Nature **424**, 524-527 (2003).

[105] T. Tayama, M. Lang, T. Lühmann, F. Steglich and W. Assmus Phys. Rev. B **67**, 214504 (2003).

[106] K. Ishida, Y. Kawasaki, K. Tabuchi, K. Kashima, Y. Kitaoka, K. Asayama, C. Geibel and F. Steglich Phys. Rev. Lett. **82**, 5353 (1999).

[107] J. Arndt, O. Stockert, K. Schmalzl, E. Faulhaber, H. S. Jeevan, C. Geibel, W. Schmidt, M. Loewenhaupt and Frank Steglich, Phys. Rev. Lett. **106**, 246401 (2011).

[108] H. Q. Yuan, F. M. Grosche, M. Deppe, C. Geibel, G. Sparn and F. Steglich, Science **302**, 2104 (2003).

[109] F. Thomas, J. Thomasson, C. Ayache, C. Geibel and F. Steglich, Physica B **186-188**, 303 (1993).

[110] A. T. Holmes, A. Demuer and D. Jaccard, Acta Phys. Pol. B. **34**, 567 (2003).

[111] D. Jaccard, H. Wilhelm, K. Alami-Yadri, E. Vargoz and Physica B **259-261**, 1 (1999).

[112] A. Onodera, S. Tsuduki, Y. Ohishi, T. Watanuki, K. Ishida, Y. Kitaoka and Y. Onuki, Solid State Commun. **123**, 113 (2002).

[113] G. Seyfarth, A. -S. Rüetschi, K. Sengupta, A. Georges and D. Jaccard, Europhys. Lett. **98**, 17012 (2012).

[114] A. T. Holmes, D. Jaccard and K. Miyake Phys. Rev. B **69**, 024508 (2004).

[115] A. Jayaraman, Phys. Rev. **137**, A179 (1965).

[116] M. J. Lipp, D. Jackson, H. Cynn, C. Aracne, W. J. Evans and A. K. McMahan, Phys. Rev. Lett. **101**, 165703 (2008).

[117] K. Fujiwara, Y. Hata, K. Kobayashi, K. Miyoshi, J. Takeuchi, Y. Shimaoka, H. Kotegawa, T. C. Kobayashi, C. Geibel and F. Steglich, J. Phys. Soc. Jpn **77**, 123711 (2008).

[118] B. Keimer, P. Bourges, H. F. Fong, Y. Sidis, L. P. Regnault, A. Ivanov, D. L. Milius, I. A. Aksay, G. D. Gu and N. Koshizuka, J. Phys. Chem. Solids **60**, 1007-1011 (1999).

[119] C. Stock, C. Broholm, J. Hudis, H. J. Kang and C. Petrovic, Phys. Rev. Lett. **100**, 087001 (2008).

[120] S. Onari and H. Kontani, Phys. Rev. B **84**, 144518 (2011).

[121] D. Parker, O. V. Dolgov, M. M. Korshunov, A. A. Golubov and I. I. Mazin, Phys. Rev. B **78**, 134524 (2008).

[122] Y. Yamakawa, S. Onari and H. Kontani, Supercond. Sci. Technol. **25**, 084006 (2012).

[123] M. Yamashita, Y. Senshu, T. Shibauchi, S. Kasahara, K. Hashimoto, D. Watanabe, H. Ikeda, T. Terashima, I. Vekhter, A. B. Vorontsov and Y. Matsuda Phys. Rev. B **84**, 060507(R) (2011).

[124] S. Kittaka, Y. Aoki, Y. Shimura, T. Sakakibara, S. Seiro, C. Geibel, F. Steglich, H. Ikeda and K. Machida, Phys. Rev. Lett. **112**, 067002 (2014).

[125] C. Pfleiderer, Rev. Mod. Phys. **81**, 1551-1624 (2009).

[126] N. D. Mathur, F. M. Grosche, S. R. Julian, I. R. Walker, D. M. Freye, R. K. W. Haselwimmer and G. G. Lonzarich, Nature **394**, 39-43 (1998).

[127] P. Thalmerier and G. Zwicknagl, Handbook on the Physics and Chemistry of Rare Earths, Vol. **36** (2004).

[128] K. Izawa, H. Yamaguchi, Y. Matsuda, H. Shishido, R. Settai and Y. Onuki, Phys. Rev. Lett. **87**, 057002 (2001).

[129] B. B. Zhou, S. Misra, E. H. da Silva Neto, P. Aynajian, R. E. Baumbach, J. D. Thompson, E. D. Bauer and A. Yazdani, Nat. Phys. **9**, 474-479 (2013).

[130] I. I. Mazin, Nature **464**, 183-186 (2010).

[131] L. Zhu, M. Garst, A. Rosch and Q. Si, Phys. Rev. Lett. **91**, 066404 (2003).

[132] A. Rosch, Phys. Rev. Lett. **82**, 4280-4283 (1999).

[133] S. Seiro, M. Deppe, H. Jeevan, U. Burkhardt and C. Geibel, Phys. Status Solidi B **247**, 614-616 (2010).

[134] D. A. Bonn and W. N. Hardy, in Physical Properties of High-Temperature Superconductors, Vol. **5**, edited by D. M. Ginsberg, (World Scientific, Singapore) (1996).

[135] Y. J. Uemura, W. J. Kossler, B. Hitti, J. R. Kempton, H. E. Schone, X. H. Yu, C. E. Stronach, W. F. Lankford, D. R. Noakes, R. Keitel, M. Senba, J. H. Brewer, E. J. Ansaldo, Y. Oonuki, T. Komatsubara, Hyperfine Interactions **31**, 413-418 (1986).

[136] F. Gross, B. S. Chandrasekhar, K. Andres, U. Rauchschwalbe, E. Bucher and B. Lüth, Physica C: Superconductivity, **153-155**, 439-440 (1988).

[137] R. Prozorov, V. G. Kogan, Rep. Prog. Phys. **74**, 124505 (2011).

[138] F. Rullier-Albenque, H. Alloul and R. Tourbot, Phys. Rev. Lett. **91**, 047001 (2003).

[139] M. Putti, M. Affronte, C. Ferdeghini, P. Manfrinetti, C. Tarantini and E. Lehmann, Phys. Rev. Lett. **96**, 077003 (2006).

[140] A. E. Karkin, Y. N. Akshentsev and B. N. Goshchitskii, JETP Lett. **97**, 347-351 (2013).

[141] R. Prozorov, M. Konczykowski, M. A. Tanatar, A. Thaler, S. L. Bud'ko, P. C. Canfield, V. Mishra, P. J. Hirschfeld, Phys. Rev. X **4**, 041032 (2014).

[142] J. D. Fletcher, A. Carrington, O. J. Taylor, S. M. Kazakov and J. Karpinski, Phys. Rev. Lett. **95**, 097005 (2005).

[143] T. Jacobs, B. A. Willemsen, S. Sridhar, R. Nagarajan, L. C. Gupta, Z. Hossain, C. Mazumdar, P. C. Canfield and B. K. Cho, Phys. Rev. B **52**, R7022-R7025 (1995).

[144] S. C. Wimbush, L. Schultz and B. Holzapfel, Physica C **408-410**, 83-84 (2004).

[145] R. Balian and N. R. Werthamer, Phys. Rev. **131**, 1553-1564 (1963).

[146] M. Sigrist and K. Ueda, Rev. Mod. Phys. **63**, 239-311 (1991).

[147] O. Bodensiek, R. Žitko, M. Vojta, M. Jarrell, T. Pruschke, Phys. Rev. Lett. **110**, 146406 (2013).

[148] R. Tazai, Y. Yamakawa, M. Tsuchiizu, H. Kontani, Phys. Rev. B **94**, 115155 (2016).

Published works

Main works

1. **T. Yamashita**, T. Takenaka, Y. Tokiwa, J. A. Wilcox, Y. Mizukami, D. Terazawa, Y. Kasahara, S. Kittaka, T. Sakakibara, M. Konczykowski, S. Seiro, H. S. Jeevan, C. Geibel, C. Putzke, T. Onishi, H. Ikeda, A. Carrington, T. Shibauchi, and Y. Matsuda, "Fully gapped superconductivity with no sign change in the prototypical heavy-fermion $CeCu_2Si_2$", submitted to Science Advances.

2. **T. Yamashita**, Y. Tokiwa, D. Terazawa, M. Nagao, S. Watauchi, I. Tanaka, T. Terashima, and Y. Matsuda,
"Conventional *s*-wave superconductivity in BiS_2-based $NdO_{0.71}F_{0.29}BiS_2$ revealed by thermal transport measurements",
Journal of the Physical Society of Japan **85**, 073707 (2016). (©2016 The Physical Society of Japan)

3. **T. Yamashita**, Y. Shimoyama, Y. Haga, T. D. Matsuda, E. Yamamoto, Y. Onuki, H. Sumiyoshi, S. Fujimoto, A. Levchenko, T. Shibauchi, and Y. Matsuda,
"Colossal Thermomagnetic Response in the Exotic Superconductor URu_2Si_2",
Nature Physics **11**, 17-20 (2015). (©2014 Macmillan Publishers Limited, part of Springer Nature)

Journal articles (including main works)

1. **T. Yamashita**, T. Takenaka, Y. Tokiwa, J. A. Wilcox, Y. Mizukami, D. Terazawa, Y. Kasahara, S. Kittaka, T. Sakakibara, M. Konczykowski, S. Seiro, H. S. Jeevan, C. Geibel, C. Putzke, T. Onishi, H. Ikeda, A. Carrington, T. Shibauchi, and Y. Matsuda, "Fully gapped superconductivity with no sign change in the prototypical heavy-fermion

$CeCu_2Si_2$",
submitted to Science Advances.

2. T. Watashige, S. Arsenijević, **T. Yamashita**, D. Terazawa, T. Onishi, L. Opherden, S. Kasahara, Y. Tokiwa, Y. Kasahara, T. Shibauchi, H. v. Löhneysen, J. Wosnitza, and Y. Matsuda,
"Quasiparticle Excitations in the Superconducting State of FeSe Probed by Thermal Hall Conductivity in the Vicinity of the BCS-BEC Crossover",
Journal of the Physical Society of Japan **86**, 014707 (2017).

3. S. Kasahara, **T. Yamashita**, A. Shi, R. Kobayashi, Y. Shimoyama, T. Watashige, K. Ishida, T. Terashima, T. Wolf, F. Hardy, C. Meingast, H. v. Löhneysen, A. Levchenko, T. Shibauchi, and Y. Matsuda,
"Giant superconducting fluctuations in the compensated semimetal FeSe at the BCS-BEC crossover",
Nature Communications **7**, 12843 (2016).

4. **T. Yamashita**, Y. Tokiwa, D. Terazawa, M. Nagao, S. Watauchi, I. Tanaka, T. Terashima, and Y. Matsuda,
"Conventional *s*-wave superconductivity in BiS_2-based $NdO_{0.71}F_{0.29}BiS_2$ revealed by thermal transport measurements",
Journal of the Physical Society of Japan **85**, 073707 (2016).

5. Y. Tokiwa, **T. Yamashita**, M. Udagawa, S. Kittaka, T Sakakibara, D. Terazawa, Y. Shimoyama, T. Terashima, Y. Yasui, T. Shibauchi, and Y. Matsuda,
"Possible observation of highly itinerant quantum magnetic monopoles in the frustrated pyrochlore $Yb_2Ti_2O_7$",
Nature Communications **7**, 10807 (2016).

6. M. D. Watson, **T. Yamashita**, S. Kasahara, W. Knafo, M. Nardone, J. Beard, F.

Hardy, A. McCollam, A. Narayanan, S. F. Blake, T. Wolf, A. A. Haghighirad, C. Meingast, A. J. Schofield, H. von Löhneysen, Y. Matsuda, A. I. Coldea, and T. Shibauchi,
"Dichotomy between the Hole and Electron Behavior in Multiband Superconductor FeSe Probed by Ultrahigh Magnetic Fields",
Physical Review Letter **115**, 027006 (2015).

7. S. F. Blake, M. D. Watson, A. McCollam, S. Kasahara, R. D. Johnson, A. Narayanan, G. L. Pascut, K. Haule, V. Kiryukhin, **T. Yamashita**, D. Watanabe, T. Shibauchi, Y. Matsuda, and A. I. Coldea ,
"Fermi Surface of $IrTe_2$ in the Valence-Bond State as Determined by Quantum Oscillations",
Physical Review B **91**, 121105(R) (2015).

8. **T. Yamashita**, Y. Shimoyama, Y. Haga, T. D. Matsuda, E. Yamamoto, Y. Onuki, H. Sumiyoshi, S. Fujimoto, A. Levchenko, T. Shibauchi, and Y. Matsuda,
"Colossal Thermomagnetic Response in the Exotic Superconductor URu_2Si_2",
Nature Physics **11**, 17-20 (2015).

9. S. Kasahara, T. Watashige, T. Hanaguri, Y. Kohsaka, **T. Yamashita**, Y. Shimoyama, Y. Mizukami, R. Endo, H. Ikeda, K. Aoyama, T. Terashima, S. Uji, T. Wolf, H. v. Löhneysen, T. Shibauchi, and Y. Matsuda,
"Field-Induced Superconducting Phase of FeSe in the BCS-BEC Crossover",
Proceedings of the National Academy of Sciences **111**, 16309-16313 (2014).

10. D. Watanabe, **T. Yamashita**, Y. Kawamoto, S. Kurata, Y. Mizukami, T. Ohta, S. Kasahara, M. Yamashita, T. Saito, H. Fukazawa, Y. Kohori, S. Ishida, K. Kihou, C. H. Lee, A. Iyo, H. Eisaki, A. B. Vorontsov, T. Shibauchi, and Y. Matsuda,
"Doping evolution of the quasiparticle excitations in heavily hole-doped $Ba_{1-x}K_xFe_2As_2$: A possible superconducting gap with sign-reversal between hole pockets",
Physical Review B **89**, 115112 (2014).

Acknowledgments

I would like to acknowledge Professor Yuji Matsuda for valuable guidance and great encouragement through my PhD student course. I also would like to acknowledge Professor Takasada Shibauchi at the University of Tokyo for fruitful discussion on my experimental results. Without their guidance and stimulation, this work would not have been possible.

I also would like to appreciate Professor Yoshifumi Tokiwa at Universität Augsburg for his great experimental assistance and valuable discussion. This work was extensively improved by his help.

This study could not be possible without high-quality single crystals. I would like to appreciate our collaborators. Prof. Christoph Geibel, Dr. Silvia Seiro, and Dr. Hirale S. Jeevan at Max Planck Institute for Chemical Physics of Solids, who provided us with very high-quality single crystals of $CeCu_2Si_2$. Prof. Isao Tanaka, Prof. Satoshi Watauchi, and Prof. Masanori Nagao at university of Yamanashi, who provided us with very high-quality single crystals of $NdO_{0.71}F_{0.29}BiS_2$. Prof. Yoshichika Onuki at University of the Ryukyus, Prof. Tatsuma D. Matsuda at Tokyo Metropolitan University, Prof. Yoshinori Haga, and Prof. Etsuji Yamamoto at the Japan Atomic Energy Agency provided us with ultraclean single crystals of URu_2Si_2.

I wish to thank Prof. Yuta Mizukami and Mr. Takaaki Takenaka at the University of Tokyo for the penetration depth measurement and helpful discussion. I also thank Prof. Antony Carrington, Dr. Carsten Putzke, and Dr. Joe A. Wilcox for their assistance in the lower critical field, penetration depth measurement, and fruitful discussion. I wish to thank Prof. Marcin Konczykowski for the electron irradiation experiments. I wish to thank Prof. Toshiro Sakakibara and Prof. Shunichiro Kittaka at the Institute for Solid State Physics at the University of Tokyo for their assistance in the specific heat experiments. I would like to thank Prof. Hiroaki Ikeda for fruitful discussion and comment for the study of $CeCu_2Si_2$. I would like to thank Prof. Alex Levchenko,

Prof. Satoshi Fujimoto, and Dr. Hiroaki Sumiyoshi for their fruitful discussion for the study of URu_2Si_2. I would like to appreciate Mr. Daiki Terazawa and Mr. Takafumi Onishi for their great assistance in the thermal conductivity measurement and helpful discussion. I would like to appreciate Mr. Yusuke Shimoyama for his great assistance in the Nernst measurement.

I would like to thank Prof. Takahito Terashima, Prof. Shigeru Kasahara, and Prof. Yuichi Kasahara for experimental supports and helpful discussion. I am deeply indebted to all members in Prof. Matsuda group in Kyoto University, namely Dr. Tatsuya Watashige, Mr. Tomohiro Ishii, Mr. Masahiro Naritsuka, Mr. Yuki Sato, Mr. Yohei Torii, Mr. Hironori Hashimoto, and Souhei Miyake, for their helpful discussion and great supports.

I express my gratitude to the staffs of Research Center for Low Temperature and Material Science for providing liquid helium and liquid nitrogen. I would like to acknowledge the financial support of Research Fellowship for Young Scientists from Japan Society for the Promotion of Science.

Finally, I am deeply grateful to my parents, my grandparents, my sister, and rest of my family for their great supports and encouragement.